

11-8-2011

The Interplay Of Size- And Site-Dependence Of Magnetic Properties Of Diluted Magnetic Semiconductor Quantum Dots

Weiwei Zheng
The Florida State University

Follow this and additional works at: <http://diginole.lib.fsu.edu/etd>

Recommended Citation

Zheng, Weiwei, "The Interplay Of Size- And Site-Dependence Of Magnetic Properties Of Diluted Magnetic Semiconductor Quantum Dots" (2011). *Electronic Theses, Treatises and Dissertations*. Paper 5301.

This Dissertation - Open Access is brought to you for free and open access by the The Graduate School at DigiNole Commons. It has been accepted for inclusion in Electronic Theses, Treatises and Dissertations by an authorized administrator of DigiNole Commons. For more information, please contact lib-ir@fsu.edu.

THE FLORIDA STATE UNIVERSITY
COLLEGE OF ARTS AND SCIENCES

THE INTERPLAY OF SIZE- AND SITE-DEPENDENCE ON THE MAGNETIC
PROPERTIES OF DILUTED MAGNETIC SEMICONDUCTOR QUANTUM DOTS

By

WEIWEI ZHENG

A Dissertation submitted to the
Department of Chemistry and Biochemistry
in partial fulfillment of the
requirements for the degree of
Doctor of Philosophy

Degree Awarded:
Fall Semester, 2011

Weiwei Zheng defended this Dissertation on October 18, 2011.

The members of the supervisory committee were:

Geoffrey F. Strouse
Professor Directing Dissertation

Peng Xiong
University Representative

Naresh Dalal
Committee Member

Albert E. Stiegman
Committee Member

The Graduate School has verified and approved the above-named committee members, and certifies that the dissertation has been approved in accordance with university requirements.

To my parents and wife, who made this journey possible!

ACKNOWLEDGEMENTS

Obtaining a Ph.D. degree in the United States is one of the most exciting experiences for me. When I arrived at Florida State University from China six years ago, I did not expect there would be so many interesting, promising, and adventurous experiences, as well as a lot of frustrating and disappointing moments. Now, the long journey is approaching to an end. I am very grateful to the professors, colleagues, friends, together with my families, all of whom not only share my progress and happiness, but help me get through the tough time as well.

First of all, I would like to thank my advisor Professor Geoffrey F. Strouse, who helps me become a good scientist. Thank you for your inspiration, knowledge, patience and tolerance, for you have changed me from a first-year graduate student who could not express his idea in English fluently and had no idea what a top-level scientific research was, to a confident and well-trained Ph.D. who is able to contribute to the academic community.

I would like to thank my committee members: Prof. Xiong, Prof. Dalal and Prof. Stiegman for the effective cooperation, helpful suggestions, and the knowledge you were always willing to give.

The Strouse group, thank you all for the helpful conversations and debates, which inspire me to think deeper in science. It turns out that I have more fun in research.

The Dalal group (Zhenxing, Jingfang, Vasanth, Jared, Raghabendra, and Mekhala), thank you all for helping me with the EPR and for enjoyable discussions in magnetochemistry.

I also appreciate my family---my parents, my brother and sister, all of whom help me become a good person. They have been always sharing good news and funny stories in their life with me, allowing me to experience the beauty in real life besides my lab work day by day. They let me feel deeply grateful for everything in my life: enjoy the good, and learn from the bad.

I would like to thank my wife, Xue, for she always encourages me to listen to the inner voice and to achieve what I really want.

I would also like to thank the following people:

Dr. Michael Shatruk, thanks for helpful discussion and suggestions.

Donny, thanks for spending time teaching me lots of research techniques in my first two years.

Mani, you are a great friend, whom I hope I can always keep in touch with.

Aaron, I thought you drove too fast to be safe, but seemed I was wrong.

Josh, you are such a gentleman and always nice to me.

Martha, I have been wondering why you are so talented in teaching.

Qilin, you are so hard a worker and always hope for the best. I couldn't have had a better neighbor.

Derek, you are so organized in the lab.

Steve, I hope I can express scientific ideas as excellently as you do.

Megan Foley, you give our group so many laughs and I am always glad to work with you.

Megan Muroski and Rachel, thank you for running group meetings and arranging so many interesting potlucks for our group.

Christopher Ridel, it is you that run the lab, which makes our working environment clean and safe, I like that.

Chris Breshike, you did an excellent job in TEM and you are a good friend.

Ryan Riskowski, I was deeply impressed by your very first talk in IMB, Wooooo!

There are many other people that I don't mention here who have also helped me and encouraged me to pursue my dream. Thank you!

TABLE OF CONTENTS

List of Figures	viii
Abstract	xii
CHAPTER ONE	1
Introduction	1
1.1 Magnetism	1
1.1.1 Classes of magnetic materials	3
1.1.2 Hysteresis loop	9
1.2 Magnetic nanoparticles and finite-size effects	9
1.2.1 Single domain limit	11
1.2.2 Superparamagnetic limit and superparamagnetism	12
1.2.3 Surface effects	15
1.3 Diluted magnetic semiconductors (DMSs) and diluted magnetic semiconductor quantum dots (DMSQDs)	16
1.3.1 Diluted magnetic semiconductors (DMSs)	16
1.3.2 Diluted magnetic semiconductors quantum dots (DMSQDs)	17
1.4 Magnetic studies of DMSs and DMSQDs	20
1.4.1 Superconducting Quantum Interference Devices (SQUID) Magnetometry	20
1.4.2 Electron paramagnetic resonance (EPR) Spectroscopy	21
1.5 Conclusion	24
CHAPTER TWO	26
Involvement of Carriers in the Size-dependent Magnetic Exchange for Mn: CdSe Quantum Dots	26
2.1 Introduction	26
2.2 Experimental	28
2.3 Results	30
2.4 Discussion	41

2.5 Conclusion	47
CHAPTER THREE	51
Probing the Local Site Environments in Mn: CdSe Quantum Dots	51
3.1 Introduction.....	51
3.2 Experimental.....	54
2.3 Results and discussion	58
3.4 Conclusion	82
CHAPTER FOUR.....	85
Evidence of Spinel Phase Formation in Cr Doped ZnSe Quantum Dots	85
4.1 Introduction.....	85
4.2 Experimental.....	88
4.3 Results and discussion	90
4.4 Conclusion	106
CHAPTER FIVE	107
Conclusions and Future Directions.....	107
5.1 Future directions	107
5.2 Conclusions.....	110
Appendix A.....	111
Permission and copyright.....	111
References.....	113
Biographical Sketch.....	122

LIST OF FIGURES

- Figure 1.1.** Schematic illustrating the arrangements of magnetic dipoles for paramagnetic, ferromagnetic, ferrimagnetic and antiferromagnetic materials in the absence of an external magnetic field (H). Note that it doesn't show diamagnetism since there are no magnetic dipoles in diamagnetic materials. 2
- Figure 1.2.** Curie-Weiss law plots of paramagnetic, ferromagnetic, ferrimagnetic and antiferromagnetic materials. The Curie-Weiss temperature (θ) can be obtained by extrapolate the high temperature data to the T-axis. 6
- Figure 1.3.** A typical magnetization curve of a ferro- or ferrimagnetic material, which shows saturation magnetization (M_s), the remanence magnetization (M_r), and the coercivity (H_c). 8
- Figure 1.4.** Schematic illustrating the dependence of magnetic coercivity on particle size. The coercivity falls to zero for superparamagnetic colloidal particles. 10
- Figure 1.5.** The ZFC and FC curves of 2.8 nm Mn:CdSe nanoparticles in diameter with blocking temperature (T_B) 12 K. 14
- Figure 1.6.** Schematic representation of a QD depicting the surface and core doping sites for a 2 nm Mn:CdSe QD, showing both the core and surface site for Mn(II), and theoretical fit and deconvolution of the 406.4GHz HF-EPR spectra allowing definitive assignment of discrete sites for the Mn(II) occupying a substitutional Cd(II) site within the core (red) and on the surface (blue). 23
- Figure 2.1.** Characterization data for 2.8 nm, 4.0 nm, 5.0 nm, and 5.8 nm (in diameter) 0.6 % Mn:CdSe QDs A) absorption (dashed) and photoluminescence (solid) spectra, B) TEM images (scale bar = 20 nm), C) Powder XRD patterns, and D) electron diffraction TEM images. The figure is color coded for the QD sizes as noted in the image. 32
- Figure 2.2.** A) Temperature dependent ZFC and FC (100 Oe) susceptibility data, and B) Temperature dependent field sweep plots for 2.8 nm, 4.0 nm, 5.0 nm and 5.8 nm 0.6% Mn:CdSe QDs. 34
- Figure 2.3.** ZFC/FC susceptibility at 50 Oe, 100 Oe and 500 Oe for 2.8 nm Mn:CdSe QDs (A) and at 20 Oe and 100 Oe for 5.8 nm Mn:CdSe QDs (B). 35
- Figure 2.4.** Magnetization vs. H/T plots for 2.8 nm, 4.0 nm, 5.0 nm and 5.8 nm Mn:CdSe QDs. 36
- Figure 2.5.** Temperature dependent ac-susceptibility (1–1000 Hz) data for the 2.8 nm and 4.0 nm 0.6% Mn:CdSe QDs showing the A) in-phase (real) component $\chi'(T)$, B) out of phase (imaginary) component $\chi''(T)$, and C) temperature dependent Arrhenius plots for the imaginary component $\chi''(T)$ 38

Figure 2.6. Plot of the A) Temperature dependent coercive field (mT) for 2.8 nm, 4.0 nm, 5.0 nm, and 5.8 nm Mn: CdSe QDs. The dependence of the coercive at 2 K vs volume of the QD is plotted in the inset. B) Theoretical Brillouin function assuming $S = 5/2$, $g = 2.0$ compared to the normalized magnetization data.	40
Figure 2.7. Brillouin function fitting of A) 5.8 nm (2 K and 50 K), B) 5.0 nm (2 K and 50 K), C) 4.0 nm (2 K, 40 K, and 100 K), and D) 2.8 nm (2 K, 40 K, and 100 K) Mn: CdSe QDs.	44
Figure 2.8. Size Dependent A) Curie-Weiss law and B) χT vs. T plots for Mn: CdSe QDs.	46
Figure 2.9. The size dependent magnetic susceptibility arising from the temperature independent Pauli paramagnetic contribution to the total susceptibility.	48
Figure 2.10. Proposed model of the onset of magnetic exchange in Mn: CdSe QDs governed by long-range carrier mediated RKKY processes.	49
Figure 3.1. Characterization data for 5.0 ± 0.3 nm 0.6% homogeneously doped Mn: CdSe QDs. A) Absorption spectra in toluene (spectra for other sizes are included), B) TEM image (HR-TEM inserted), C) pXRD pattern (surface doped Mn: CdSe included), and D) FT-IR spectra. In Figure S1D, the lack of FT-IR absorptions for Mn-O at 411, 524, and 630 cm^{-1} is suggestive that the presence of Mn(III) impurities are well below the detectable limit for the experiment ($<0.01\%$).	57
Figure 3.2. A) Schematic representation of a QD depicting the surface and core doping sites for a 2 nm Mn: CdSe QD showing the core and surface site for Mn(II). B) EPR splitting pattern for a Mn(II) ion ($S = 5/2$, $I = 5/2$ and $L = 0$) occupying a pseudo- T_d site in CdSe showing only first-order perturbation. The transition fields of hyperfine splitting are marked by vertical arrows corresponding to the six allowed transition ($\Delta M_S = \pm 1$, $\Delta M_I = 0$), corresponding to the M_I : $5/2 \rightarrow 5/2$, $3/2 \rightarrow 3/2$, $1/2 \rightarrow 1/2$, $-1/2 \rightarrow -1/2$, $-3/2 \rightarrow -3/2$, and $-5/2 \rightarrow -5/2$ nuclear transitions.	60
Figure 3.3. A) Frequency dependent EPR spectra (298K) for 5.0 nm diameter $\text{Mn}_x\text{Cd}_{1-x}\text{Se}$ ($x = 0.006$) (6% RMS size dispersity) measured at 34, 216, 324, and 406.4 GHz. B) Theoretical fit and deconvolution of the 406.4GHz HF-EPR spectra allowing definitive assignment of discrete sites for the Mn(II) occupying a substitutional Cd(II) site within the core (site 1, red), and surface (site 2, blue).	63
Figure 3.4. Fitting of the frequency dependent 5.0 nm Mn: CdSSe QD EPR spectra identifying the core (red), and surface (blue) components at 34 GHz, 216 GHz and 324 GHz EPR data.	64
Figure 3.5. Frequency dependence of central resonance field for A) site 1 and B) site 2, C) Hyperfine constant (A), and D) Linewidth (ΔH) at 298 K for the 5.0 nm diameter $\text{Mn}_x\text{Cd}_{1-x}\text{Se}$ ($x = 0.006$). The dashed lines are guides to the eye.	65
Figure 3.6. Fitting site 1 (core) of the EPR spectra for the 5.0 nm Mn: CdSe QD at fixed values of D for the single crystal ($D = 0.015 \text{ cm}^{-1}$) and for reported Mn: CdSe QDs ($D = -0.082 \text{ cm}^{-1}$).	67
Figure 3.7. Mn $L_{3,2}$ edge X-ray absorption spectra of the Mn: CdSe QDs.	69

Figure 3.8. 406.4 GHz HF-EPR spectra for 5.0 nm $Mn_xCd_{1-x}Se$ ($x = 0.006$) ligand exchanged by DDN, TOP, TOP-Se, DDA, and py. 72

Figure 3.9. 406.4 GHz HF-EPR spectra for the $MnBr_2$ with DDA, the fitted A-value is 94.1 G.75

Figure 3.10. A) EPR measurements at 406.4 GHz (298 K) for i) 5.5 nm surface doped (black) $Mn:CdSe$ (0.4%) and ii) 5.0 nm stochastically doped (red) $Mn:CdSe$ (0.6%), EPR evolution of $Mn:CdSe$ QDs following acid etching of B) 5.0 nm stochastically doped $Mn:CdSe$, and C) 5.5 nm surface doped $Mn:CdSe$. The arrows in A) and C) indicate the surface component of the EPR spectra in $Mn:CdSe$ corresponding to $M_I: 5/2 \rightarrow 5/2$ (left) and $-5/2 \rightarrow -5/2$ (right) transitions. 76

Figure 3.11. Absorption spectra before and after acid etching for A) 5.5 nm surface doped and B) 5.0 nm stochastically doped $Mn:CdSe$ QDs..... 77

Figure 3.12. Plot of the change in the site 2 to total $Mn(II)$ sites intensity for acid etched QDs measured by 406.4 GHz EPR. The dotted lines represent theoretical plots for a spherical $CdSe$ QD (blue) and for an oblate QD with a 1:1.2 c/a ratio (red)..... 79

Figure 3.13. Size dependent A) EPR measurements at 406.4 GHz (298 K) for 1.3 nm, 2.8 nm, 5.0 nm and 5.8 nm $Mn_xCd_{1-x}Se$ ($x = 0.006$), B) g-value, C) Hyperfine constant (A), and D) Plot of the size dependence of the intensity of site 2 relative to the total $Mn(II)$ EPR intensities (at 406.4 GHz and 298 K). Theoretical lines for an idea spherical $CdSe$ (black dot line) and for an oblate QD with a 1.2:1 c/a ratio (red dot line) are shown..... 81

Figure 3.14. EPR measurements at 406.4 GHz (298K) on size selected QDs for A) 5.0 nm prior to size selection (red), B) the 4.6 nm (blue) and C) 5.2 nm (black). 83

Figure 4. 1. Characterization data A) absorption (dashed) and photoluminescence (solid) spectra for $ZnSe$ and $Cr:ZnSe$ QDs, B) pXRD patterns for $ZnSe$ and $Cr:ZnSe$ QDs, C) TEM image for $Cr:ZnSe$ QD, and D) TEM electron diffraction image for $Cr:ZnSe$ QDs..... 91

Figure 4. 2. The pXRD data for 2.5% and 4.0 % $Cr:ZnSe$ QDs..... 94

Figure 4. 3. Absorption (dashed) and photoluminescence (solid) spectra for 0%, 0.4%, 1.0%, 2.5%, 4.0% $Cr:ZnSe$ QDs. 95

Figure 4. 4. Cr $L_{2,3}$ edge X-ray absorption spectra. A) simulation of (a) $Cr(II)$, (b) $Cr(III)$, and (c) $Cr(IV)$ in a perfect O_h field ($10 Dq = 2.07$ eV). B) (a) $Cr:ZnSe$ QDs and (b) simulated distorted O_h crystal field for $Cr(III)$ 97

Figure 4. 5. Absorption spectra in concentrated toluene solution for 0%, 0.4%, 1.0%, 2.5%, 4.0% $Cr:ZnSe$ QDs. Insert is the energy level of $Cr(III)$ ion in a O_h crystal field. 98

Figure 4. 6. A) Frequency dependent EPR measurements at 10 K for $Cr:ZnSe$ QD, B) Frequency dependent of EPR central resonance field of 2.4% $Cr(III):ZnSe$ QD which can fit to $g = 1.9808$ for $Cr(III)$ ion. 100

Figure 4. 7. A) Absorption spectra before and after acid etching for the Cr:ZnSe QDs, and B) 200 GHz EPR of Cr:ZnSe QDs after acid etching..... 102

Figure 4. 8. A) Temperature dependent ZFC and FC (200 Oe) susceptibility data. The insert is the Curie-Weiss law plot showing negative Curie-Weiss temperature (-125 K), B) Field dependent magnetization (M) plots at 2, 10, 20, 30, 50 K, and C) Arrott plots (M^2 vs. H/M) for the Cr(2.5%):ZnSe QDs..... 103

Figure 4. 9. Illustration of part of the $ZnCr_2Se_4$ spinel structure in the ZnSe lattice. The Cr(III) ions (blue balls) occupy O_h sites and Zn(II) ions (green balls) occupy T_d sites. Three Zn(II) T_d sites were removed to add two Cr(III) O_h sites. 105

Figure 5. 1. A). Temperature dependent ZFC and FC (100 Oe) susceptibility data for 3.0 nm, 3.9 nm and 4.7 nm 1% Mn:CdSe QDs. Blocking temperature (TB) is indicated in the plots. B). Magnetization plots for 3.0 nm, 3.9 nm and 4.7 nm 1% Mn:CdSe QDs. The coercive field decreases as the size of the DQs increases which is the same trend found in 0.6% Mn:CdSe QDs. 108

ABSTRACT

This dissertation studies the size- and site-dependent optical and magnetic properties of II-VI quantum dots (QDs). The first chapter provides a theoretical background used to analyze the data and the properties expected for diluted magnetic semiconductor materials at the nanoscale. The second chapter probes the size-dependent magnetic properties for Mn(II) doped CdSe QDs. The Curie-Weiss law plots show significant size-dependent carrier concentration in the QDs. The carriers inside the small QDs can mediate the Mn(II)-Mn(II) ferromagnetic interaction by the RKKY model, which helps explain reasons for the observation of a superparamagnetism (SPM) in small Mn:CdSe QDs. The third chapter involves high frequency EPR analysis of possible dopant (Mn(II) ions) sites in CdSe lattice. Stochastically doped Mn:CdSe QDs and surface doped Mn:CdSe QDs were successfully made by traditional thermal decomposition of cluster and microwave irradiation. Two sets of hyperfine splitting were observed for stochastically doped Mn:CdSe QDs from EPR spectra and the ratio of the signal has liner relationship with the surface to volume ratio of QDs. One set of hyperfine splitting can be removed by surface acid treatment enabled us to identify the Mn(II) sites on the surface or core position of Mn:CdSe QDs. The fourth chapter is a study of chromium incorporation in ZnSe QDs by single cubic source precursor method. The formation of ZnCr_2Se_4 spinel structure was approved by XANES, and $^4\text{A}_{2g} \rightarrow ^4\text{T}_{2g}$ transition of Cr (III) ion in absorption spectra.

CHAPTER ONE

INTRODUCTION

1.1 Magnetism

Magnetic materials have played many important roles in our daily life for thousands of years. It was discovered that the origin of magnetism lies in the orbital and spin motion of electrons and how they interact with one another. Magnetic behavior in materials is determined by measuring the magnetic response (the susceptibility χ) to an external magnetic field (H), which is defined as:

$$\chi = M / H \quad (1.1)$$

where M is the magnetization. M and H are in the same units, which can be Gauss (G) or Oersted (Oe). So χ is dimensionless, but can be usually expressed as emu/cm^3 in volume magnetic susceptibility, emu/g in mass magnetic susceptibility and emu/mol in molar magnetic susceptibility. According to the arrangement of their magnetic dipoles in the absence and presence of an external magnetic field the magnetic order can be classified as diamagnetism, paramagnetism, ferromagnetism, ferrimagnetism, and antiferromagnetism.¹ Other types include the effects of domains, anisotropy, and long-range order. The main distinction is that in some materials, there is no collective interaction between atomic magnetic moments, whereas in other materials, there are very strong interactions between them. Figure 1.1 shows schematic diagrams of the arrangements of magnetic dipoles for paramagnetic, ferromagnetic, ferrimagnetic and antiferromagnetic materials. Note that it doesn't show diamagnetism since there are no magnetic dipoles in diamagnetic materials. In terms of susceptibility, diamagnetic substances are slightly repelled by such a field and have negative susceptibilities; paramagnetic substances have positive

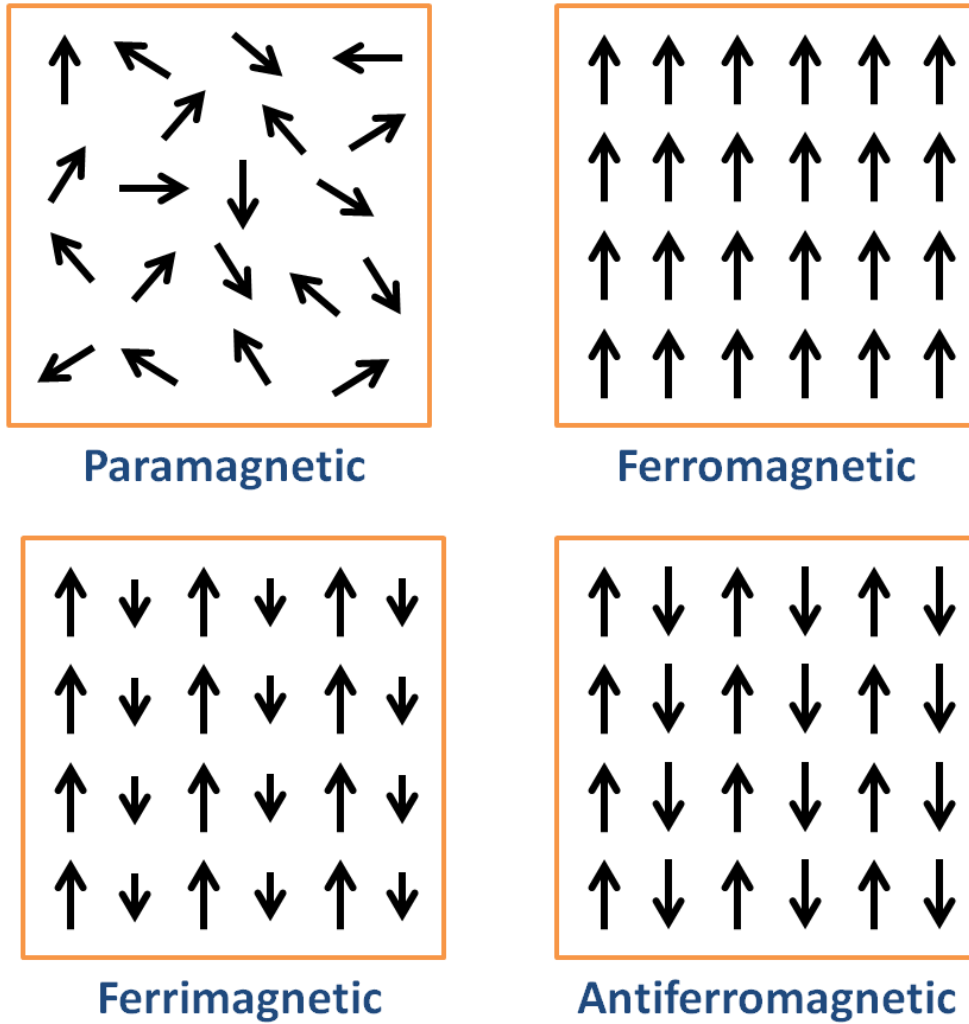


Figure 1.1. Schematic illustrating the arrangements of magnetic dipoles for paramagnetic, ferromagnetic, ferrimagnetic and antiferromagnetic materials in the absence of an external magnetic field (H). Note that it doesn't show diamagnetism since there are no magnetic dipoles in diamagnetic materials.

susceptibilities. Ferromagnetic materials typically show large, positive susceptibilities. The responses of materials to an external magnet can be either linear or nonlinear. Typical diamagnetic and paramagnetic substances are weakly magnetic and give a linear response to the strength of the external field. Ferromagnetic materials respond nonlinearly with an external field.

1.1.1 Classes of Magnetic Materials

Diamagnetism

Diamagnetism is a fundamental property of all matter and arises from the interaction of paired electrons with the magnetic field. The molar susceptibility of a diamagnetic material is negative and usually very weak on the order of -10^{-6} to -10^{-4} . Diamagnetic susceptibilities do not depend on the field strength, and the magnetization is zero when the field is zero. The magnetization of a diamagnet responds in the opposite direction to the external field. So, when exposed to a field, a negative magnetization is produced and the susceptibility is negative.

Paramagnetism

Some of the atoms or ions in this class of materials have a net magnetic moment due to unpaired electrons in partially filled orbitals. Paramagnetic materials have randomly oriented dipoles that can be aligned in an external field, thus the magnetic moment of a paramagnet tends to align in the same direction as the external field, which results in a net positive magnetization and susceptibility. However, the individual magnetic moments do not interact magnetically, and like diamagnets, the magnetization is zero when the field is removed. In addition, the efficiency of the field in aligning the moments is opposed by the randomizing effects of temperature. This results in a temperature dependent susceptibility, known as the Curie Law:

$$\chi = C / T \tag{1.2}$$

where χ is the magnetic susceptibility, C is the Curie constant (in emu*K/mol for molar magnetic susceptibility), and T is absolute temperature in K. Curie's constant can be expressed as:

$$C = \frac{Ng^2\mu_B^2J(J+1)}{3k_B} \quad (1.3)$$

where N is the number of magnetic moments, g is the Landé g-factor, μ_B is the Bohr magneton, J is the angular momentum quantum number and k_B is Boltzmann's constant. In cases when the orbital contribution to the magnetic moment is negligible ($L = 0$), then $J = S + L = S$ in the above equation. For a two level system ($S = 1/2$) the formula can be reduced to:

$$C = \frac{Ng^2\mu_B^2}{4k_B} \quad (1.4)$$

For paramagnetic ions with interacting magnetic moment the magnetic susceptibility in the paramagnetic region can be described as the Curie-Weiss law (Figure 1.2):

$$\chi = C / (T - \theta) \quad (1.5)$$

Where θ is the Curie-Weiss temperature. The susceptibility has a singularity at $T = \theta$. From the sign of the θ , the type of the interaction can be determined. For ferromagnetism the positive θ will be obtained, while negative θ can be obtained in ferrimagnetism and antiferromagnetism.

The paramagnetic metals fall into a distinct group, in that their susceptibility is relatively low and nearly independent of temperature. In a Pauli paramagnet, the electron distribution follows Fermi-Dirac statistics and only those electrons in an energy band about $k_B T$ of the top of the Fermi level have a chance to turn over in the field and take part in any energy changes. This could be due to thermal or magnetic effects. So only a fraction (T/T_F , where T_F is the Fermi temperature) of the total number of electrons contributes to the susceptibility, which is independent of temperature (Eqn 1.6).

$$M \approx \frac{N\mu^2 H}{k_B T} \cdot \frac{T}{T_F} = \frac{N\mu^2}{k_B T_F} H \quad (1.6)$$

Ferromagnetism

For a ferromagnetic material, magnetic dipoles can exist in the absence and presence of an external field because of the parallel alignment of magnetic moments. Ferromagnetic materials exhibit a long-range order phenomenon at the atomic level which causes the unpaired electron spins to line up parallel with each other in a region called a domain. A ferromagnetic material actually forms microscopic domains structure. In each domain all the spins are same alignment but each domain is oriented differently from its neighbors. Unlike paramagnetic materials, the atomic moments in the ferromagnetic materials exhibit very strong long range interactions between spin centers (S_i and S_j), which can be described by the following Hamiltonian with a positive exchange coupling constant J :

$$\hat{H} = -\sum_{i,j} 2J_{i,j} \hat{S}_i \hat{S}_j \quad (1.7)$$

These interactions are produced by electronic exchange forces and result in a parallel alignment of atomic moments, which will show a positive Curie-Weiss temperature in the Curie-Weiss law plot (Figure 1.2). These exchange forces are a quantum mechanical phenomenon due to the relative orientation of electronic spins. Even though electronic exchange forces are very large, thermal energy can eventually overcome the exchange and produce a randomizing effect. Magnetic ordering in ferromagnetic materials occurs below an ordering temperature, called the Curie temperature (T_c). Above T_c , the ferromagnet is disordered. The magnetization increases quickly upon cooling below this point and approaches the saturation value at 0 K. Examples of materials that exhibit ferromagnetism include Fe ($T_c = 1043$ K), MnAs ($T_c = 670$ K), CrO₂ ($T_c = 386$ K), and EuO ($T_c = 69$ K).²

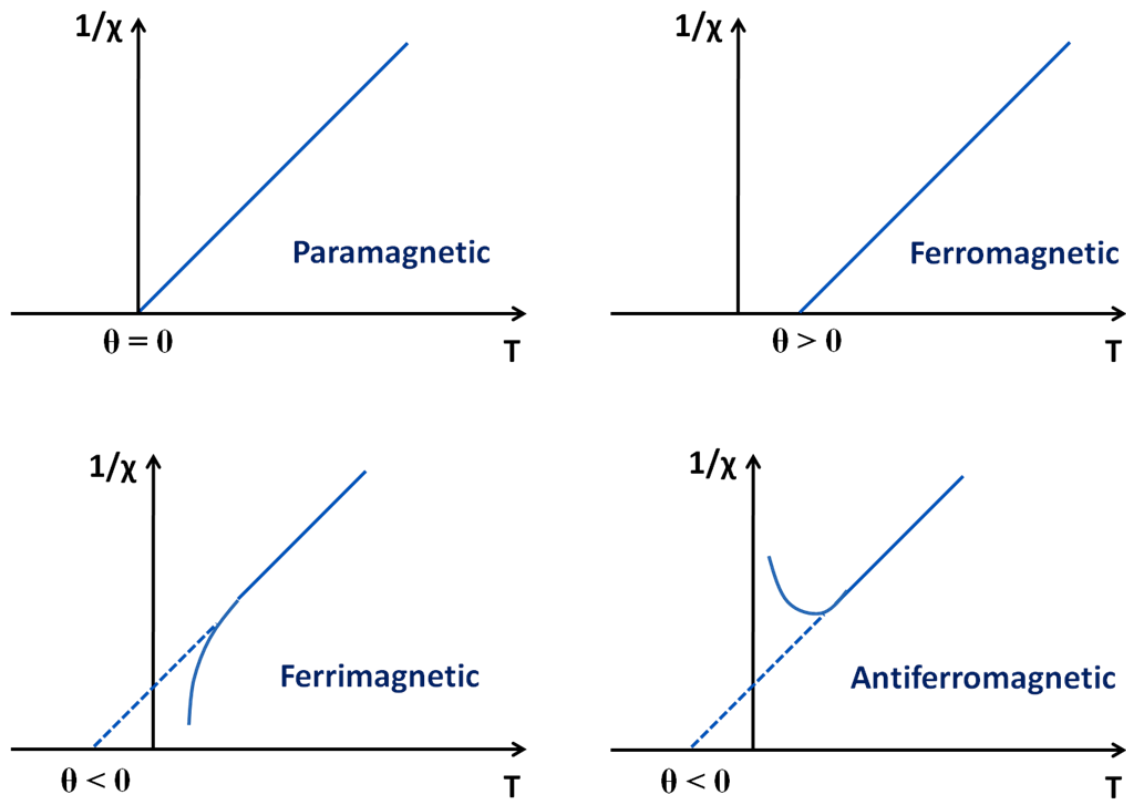


Figure 1.2. Curie-Weiss law plots of paramagnetic, ferromagnetic, ferrimagnetic and antiferromagnetic materials. The Curie-Weiss temperature (θ) can be obtained by extrapolate the high temperature data to the T-axis.

Ferrimagnetism

In a ferromagnetic material two types of dipoles are arranged in the opposite directions. One type among the two is prevailing, so there is some magnetization present even if there is no field. There is a net magnetization below the Curie temperature (T_c). Stronger dipoles can be obtained in the absence of an external magnetic field. A well known ferrimagnetic material is magnetite (Fe_3O_4) with the spinel structure. The structural formula for magnetite is: $[\text{Fe}^{3+}]_A[\text{Fe}^{3+},\text{Fe}^{2+}]_B\text{O}_4$ with negative exchange interactions between the two magnetic sublattices called A and B. In ferrimagnets, the magnetic moments of the A and B sublattices are not equal and result in a net magnetic moment. Above T_c , the susceptibility obeys the Curie-Weiss law (equ. 1.5) for paramagnets but with a negative intercept indicating negative exchange interactions (Figure 1.2). Ferrimagnetism can also occur in molecular magnets. An example is a dodecanuclear manganese molecule with an effective spin of $S = 10$ derived from antiferromagnetic interaction on Mn(IV) metal centres with Mn(III) and Mn(II) metal centres.³

Antiferromagnetism

For an antiferromagnetic material, the ordered two magnetic sublattice are in antiparallel fashion (magnetic exchange constant $J < 0$) and with exactly equal moments. So they cancel each other and the net moment is zero. Similar to ferrimagnetism, the Curie-Weiss temperature (θ) is also negative except with the positive deviation at low temperature (Figure 1.2).

The ordering occurs at a critical temperature, called the Néel temperature (T_N). Above T_N , the magnetic susceptibility is in the paramagnetic region and can be described as the Curie-Weiss law (equ. 1.5). At low temperature (below T_N), susceptibility approaches zero. Antiferromagnetic materials occur commonly among transition metal compounds such as FeO ($T_N = 198$ K) and metals such as Cr ($T_N = 308$ K).²

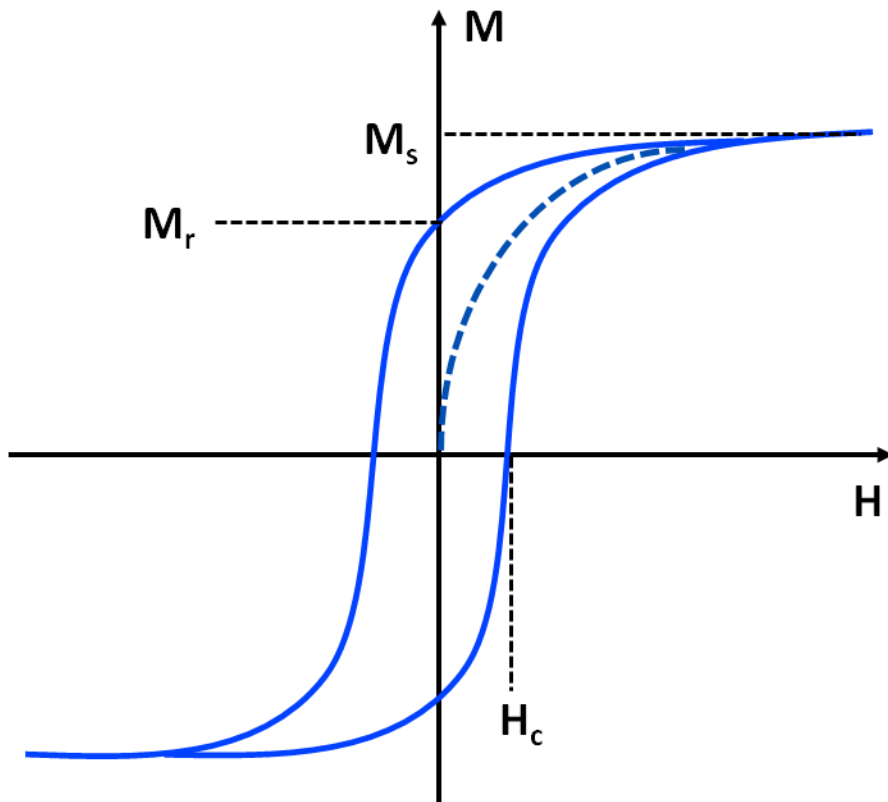


Figure 1.3. A typical magnetization curve of a ferro- or ferrimagnetic material, which shows saturation magnetization (M_s), the remanence magnetization (M_r), and the coercivity (H_c).

1.1.2 Hysteresis loop

Ferromagnetic and ferrimagnetic materials are usually what we consider as being magnetic (ie., behaving like iron). The remaining three (diamagnetism, paramagnetism, and antiferromagnetism) are so weakly magnetic that they are usually thought of as "nonmagnetic". Ferro- and ferrimagnetic materials are usually described by the hysteresis loop, where the magnetization M is plotted against the magnetic field strength H .⁴ Three important quantities in the hysteresis loop are the remanence (M_r for $H = 0$), the coercive force (reverse magnetic field required to eliminate magnetic induction in the sample: H_c for $M = 0$), and the saturation magnetization (M_{sat}). Figure 1.3 shows a typical curve, where the magnetization always falls behind the applied magnetic field because of magnetic domains inside the material.⁴ From the magnetization curve, one can easily find remanence magnetization M_r , the coercivity H_c , and the saturation magnetization M_s . The various hysteresis parameters are not solely intrinsic properties but are dependent on grain size, domain state, stresses, and temperature.

Both the ferro- and antiferromagnetic materials become paramagnetic above the Curie and Néel temperatures, respectively. Above those temperatures the thermal oscillations in the material are strong enough to overcome the interaction between aligned dipoles, flip and rotate them around, which destroys the aligned domains and no remanence magnetization (M_r) and the coercivity (H_c) in the hysteresis loop.

1.2 Magnetic nanoparticles and finite-size effects

Magnetic nanoparticles are of great interest to researchers from a wide range of disciplines, which include magnetic fluids,⁵ catalysis,⁶ biotechnology,⁷ magnetic resonance imaging (MRI),⁸ data storage,⁹ and environmental remediation.¹⁰ Magnetism is highly volume and temperature dependent, as this property arises from the collective interaction of atomic

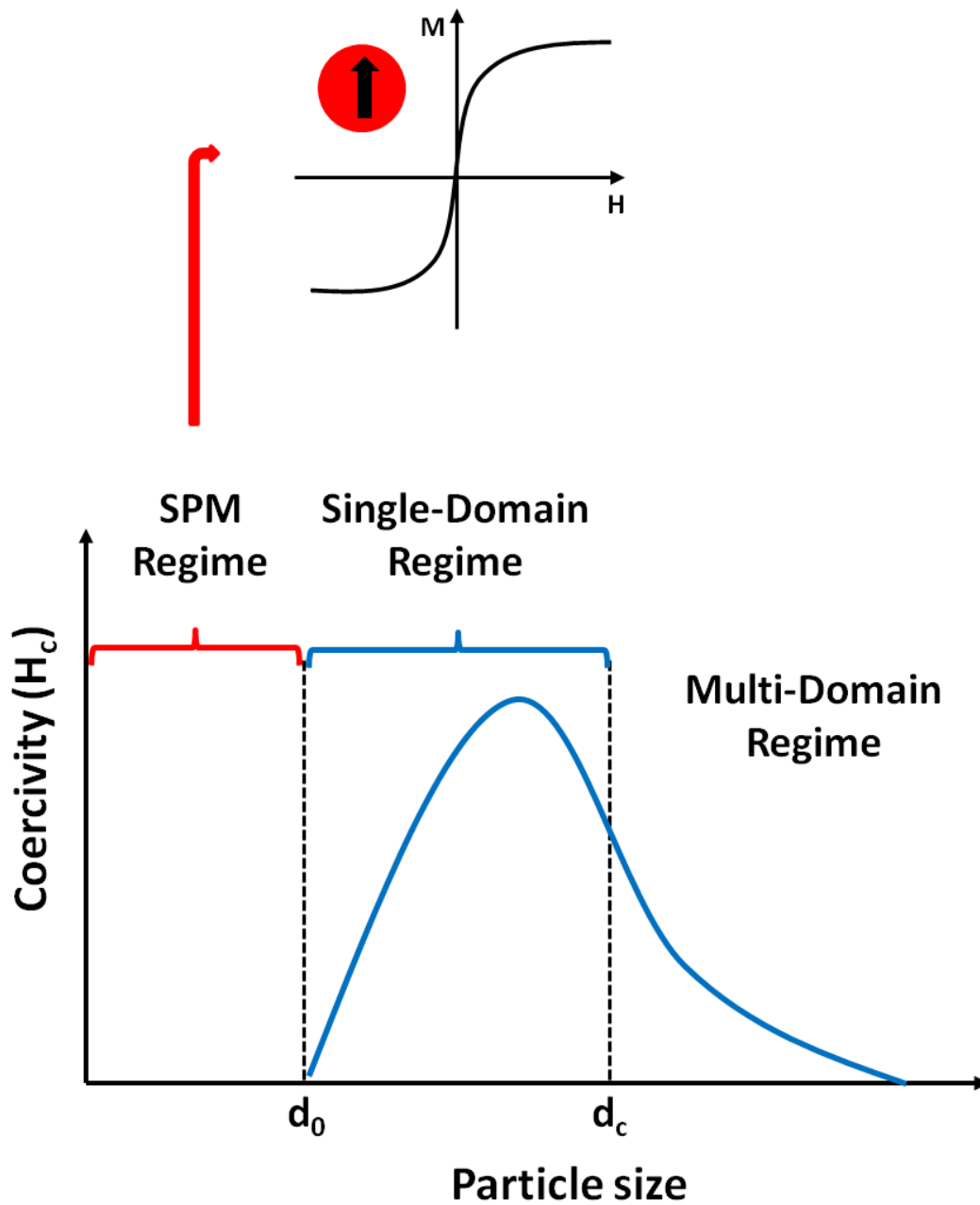


Figure 1.4. Schematic illustrating the dependence of magnetic coercivity on particle size. The coercivity falls to zero for superparamagnetic colloidal particles.

magnetic dipoles.¹¹ The two most studied finite-size effects in magnetic nanoparticles are the single domain limit and the superparamagnetic limit (Figure 1.4).

1.2.1 Single domain limit

In bulk magnetic particles, there is a multidomain structure, where regions of uniform magnetization are separated by domain walls. The formation of domain walls is a process driven by the balance between the magnetostatic energy (ΔE_{MS}), which increases proportionally with the volume of the material, and the domain-wall energy (E_{dw}), which increases proportionally with the interfacial area between domains. If the sample size is reduced, there is a critical volume below which it costs more energy to create a domain wall than to support the external magnetostatic energy of the single-domain state. When the ferro- or ferrimagnet becomes sufficiently small below a critical value d_c , the particles change from a state with multiple magnetic domains to one with a single domain.¹²

A single-domain state is reached below a critical diameter (d_c) when $\Delta E_{MS} = E_{dw}$. For a spherical particle:

$$d_c \approx 18(AK_{eff})^{1/2} / (\mu_0 M^2) \quad (1.8)$$

where A is the exchange constant, K_{eff} is anisotropy constant, μ_0 is the vacuum permeability, and M is the saturation magnetization. This critical diameter is typically less than 100 nm and depends on the material. It is influenced by contributions from various anisotropic energy terms. A single domain particle is uniformly magnetized with all the spins aligned in the same direction. The magnetization will be reversed by spin rotation, since there are no domain walls to move. This is why such high coercivity observed in small nanoparticles.¹³ Another source for the high coercivity in a system of small particles is the shape anisotropy.

1.2.2 Superparamagnetic limit and Superparamagnetism

If the size continues to decrease to a value d_0 , the thermal energy becomes comparable with that required for spin to flip directions, leading to the randomization of the magnetic dipoles in a short period of time. The magnetic anisotropy energy per particle which is responsible for holding the magnetic moments along a certain direction can be expressed as follows:

$$E(\theta) = K_{eff}V \sin^2 \theta \quad (1.9)$$

where V is the particle volume, K_{eff} is the anisotropy constant and θ is the angle between the magnetization and easy axis. The energy barrier $K_{eff}V$ separates the two energetically equivalent easy directions of magnetization. With decreasing particle size, the thermal energy, $k_B T$, exceeds the energy barrier $K_{eff}V$ and the magnetization is easily flipped. In the cases when $k_B T > K_{eff}V$ the particle behaves like a paramagnet, and instead of atomic magnetic moments, there is now a giant moment inside each particle. This system is named a superparamagnet. Such a system has no hysteresis and the data of different temperatures superimpose onto a universal curve of M versus H/T . At this point the particles do not have ferromagnetic properties anymore because their magnetic moments become randomly oriented. They behave paramagnetically even at temperatures far below the Curie and Néel temperatures. The size of particles where this happens is between 4 and 20 nm, depending on the material. Such small particles do not have permanent magnetic moments in the absence of an external field but can align with the external field easily even in weaker magnetic fields.

The relaxation time (τ) of the moment of a particle is given by the Néel-Brown expression¹⁴

$$\tau = \tau_0 \exp(K_{eff}V / k_B T) \quad (1.10)$$

where k_B is the Boltzmann's constant. If the particle magnetic moment reverses at times shorter than the experimental time scales, the system is in a superparamagnetic state; otherwise it is in the so-called blocked state. For superparamagnetic systems, the value of τ_0 is in the $10^{-9} - 10^{-11}$ s range.¹⁵ The temperature required to separate these two regimes is known as blocking temperature (T_B). It depends upon the effective anisotropy constant, size of the particles, applied magnetic field, and experimental measuring time. For example, the experimental measuring time with a magnetometer (roughly 100 s) gives:

$$T_B = K_{eff}V / (30k_B) \quad (1.11)$$

The blocking temperature (T_B) can be determined experimentally by zero-field-cooled (ZFC)/field-cooled (FC) dc magnetometry measurements. In a standard procedure, the sample is cooled from room temperature with no applied magnetic field, and then warmed up under a small magnetic field of about 100 Oe. As temperature increases in ZFC measurement, the thermal energy disturbs the system and more moments acquire the energy needed to align with the external field. Eventually, the number of unblocked, aligned moments reaches a maximum at T_B . Above the T_B the thermal energy is strong enough to randomize the magnetic moments leading to a decrease in magnetization. A distribution of the particle sizes results in a distribution of the blocking temperatures. Figure 1.5 shows the ZFC and FC magnetization versus temperature curves for 2.8 nm Mn:CdSe particles. The T_B can be determined experimentally by the peak position in the ZFC plot. For superparamagnetic colloids, the $M-H$ curve does not show any hysteresis when the measurement is performed at a temperature well above the blocking temperature.

If there are magnetic interactions between nanoparticles that have a strong influence on the superparamagnetic relaxation, the behavior of the system can become even more complicated.

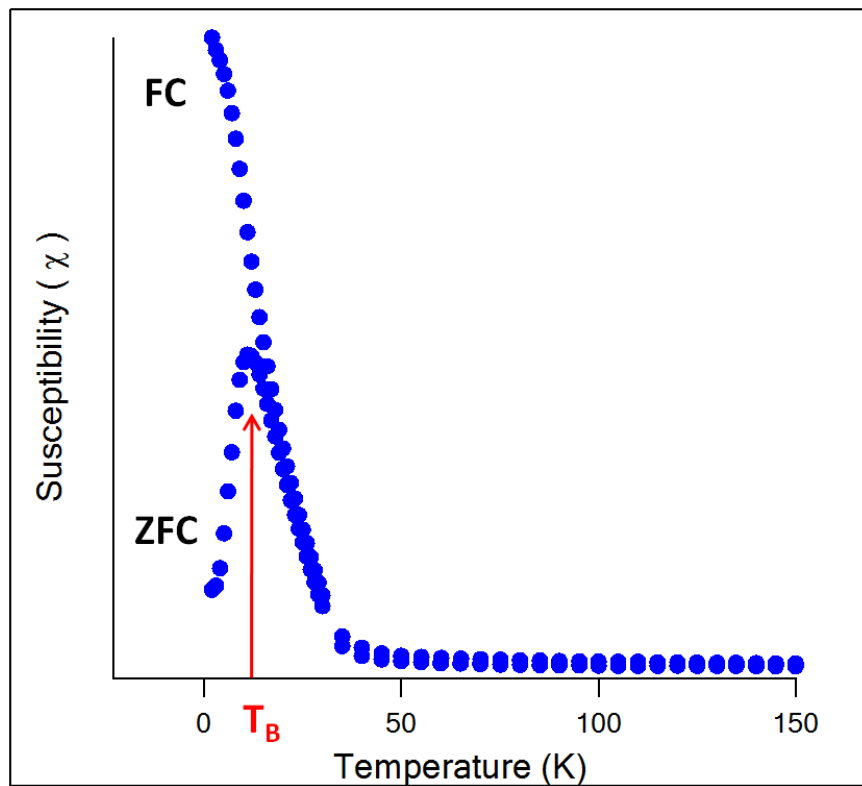


Figure 1.5. The ZFC and FC curves of 2.8 nm Mn:CdSe nanoparticles in diameter with blocking temperature (T_B) 12 K.

The primary interactions present in a system of small particles are: dipole-dipole interactions, direct exchange interactions for touching particles, superexchange interactions for metal particles in an insulating matrix, and RKKY (Ruderman-Kittel-Kasuya-Yosida) interactions for metallic particles embedded in a metallic matrix.¹⁶ Dipolar interactions are almost always present in a magnetic particle system and typically are the most relevant. They are of long-range character and anisotropic. From an experimental point of view, the problem of interparticle interactions is very complex. First, it is very difficult to separate the effects of interactions from the effects caused by the random distributions of sizes, shapes, and anisotropy axes. Second, one sample can simultaneously present more than one interaction, making it even more complicated to assign the observed properties to specific interactions.

Superparamagnetic nanoparticles are very attractive for a broad range of biomedical applications since the risk of forming agglomerates is negligible at room temperature. Other application areas include energy and data storage, ferrofluid technology, and magnetorheological polishing. One key feature of superparamagnetic nanoparticles is that they have no memory effect, which allow the thermal energy to flip the dipoles in random directions and cause them to become neutral again almost immediately after the field is turned off. Such individual nanoparticles have a large constant magnetic moment and behave like a giant paramagnetic atom with a fast response time to applied magnetic fields and a negligible remanence and coercivity.

1.2.3 Surface Effects

The physical properties of nanoparticle, such as colloidal quantum dots (QDs), are strongly influenced by the high surface to volume ratio in these materials.¹⁷⁻¹⁹ As particle size decreases, the percentage of the surface atoms in a nanoparticle increases, which implies that surface and interface effects become more important. Owing to this large surface/volume ratio,

the surface spins make an important contribution to the magnetization. Typical surface effects are related to the symmetry breaking of the crystal structure at the boundary of each particle. This local breaking of the symmetry might lead to changes in the band structure, lattice constant or/and atom coordination. Under these conditions, some surface and/or interface related effects can occur, like surface anisotropy and, under certain conditions, core-surface exchange anisotropy can also occur. Surface ligation of organic ligands, used to stabilize the magnetic nanoparticles, also have an influence on their magnetic properties, that is, ligands can modify the anisotropy and magnetic moment of the metal atoms located at the surface of the nanoparticles.²⁰ Surface ligation of an organic passivating layer onto a non-magnetic quantum dot leads to passivation of dangling bonds but also will impact the structure and magnetic properties of the QD.^{21,22}

1.3 Diluted magnetic semiconductors (DMSs) and diluted magnetic semiconductor quantum dots (DMSQDs)

1.3.1 Diluted magnetic semiconductors (DMSs)

The incorporation of impurities or defects into semiconductor lattices is a thriving area of physical and synthetic inorganic chemistry. One of the most interesting categories of dopants in semiconductors is magnetic ions, as the magnetic properties are directly influenced by the strength of the overlap between the d-orbitals of the magnetic ion and the valence (p-d exchange) or conduction (s-d exchange) band of the semiconductor. Semiconductors containing magnetic impurities have been studied for several decades and have come to be known as “diluted magnetic semiconductors”. Interest in diluted magnetic semiconductors (DMSs) originally arose from the so-called “giant Zeeman effects” observed in the excitonic levels. Dilute magnetic

semiconductors (DMSs) are recognized as an important class of materials with potential for spin-based electronic and magneto-optical applications.^{23,24}

The charge carriers in semiconductors will significantly affect the properties of a material. In intrinsic semiconductors, conduction band electrons come from the excitation of electrons in the valence band. The intrinsic carrier density $n_i = p_i$, is a function of temperature and band gap energy. In DMSs, charge carriers can also come from dopants, where conduction band electrons arise from donors and valence band holes from acceptors. One well-studied approach to obtaining spin-polarized carriers for data-storage devices is the use of DMSs, which is created by doping ions having a net spin like Mn, Fe, or Co into a semiconducting host such as GaAs, ZnO, or GaN. The interaction among these spins leads to ferromagnetic order at low temperatures, which is necessary to create spin-polarized carriers.

In DMS materials, Mn(II) doped III-V semiconductors can exhibit ferromagnetism due to hole mediated exchange interactions via the Ruderman–Kittel–Kasuya–Yosida (RKKY) model.^{16,25} More specifically, Mn-doped GaAs, in which the Mn dopant provides both a magnetic moment and a spin-polarized charge carrier, has attracted considerable interest as a spintronics material. In Mn(II) doped II–VI compounds, the nearest neighbor antiferromagnetic exchange is observed.²⁴ The onset of ferromagnetic (FM) exchange has been achieved in p-type Mn(II) doped II-VI compounds (Mn:CdTe, Mn:ZnTe),^{26,27} as well as through photogenerated carriers in Mn:CdSe.²⁸ The results on II-VI DMS systems suggest that FM exchange can be achieved if exchange interactions in the II-VI materials can be enhanced via a carrier mediated process.

1.3.2 Diluted magnetic semiconductors quantum dots (DMSQDs)

Colloidal semiconductor nanocrystals, also named “quantum dots” (QDs), consist of a few hundred to a few thousand atoms. The quantum confinement effect arises from the small size

of the nanoparticles when the semiconductor is smaller than the natural Bohr radius. This is defined by an increasing bandgap accompanied by the quantization of the energy levels to discrete values. Systematically incorporating paramagnetic ion impurities onto the metal lattice sites for quantum dots (QDs)²⁹⁻³¹ represents an exciting materials development area for generating a new class of dilute magnetic semiconductor quantum dots (DMSQDs). DMSQDs hold potential for spin-based electronic applications,²⁴ as well as the investigation of fundamental magnetic exchange in a well-defined confined environments. DMSQDs will be strongly influenced by the surface states and doping sites (core vs. surface) to the observed magnetic behavior.^{32,33}

In II-VI QDs the intentional doping of paramagnetic ions into the core of a QD lattice can be difficult to achieve due to the tenants of nucleation theory,³⁴ the high surface energies for ion addition to the face,³⁵ and the propensity for QDs to exhibit self-annealing.³⁶ In recent studies, the difficulty of doping has been overcome by the use of pre-doped molecular clusters that act as critical nuclei for formation of the doped QDs.^{30,37} The use of the molecular cluster has been shown to allow the statistical incorporation of the magnetic impurity ions onto the metal T_d sites. The breakthrough in doping strategies has led to the observation of an optically induced excitonic magnetic polaron (EMP) in Mn: CdSe QDs³⁸ and the report of a giant Zeeman splitting in Mn: CdSe quantum nanoribbons³⁹ due to kinetic s-d mixing ($N_0\alpha$) between the Mn d-levels and conduction band levels of the semiconductor. The orbital exchange should be size dependent due to the quantum confinement effects on the conduction band⁴⁰ and will be influenced by the presence of surface states whose contribution will increase as the surface/volume ratio increases. The participation of surface donor states in QDs due to ligation may lead to intrinsic carriers³² which may induce a carrier mediated process in these DMSQD systems. The participation of surface states was reported to be critical in explaining the observed magnetic exchange in

undoped CdSe QDs measured by XMCD,³² and the onset of Pauli-paramagnetism (PPM) in CdSe measured by SQUID.⁴¹

In DMSQDs the perturbation of the physical properties by the defect ion is influenced by the size of the semiconductor due to quantum confinement effects. Therefore, probing the incorporation of magnetic ions into a semiconductor quantum dot is a fascinating field to investigate. By systematically tuning the lattice composition of the paramagnetic guest ion and the QD size, it might be possible to efficiently tune the band parameters and interactions within this quantum dot system, which would allow probing the existence of carriers and spin wave formation.

When the size of DMSs decreases to nanoscale, finite-size effects resulted from the quantum confinement of the electrons is one of the key issues dominating the magnetic properties. The defects both on the surface and within the nanoparticles could also significantly affect the magnetic properties. When the size of a ferro- or ferrimagnet decreases to a certain critical value, the particles change from a state with multiple magnetic domains to one with a single domain. If the size continues to decrease, the thermal energy will become comparable with the energy required for spin to flip directions, which leads to the randomization of the magnetic dipoles in a short period of time. Such small particles do not have permanent magnetic moments in the absence of an external field but can respond to an external magnetic field. They are referred to as superparamagnetic quantum dots (SPM QDs). They have found widespread use in many traditional areas including magnetic data storage, ferrofluid technology, magnetorheological polishing, and energy storage.¹⁴ They also hold great potential for many other applications related to biomedical research. To this end, SPM QDs have been exploited for labeling and separation of DNAs, proteins, bacteria, and various biological species, as well as

applied to magnetic resonance imaging (MRI), guided drug delivery, and hyperthermia treatment of cancer.¹⁴

1.4 Magnetic studies of DMSs and DMSQDs

In diluted magnetic semiconductors, unpaired spins from transition metal ions allow magnetic measurements to be used to probe both the dopant's magnetic behavior and its interactions with the lattice. Methods employed in these analyses include SQUID magnetometry and electron paramagnetic resonance (EPR) spectroscopy, which are known to help bring insight onto the oxidation state of the dopant ion and the magnetic exchange interactions that exist in the paramagnetically doped material.

1.4.1 Superconducting Quantum Interference Devices (SQUID) Magnetometry

SQUID measurements are useful in determining the ensemble magnetic properties of interactions between magnetic ions. DC magnetic measurements determine the equilibrium value of the magnetization in a sample. In DC SQUID measurement, temperature dependent Zero-field cooled (ZFC) and field cooled (FC) susceptibility measurements are generally performed in order to get insight on the nature of the magnetic interactions, which can be paramagnetic, ferromagnetic, and antiferromagnetic. The difference between ZFC and FC magnetization indicates that the free energy has a complicated structure below a critical temperature. While in field sweep magnetization measurement, experimental parameters such as saturation magnetization (M_s), the remanence magnetization (M_r), and the coercivity (H_c) can be obtained from hysteresis (Figure 1.3), which help determine if a material is ferromagnetic. Comparing to DC measurements, AC measurements yield information about magnetization dynamics. In AC magnetic susceptibility measurement, a small AC drive magnetic field ($2 \times 10^{-4} - 2$ Oe) is superimposed onto the DC field, creating a time-dependent moment in the sample. The

frequency range in AC measurements can vary between 0.01 Hz and 1000 Hz, permitting a full determination of the real χ' and imaginary χ'' components. The AC susceptibility is important for systems with spin frustration effects (spin glass or cluster glass phases) and SPM nanoparticles.

SQUID magnetometry is a powerful technique that has been used to study the nature of magnetic interaction within doped nanomaterials. Depending on the interactions that exist and the level of doping, the DMSs can exhibit a number of different types of behaviors including paramagnetism, ferromagnetism, antiferromagnetism, and spin glass behaviors.²⁴ In 4 nm 1% Mn:CdSe DMSQDs, a transition of superparamagnetic (SPM) character with a coercive field was observed after thermal annealing of the QDs.³⁷ Magnetic susceptibility and magnetization studies confirm that the magnetic effects can be explained in terms of a doubling of the Mn cluster domain content. Furthermore the Mydosh parameter obtained from AC measurements (0.16) confirmed the SPM character of the QDs.

1.4.2 Electron Paramagnetic Resonance (EPR) Spectroscopy.

EPR provides insight onto the magnetic properties of the paramagnetic ions in a material.^{29,35} These experiments are performed in a microwave cavity between two magnets. The sample is then placed inside an evacuated and sealed quartz tube. Usually, the field scan is performed in a fixed microwave frequency. The energy levels of the magnetic ion split under a magnetic field, which is called Zeeman effect. As the field is scanned the sample will absorb microwave radiation when the energy of the radiation corresponds to an allowed transition between two spin levels ($\Delta m_s = \pm 1$).

$$h\nu = \Delta E = g\beta H \quad (1.12)$$

$$g = h\nu / \beta H_r = 714.4775\nu / H_r \quad (1.13)$$

where h is Planck's constant, ν is the frequency in GHz, g is the Landé g-factor, β is the Bohr magneton, and H is the magnetic field in G. From the position of the EPR peak (H_r), the g-factors of a material can be determined. For some transition metal ions with weak EPR signals, low temperature EPR measurements can be employed (below 77K) to reduce the effect of spin-lattice coupling.

Generally EPR research has been done at the commercially available instruments in X-Band (9.5 GHz), Q-Band (35 GHz), and W-Band (95 GHz). Compared to conventional EPR techniques, high frequency/field EPR (HF-EPR) measurements with frequency up to more than 400 GHz offer better resolution with respect to g-value.⁴² This can be seen in equ. 1.13, where the resonance field H_r is proportional to the frequency ν :

$$H_r = h\nu / g\beta \propto \nu \quad (1.14)$$

The HF-EPR setup at the National High Magnetic Field Laboratory (NHMFL), Tallahassee, FL. operates in transmission mode and employs oversized cylindrical waveguides. Microwave detection is performed with a low-noise, fast-response InSb hot-electron bolometer (QMC Ltd.). Modulation amplitude and microwave power were optimized for high signal-to-noise ratio and narrow peaks.

Using EPR, the crystal field and orbital admixture (s-p-d) between the paramagnetic ions and the diamagnetic host lattice can be probed, as the ion's g-value and the hyperfine constant are both elementally specific and respond to changes in local bonding, orbital admixtures, and crystal-field influences.^{43,44} In DMSQDs guest ion incorporation into the host lattice may lead to both core and surface incorporation (Figure 1.6), which is dependent on the preparative route is inhomogeneous (surface-only) or homogeneous (surface and core). Mn^{2+} hyperfine splitting in bulk CdSe has been shown to be $62 * 10^{-4} \text{ cm}^{-1}$,⁴⁵ while studies of Mn^{2+} doped ZnS have shown that the dopant resides in the core and surface with hyperfine splittings of $64.5 * 10^{-4} \text{ cm}^{-1}$, and

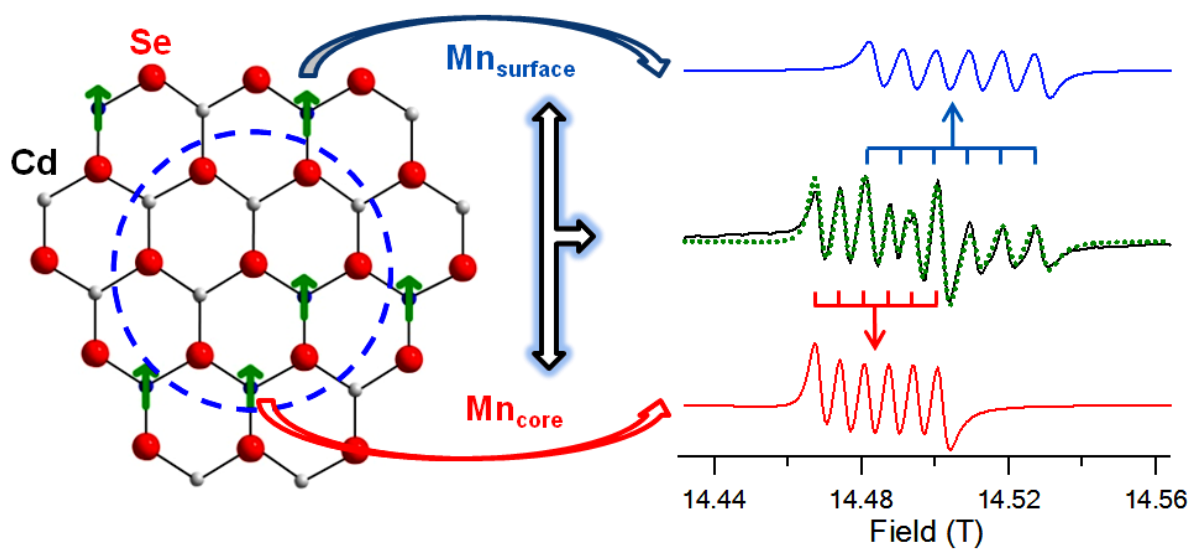


Figure 1.6. Schematic representation of a QD depicting the surface and core doping sites for a 2 nm Mn:CdSe QD, showing both the core and surface site for Mn(II), and theoretical fit and deconvolution of the 406.4GHz HF-EPR spectra allowing definitive assignment of discrete sites for the Mn(II) occupying a substitutional Cd(II) site within the core (red) and on the surface (blue).

$89 * 10^{-4} \text{ cm}^{-1}$ respectively.⁴⁶ In $\text{Cd}_{1-x}\text{Mn}_x\text{Se}$ prepared by Mikulec et al, the Mn^{2+} had a hyperfine splitting of $83 * 10^{-4} \text{ cm}^{-1}$ and was therefore attributed to being near the surface.³⁶ In Mn^{2+} doped CdSe QDs made by Magana et al, the hyperfine splitting of $62 * 10^{-4} \text{ cm}^{-1}$ was obtained and therefore attributed to the Mn(II) ion in the core of the QDs.³⁷ The Mn^{2+} doped ZnSe prepared by Norris, et al showed a hyperfine splitting of $60.4 * 10^{-4} \text{ cm}^{-1}$, allowing one to conclude that the guest ion was substitutionally replacing Zn inside the host lattice.⁴⁷

Although low frequency EPR has been carried out on QDs, the use of HF-EPR allows for the spectral resolution^{42,48} of the individual surface and core components in the EPR spectrum and therefore in-depth insight into the effects of size and passivation. For these studies, Mn(II) doped into a II-VI QD is an ideal probe of a II-VI QD microenvironment since the II-VI lattice is diamagnetic while the Mn(II) ion exhibits a sextet hyperfine splitting arising from the $S = 5/2$, $I = 5/2$, $L = 0$ ground state (${}^6\text{A}_1$), which is sensitive to changes in crystal field and orbital admixture.⁴³ Discrete surface and core sites within the QD (Figure 1.6) are assigned by HF-EPR, demonstrating the effect of surface passivation by an organic ligand strongly perturbs the surface layer, but exhibits no impact on the core of the QD. A more covalent core site has relatively high g -factor and small ${}^{55}\text{Mn}$ hyperfine interaction ($g = 2.0042$, $A = 66.8 \text{ G}$), and $g = 2.0014$, $A = 90.8 \text{ G}$ obtained for a more ionic surface site.

1.5 Conclusion

Diluted magnetic semiconductor nanomaterials are an exciting area of physical and synthetic inorganic chemistry with potential for spin-based electronic and magneto-optical applications. It has been shown that the magnetic properties of DMSs and DMSQDs are strongly dependent on the type of the dopant, host lattice, size, and surface effect. The recently found superparamagnetic (SPM) phase of DMSQDs is promising for widespread use in many

traditional areas. SQUID magnetometry and EPR spectroscopy are very important tools for providing useful information on the oxidation state of the dopant, location of dopant, and the nature of magnetic interaction in the material.

The upcoming chapters outline our investigation of the size- and site-dependent magnetic properties of DMSQDs. The size dependent magnetic properties of Mn(II) doped CdSe QDs were studied using a SQUID, which demonstrated that the carriers mediate the Mn(II)-Mn(II) ferromagnetic interaction by the RKKY model leading to the SPM behavior of the small QDs (Chapter 2). The site occupation of dopant (Mn^{2+}) in CdSe lattice was studied using high frequency EPR. The ratio of the two sets of hyperfine splitting signal has linear relationship with the surface to volume ratio of the QDs, which enabled us to identify the surface and core Mn^{2+} sites of Mn:CdSe QDs (Chapter 3). The Cr ion doped ZnSe QDs were made by single cubic source precursor. The formation of ZnCr_2Se_4 spinel structure was approved by XANES, and ${}^4\text{T}_{2g} \rightarrow {}^4\text{T}_{2g}$ transition of Cr (III) ion in absorption spectra (Chapter 4). The preliminary experimental data of concentration dependent magnetic properties of Mn(II) doped CdSe QDs are included in chapter 5.

CHAPTER TWO

INVOLVEMENT OF CARRIERS IN THE SIZE-DEPENDENT MAGNETIC EXCHANGE FOR Mn:CdSe QUANTUM DOTS*

* *J. Am. Chem. Soc.* **2011**, *133*, 7482-7489.

The magnetic behavior for Mn:CdSe (0.6%) quantum dots (QDs) exhibits size dependent magnetic exchange mediated by the concentration of intrinsic carriers which arise from surface states. High temperature paramagnetic behavior that can be fit to a Brillouin function with weak low temperature antiferromagnetic (AFM) coupling is observed for the large Mn:CdSe (5.0 nm and 5.8 nm) QDs. The 2.8 nm and 4.0 nm Mn:CdSe QDs display a size independent blocking temperature (T_B) at 12 K, decreasing coercivity with increasing size, and a lowering of the activation barrier for spin relaxation as the QD is increased in size. The magnetic behavior is inconsistent with classical domain theory behavior for a superparamagnet (SPM) but can be accounted for a carrier mediated RKKY model. Fitting the susceptibility data reveals a Pauli-paramagnetic (PPM) component that is believed to arise from the presence of carriers. The carrier density is observed to scale with the surface to volume ratio in the QDs indicating the carriers arise from surface states which are weakly localized resulting in the onset of long-distance carrier-mediated RKKY exchange inducing overall ferrimagnetism in the Mn:CdSe QDs when the carrier concentration is above a critical threshold.

2.1 Introduction

Dilute magnetic semiconductors (DMSs) are recognized as an important class of materials with potential for spin-based electronic and magneto-optical applications.^{23,24,29,31,39,49}

In DMS materials Mn(II) doped III-V semiconductors can exhibit ferromagnetism due to hole mediated exchange interactions via the Ruderman–Kittel–Kasuya–Yosida (RKKY) model,^{16,25} while in Mn(II) doped II–VI compounds, the nearest neighbor antiferromagnetic exchange is observed.²⁴ The onset of ferromagnetic (FM) exchange has been achieved in p-type Mn(II) doped II-VI compounds (Mn:CdTe, Mn:ZnTe),^{26,27,50} as well as through photogenerated carriers in Mn:CdSe.²⁸ The results on II-VI DMS systems suggest that FM exchange can be achieved if exchange interactions in the II-VI materials can be enhanced via a carrier mediated process.

The study of dilute magnetic semiconductors quantum dots (DMSQDs) based on CdSe are ideal for probing the fundamental interplay of charge-, lattice- and magnetic degrees of freedom in quantum confined environments reflecting the exquisite control over the energies of the conduction and valence bands in these materials due to quantum confinement effects.^{29,31,35,40} In addition, the participation of surface donor states in CdSe QDs due to ligation may lead to intrinsic carriers^{32,41} that may induce a carrier mediated process in these DMSQD systems. To date, only limited reports on FM exchange have been reported for Mn(II) doped II-VI QDs.^{33,37} In general the limited reports reflect the difficulty in achieving intentional doping of paramagnetic ions into the core of a quantum dot (QD) due to the tenants of nucleation theory,³⁴ the high surface energies for ion addition to a growing QD facet,³⁵ and the propensity for QDs to exhibit self-annealing.³⁶ Although the difficulty of doping has been overcome by the use of pre-doped molecular clusters that act as critical nuclei for formation of the doped QDs,^{30,31,37} allowing statistical incorporation of magnetic impurity ions onto the metal tetrahedral (T_d) sites, no studies have appeared investigating the size dependent magnetic behavior for Mn:CdSe QDs. The exchange behavior will be influenced by QD size, dopant concentration, and the site of doping (core vs. surface),^{32,33,41} providing a carefully controlled study of size dependent

exchange in a DMSQD at a fixed dopant concentration which is important to understand the fundamental magnetic exchange in a well-defined environment.

In this manuscript, the size dependent magnetic properties for 0.6% doped Mn:CdSe QDs passivated by dodecylamine is interrogated. The Mn:CdSe QDs are isolated as spherical, wurtzite nanocrystals with diameters of 2.8 nm, 4.0 nm, 5.0 nm, and 5.8 nm. The doping level is constant throughout the samples due to the use of a pre-doped single source precursor and is confirmed by SQUID spin counting and X-ray fluorescence methods. In the Mn:CdSe QDs, paramagnetic (PM) behavior is observed for the 5.0 nm and 5.8 nm QDs, while a size independent magnetic transition at 12 K and size dependent coercivity is observed for the 2.8 nm and 4.0 nm QDs. The SQUID data for the larger QDs can be fit to a high temperature paramagnetic behavior exhibiting antiferromagnetic coupling at low temperature. Analysis of the Curie-Weiss law plot for the 2.8 and 4.0 nm QDs indicates the participation of Pauli-paramagnetism (PPM) attributed to intrinsic carriers arising from surface states in the QDs generating ferromagnetic (FM) exchange below the blocking temperature. Consistent with the assignment of surface states producing carriers within the QD, a plot of the temperature independent Pauli-paramagnetism versus QD size reveals a direct correlation between the observed magnetic moment and the QD size. It is believed the carriers in the smaller QDs mediate the exchange interaction in these single domain Mn:CdSe QDs, which leads to overall ferrimagnetism in the samples.

2.2 Experimental

Chemicals. Dodecylamine (DDA) (98+%, Alfa Aesar), MnBr₂ (anhydrous, 99%, Alfa Aesar), toluene (>99.9%, EMD Chemicals) and methanol (MeOH) (>99.8%, VWR) were used as supplied. Li₄[Cd₁₀Se₄(SeC₆H₅)₁₆] (Cd₁₀) was prepared as described previously.⁵¹

Dodecylamine (DDA) passivated Mn: CdSe (0.6%). DDA passivated Mn: CdSe (0.6%) with a 5–6% size distribution was prepared by the reaction between the single source precursor $\text{Li}_4[\text{Cd}_{10}\text{Se}_4(\text{SeC}_6\text{H}_5)_{16}]$ (Cd_{10}) and MnBr_2 in DDA, as described previously.^{37,52} Briefly, the QDs are prepared by the dissolution of 200 mg (0.05 mmol) of Cd_{10} in ~20 mL of DDA at 100 °C under N_2 . To the solution, 4.34 mg (0.02 mmol) MnBr_2 is added and the reaction allowed to stir for 1 h to induce ion exchange into the Cd_{10} cluster. The reaction mixture was heated to 220 °C (10 °C/min) inducing QD growth. The solution was cooled to room temperature, dissolved into ~10 mL of toluene, precipitated by the addition of ~15 mL of MeOH, and centrifuged to isolate the QDs (4×). The QDs were dissolved in a minimum of pyridine, precipitated (3×) by the addition of hexane to remove Mn(II) impurities, and isolated by centrifugation. Sequential dissolution/re-precipitation steps has been shown to effectively remove unreacted Mn(II).^{30,36,37} QD size, morphology, and structure were analyzed by transmission electron microscopy (TEM) and confirmed with powder X-ray diffraction (pXRD) and UV-Vis spectroscopy. The Mn doping level was analyzed by X-ray fluorescence (XRF) found to be 0.006 mole fraction (~0.6%) relative to Cd for all the samples.

Analysis. QD size, dispersity, and morphology were analyzed by TEM using a JEOL-2010 microscope operated at 200 kV. The QDs were dispersed on holey carbon (400 mesh) from a toluene solution. Size dispersities were measured by averaging ~100 individual dots from the TEM. Optical absorption was analyzed in a 1-cm cell in toluene using a Cary 50 UV-Vis spectrophotometer. The absorption maximum for the first exciton was used to estimate the QD size.⁵³ Powder X-ray diffraction was carried out on a Rigaku DMAX 300 Ultima 3 diffractometer using Cu K_α ($\lambda = 1.5418 \text{ \AA}$) with the d-spacing calibrated to a Si standard to verify crystal motif.

Elemental composition analysis for Mn^{2+} , Cd^{2+} and Se^{2-} was carried out in triplicate on an Oxford Instruments ED₂₀₀₀ X-ray fluorescence spectrometer with a Cu-K_α source. The atomic concentration was measured for Mn^{2+} at 5.9 KeV, Cd^{2+} at 23.1 keV and Se^{2-} at 11.2 keV. For a standard XRF measurement, the powdered samples were completely dissolved in 90% HNO_3 , heated to remove excess NO_x , and then diluted to ~3 mL with a 2% HNO_3 solution (to allow compatibility with the XRF sample holder). Calibration curves were generated using commercially prepared 1000 ppm elemental standards in 2% HNO_3 , which results in accuracies of 5 ppm for Mn^{2+} , 3 ppm for Cd^{2+} and 4 ppm for Se^{2-} .

Magnetic Measurements. Magnetic data on 20–40 mg powdered samples of the QDs was measured on a Quantum Design MPMS XL7 SQUID magnetometer. Zero-field cooled (ZFC) and field cooled (FC, 0.01T) measurements were collected for dc-susceptibility. Ac susceptibility was measured between 1 to 1000 Hz. The temperature dependent dc- and ac-magnetic susceptibility measurements were measured between 2 to 300 K. Field dependent magnetization (M) data was collected between -7 to $+7$ T. The experimental data was fit to a Brillouin function, assuming $g = 2.0$, S is a variable, and the Mn(II) doping concentration in $\text{Mn}_x\text{Cd}_{1-x}\text{Se}$ is $x = 0.006$.

2.3 Results

The Mn:CdSe QDs were doped at 0.6% Mn(II) via the reaction of the “single-source” Mn(II) doped $\text{Li}_4[\text{Cd}_{10}\text{Se}_4(\text{SeC}_6\text{H}_5)_{16}]$ (Cd_{10}), which allows consistent Mn(II) ion incorporation into the QD lattice for the studied sizes.³⁷ Growth of the QD is achieved at 220 °C resulting in spherical, wurtzite QDs passivated by DDA with 5–6% size dispersity based on TEM. In Figure 2.1, the optical spectra, pXRD, and TEM data are shown for the isolated Mn:CdSe QDs. The optical absorption (Figure 2.1A) (dotted lines) and photoluminescence (PL) spectra (solid lines)

can be fit to 2.8 nm, 4.0 nm, 5.0 nm and 5.8 nm in diameter for the isolated QDs. The color coding (2.8 nm (blue), 4.0 nm (green), 5.0 nm (black), and 5.8 nm (red)) for the experimental data is maintained throughout the text to simplify size identification for all experimental measurements. The sizes of the QDs measured by analysis of the optical data are confirmed by TEM analysis (Figure 2.1B). The concentration of Mn(II) in the CdSe QDs is on average 0.6% doping per QD as experimentally measured by XRF analysis and spin counting via SQUID magnetometry by fitting to Brillouin function. The Mn(II) ion is assigned as a substitutional dopant on the Cd metal ion site based upon analysis of the total metal ion (Mn + Cd) to chalcogenide (Se) mole ratio, which yielded a value of 0.9:1 similar to the value observed for the undoped CdSe QD of 0.9:1. The Mn(II) doping will exhibit a Poisson distribution within the QD ensemble, but on average represents *~two* Mn(II) ions in the 2.8 nm QD, *~four* Mn(II) ions in the 4.0 nm QD, *~seven* Mn(II) ions in the 5.0 nm and *~ten* Mn(II) ions in the QD in the 5.8 nm QD distributed statistically between the core and surface of the QD.

Powder XRD (Figure 2.1C) allows assignment of a wurtzite crystal structure for the larger QDs, but can be interpreted as either cubic (zinc blende) or wurtzite for the smaller QDs. In QDs below 4 nm, the observation of a pseudo zinc blende pXRD pattern can be misinterpreted as a pure zinc blende structure since the presence of one to two stacking faults within the wurtzite Mn:CdSe QDs can lead to loss of the (103) reflection intensity at 45 degree.^{54,55} Analysis of TEM-selected area electron diffraction (ED) data (Figure 2.1D) allows definitive assignment of wurtzite crystal morphology for all sizes of the Mn:CdSe based upon the observation of the (002), (110), and (201) reflections in the TEM-ED micrograph. The assignment of wurtzite crystal morphology from the TEM electron diffraction pattern suggests the loss of intensity for the 45 degree reflection in the pXRD is due to stacking faults in the small QDs as observed previously and not to formation of a zinc blende phase at this size scale.

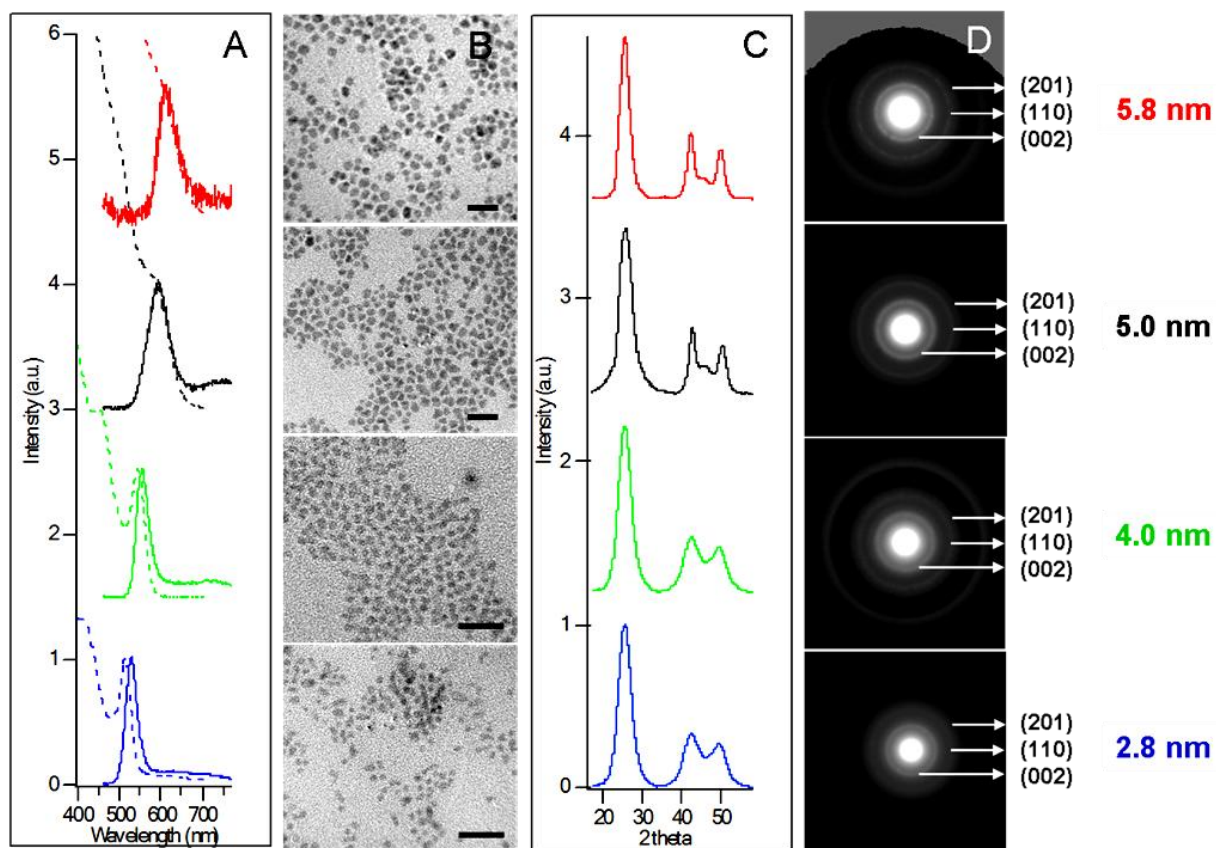


Figure 2.1. Characterization data for 2.8 nm, 4.0 nm, 5.0 nm, and 5.8 nm (in diameter) 0.6 % Mn:CdSe QDs A) absorption (dashed) and photoluminescence (solid) spectra, B) TEM images (scale bar = 20 nm), C) Powder XRD patterns, and D) electron diffraction TEM images. The figure is color coded for the QD sizes as noted in the image.

In Figure 2.2A, the size dependent zero-field-cooled (ZFC) and field-cooled (FC, 100 Oe) susceptibility (χ) plots for the Mn:CdSe QDs measured by SQUID magnetometry are shown. The susceptibility plots are plotted relative to emu/mol of QD. The susceptibility plots for the 5.0 and 5.8 nm Mn:CdSe samples exhibit paramagnetic (PM) behavior, as expected for <1% doping levels in the Mn:CdSe samples.²⁴ The 2.8 nm and 4.0 nm Mn:CdSe samples show non-paramagnetic behavior with a clearly observed size-independent magnetic transition at 12 K. Field dependent ZFC/FC SQUID measurements (Figure 2.3A) on the 2.8 nm Mn:CdSe at 50 Oe, 100 Oe, and 500 Oe indicate the 12 K magnetic transition is field independent. No transitions are observed for the 5.8 nm sample up to 100 Oe (Figure 2.3B). Temperature dependent M vs. H plots (Figure 2.2B) for the four samples indicate a saturation value (M_{SAT}) for the samples above 2T that is size dependent but exhibits no clear correlation with QD size. The slower saturation may reflect the participation of spins at the QD surface.⁵⁶

Size dependent low temperature coercivity is observed for the 2.8 nm (0.29 T at 2 K) and 4.0 nm (0.16 T at 2 K) Mn:CdSe QDs in the M vs. H plots below 20 K (Figure 2.2B). No coercivity is observed for the 5.0 nm and 5.8 nm Mn:CdSe samples. The coercivity in the small QDs decreases to 0 T near 20 K for the 2.8 nm and 4.0 nm Mn:CdSe QDs, which is typical for blocking temperature behavior observed for a superparamagnetic (SPM) material. The experimental susceptibility curves are consistent with PM behavior in the 5.0 and 5.8 nm Mn:CdSe QD, while a more complex magnetic behavior reflective of SPM or spin-glass behavior is observed for the 2.8 nm and 4.0 nm Mn:CdSe QD samples. A plot of the temperature dependent magnetization versus H/T (Figure 2.4) confirms the magnetization of the 5.0 and 5.8 nm Mn:CdSe can be described as PM. The susceptibility results on the 5.0 nm and 5.8 nm

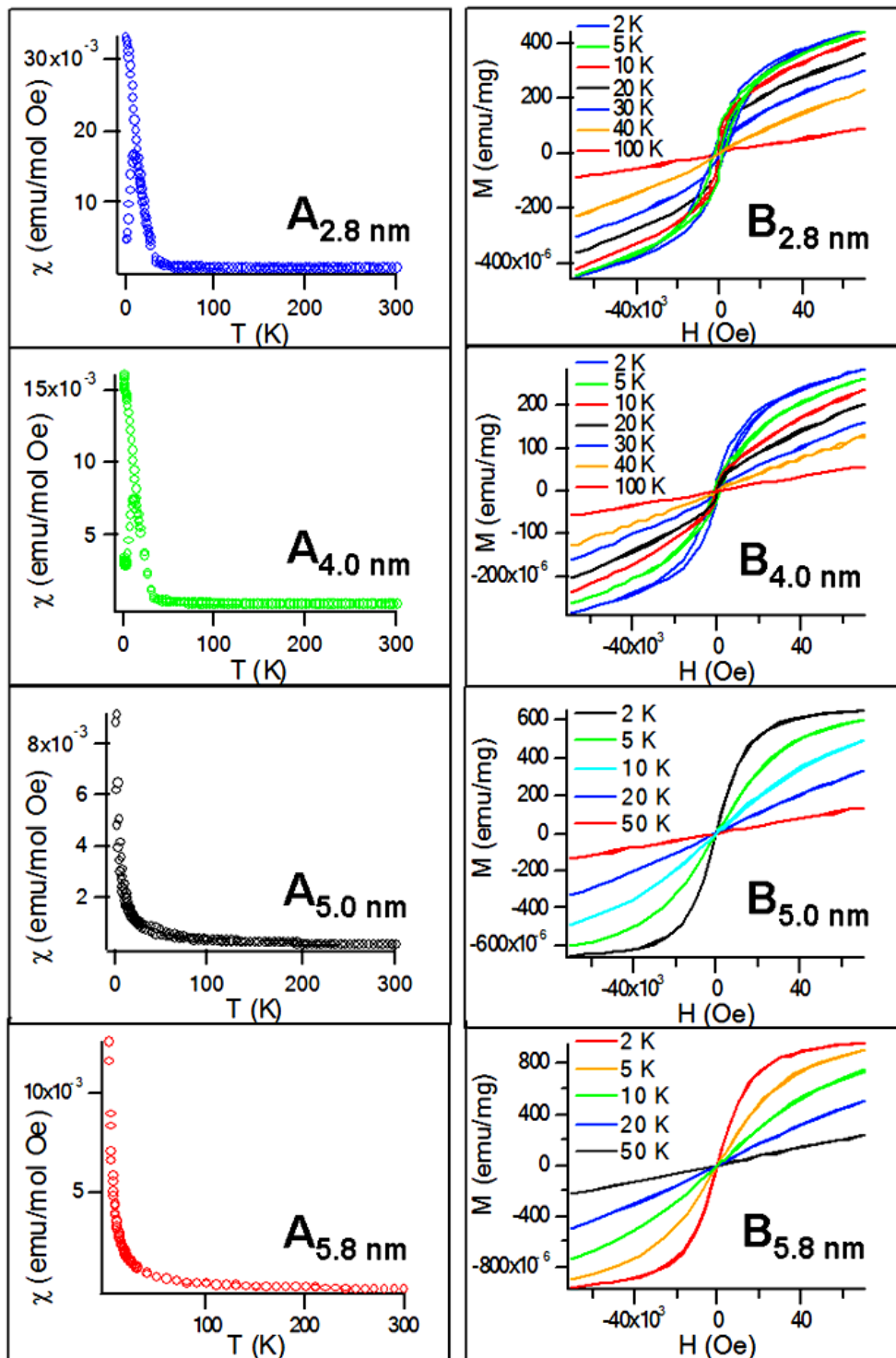


Figure 2.2. A) Temperature dependent ZFC and FC (100 Oe) susceptibility data, and B) Temperature dependent field sweep plots for 2.8 nm, 4.0 nm, 5.0 nm and 5.8 nm 0.6% Mn:CdSe QDs.

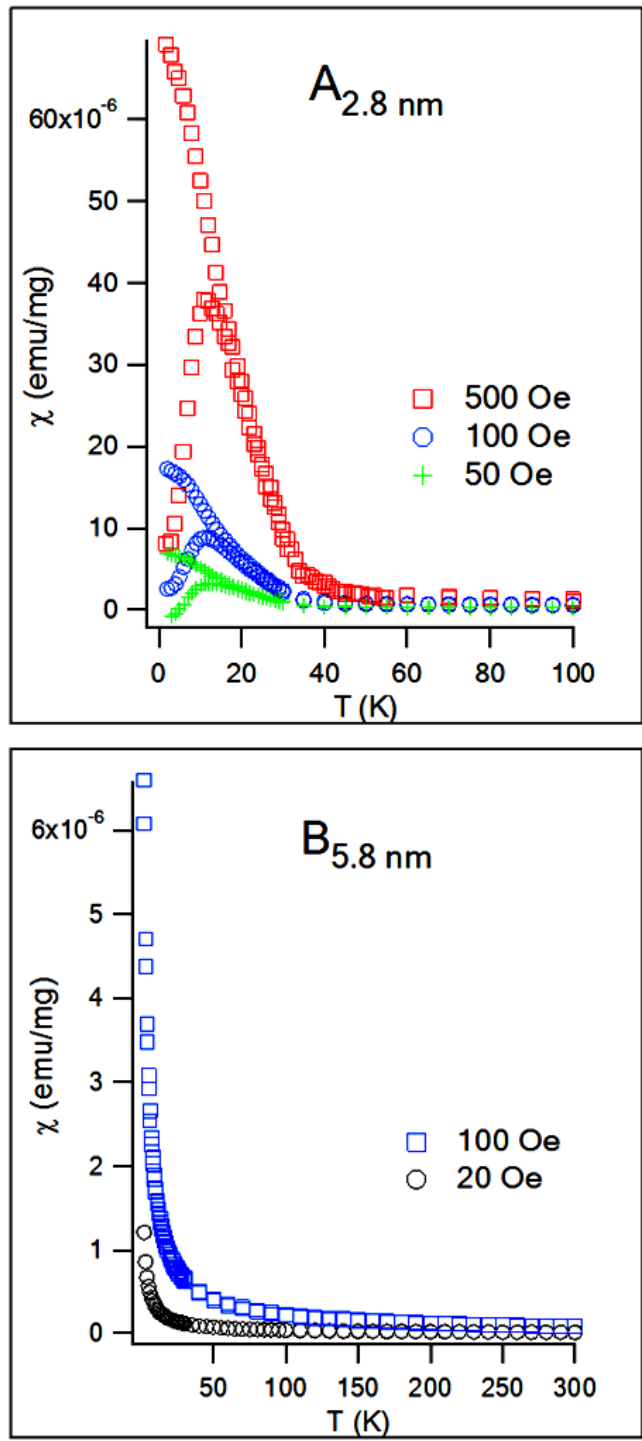


Figure 2.3. ZFC/FC susceptibility at 50 Oe, 100 Oe and 500 Oe for 2.8 nm Mn:CdSe QDs (A) and at 20 Oe and 100 Oe for 5.8 nm Mn:CdSe QDs (B).

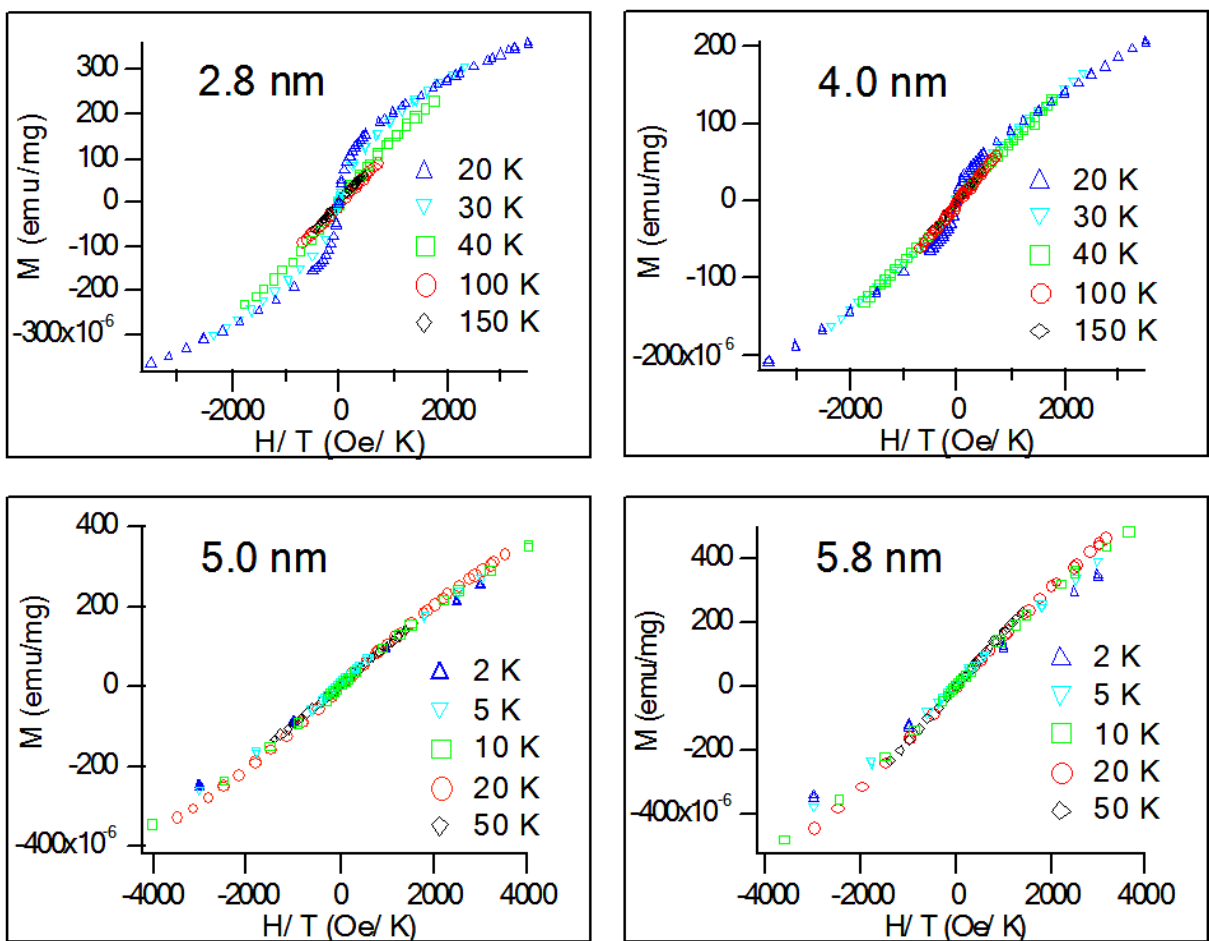


Figure 2.4. Magnetization vs. H/T plots for 2.8 nm, 4.0 nm, 5.0 nm and 5.8 nm Mn:CdSe QDs.

Mn:CdSe are consistent with theoretical predictions and experimental observations in bulk Mn:CdSe samples, where high temperature PM is reported with a weak antiferromagnetic (AFM) exchange at low T arising from the short range exchange coupling between Mn(II) ions (J_{NN} (-7.3) and J_{NNN} (-2.4)).²⁴ The magnetic susceptibility plots for the 2.8 nm and 4.0 nm Mn:CdSe samples are more complex. As observed in Figure 2.4, a change in the magnetization is observed above 20 K when the magnetization data overlaps in the M vs. H/T plots for 2.8 and 4.0 nm QDs. The observed transition behavior is consistent with SPM-like character above a magnetic blocking temperature.¹²

Evidence of SPM behavior rather than spin-glass behavior in the 2.8 nm and 4.0 nm QDs can be further confirmed by measurement of the frequency dependent ac-susceptibility. The phase behavior can be analyzed using the Mydosh criteria $\Phi = \Delta T_f / [T_f \Delta(\log \omega)]$, where T_f is the temperature at which the maximum in $\chi'(T)$ occurs, ΔT_f is the difference in T_f between an initial frequency ω_i and final frequency ω_f , and $\Delta(\log \omega)$ is the difference between the log of the initial and final measuring frequencies.⁵⁷ A value of Φ observed for SPM materials is $\Phi = 10^{-1}$ to 10^{-2} , while a spin glass yields a value of $< 10^{-2}$.⁵⁷ Using the Mydosh parameter SPM character has been assigned to Fe_3O_4 nanocrystals ($\Phi = 0.07$)¹⁵ and an Fe-Ni alloy ($\Phi = 0.1$),⁵⁷ while spin glass behavior is observed for $Zn_{1-x}Mn_xIn_2Te_4$ ($\Phi = 0.005$).⁵⁸ The ac-susceptibility of the 2.8 nm and 4.0 nm Mn:CdSe QDs was measured at 1 Hz, 10 Hz, 100 Hz and 1000 Hz (Figure 2.5). In Figure 2.5, a plot of the real (χ') (Figure 2.5A) and imaginary (χ'') (Figure 2.5B) components reveal a phase lag in the magnetic data which can arise from either superparamagnetic (SPM) or spin-glass (SG) behavior in the QDs. The values of Φ obtained for 2.8 nm and 4.0 nm dots are 0.09 and 0.08, respectively confirm the assignment of SPM behavior in the 2.8 nm and 4.0 nm Mn:CdSe samples.¹⁵ SPM behavior has been observed previously in 4.0 nm Mn(1%):CdSe QDs.³⁷

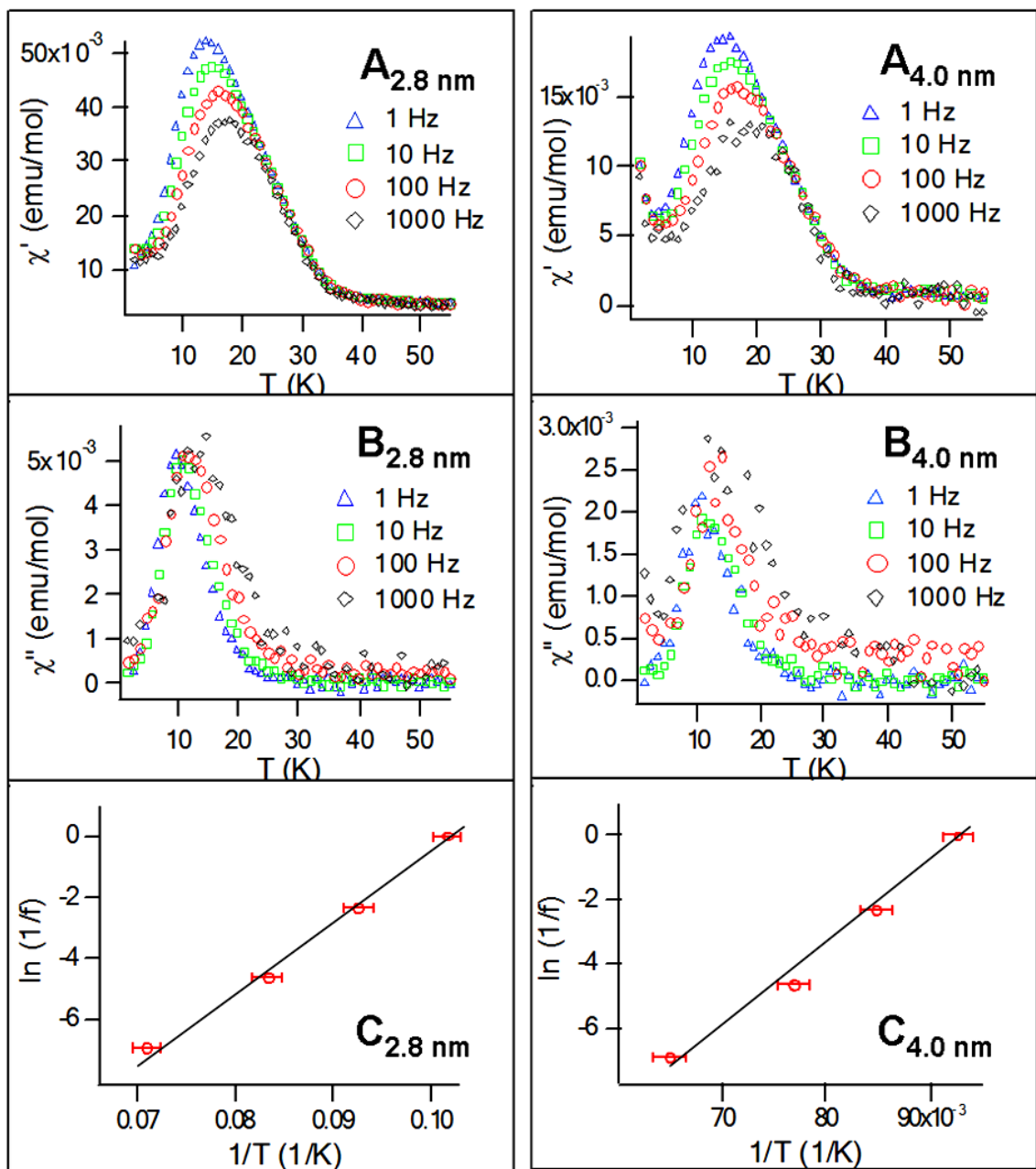


Figure 2.5. Temperature dependent ac-susceptibility (1–1000 Hz) data for the 2.8 nm and 4.0 nm 0.6% Mn:CdSe QDs showing the A) in-phase (real) component $\chi'(T)$, B) out of phase (imaginary) component $\chi''(T)$, and C) temperature dependent Arrhenius plots for the imaginary component $\chi''(T)$.

The energy barrier for spin relaxation can be extracted from the temperature dependent ac-susceptibility curves (Figure 2.5C). Fitting the data to the Arrhenius equation, $\ln(\tau/\tau_0) = E_a/(k_B T)$, where τ is the average relaxation time corresponding to the frequency of the ac measurement and E_a/k_B is the energy barrier to magnetic reversal in an isolated particle, yields a value for the 2.8 nm Mn:CdSe QDs of $\tau_0(2.8 \text{ nm}) = 9.6 * 10^{-11} \text{ s}$ and $E_a/k_B(2.8 \text{ nm}) = 225 \pm 10 \text{ K}$ ($E_a = 4.9 * 10^{-40} \text{ eV}$), and a value for the 4.0 nm Mn:CdSe QDs of $\tau_0(4.0 \text{ nm}) = 6.6 * 10^{-11} \text{ s}$ and $E_a/k_B(4.0 \text{ nm}) = 250 \pm 10 \text{ K}$ ($E_a = 5.5 * 10^{-40} \text{ eV}$). The value of τ_0 for both 2.8 nm and 4.0 nm QDs is in the range observed for SPM materials ($\tau_0 = 10^{-9} - 10^{-11} \text{ s}$).¹⁵

The magnetization data for the 5.0 nm and 5.8 nm Mn:CdSe QDs exhibits the predicted high temperature PM behavior for the low doping levels of Mn(II) in CdSe.²⁴ The observation of SPM-like behavior in the 2.8 nm and 4.0 nm QDs with an observed magnetic phase transition at 12 K coupled to the onset of a magnetic hysteresis is surprising. A plot of the coercivity data vs. temperature in Figure 2.6A illustrates that although the T_B is size independent, the coercivity at 2 K is size dependent for the 4.0 nm and 2.8 nm Mn:CdSe samples. A plot of the coercivity versus size (Figure 2.6A inset) shows a decreasing linear correlation with increasing volume of the QD up to the 5.0 nm sample. The coercivity behavior is inconsistent with Domain theory for SPM materials, since classical SPM behavior would predict an increasing coercivity as the critical domain size is approached. According to the Stoner-Wohlfarth theory, the magnetocrystalline anisotropy E_a of a single domain particle should decrease with decreasing particle size, since $E_a = KV\sin^2\theta$, where K is magnetocrystalline anisotropy constant, V is the volume of the nanoparticle and θ is the angle between the magnetization direction and the easy axis of the nanoparticle.^{4,59} Assuming the value of K and θ are constants, the Stoner-Wohlfarth theory predicts for the Mn:CdSe QDs, a decrease in E_a from 250 K (4.0 nm) to 86 K (2.8 nm) (the E_a for 2.8 nm QD is predicted from theory to decrease by 34.3% of the value for the 4.0 nm QD) in

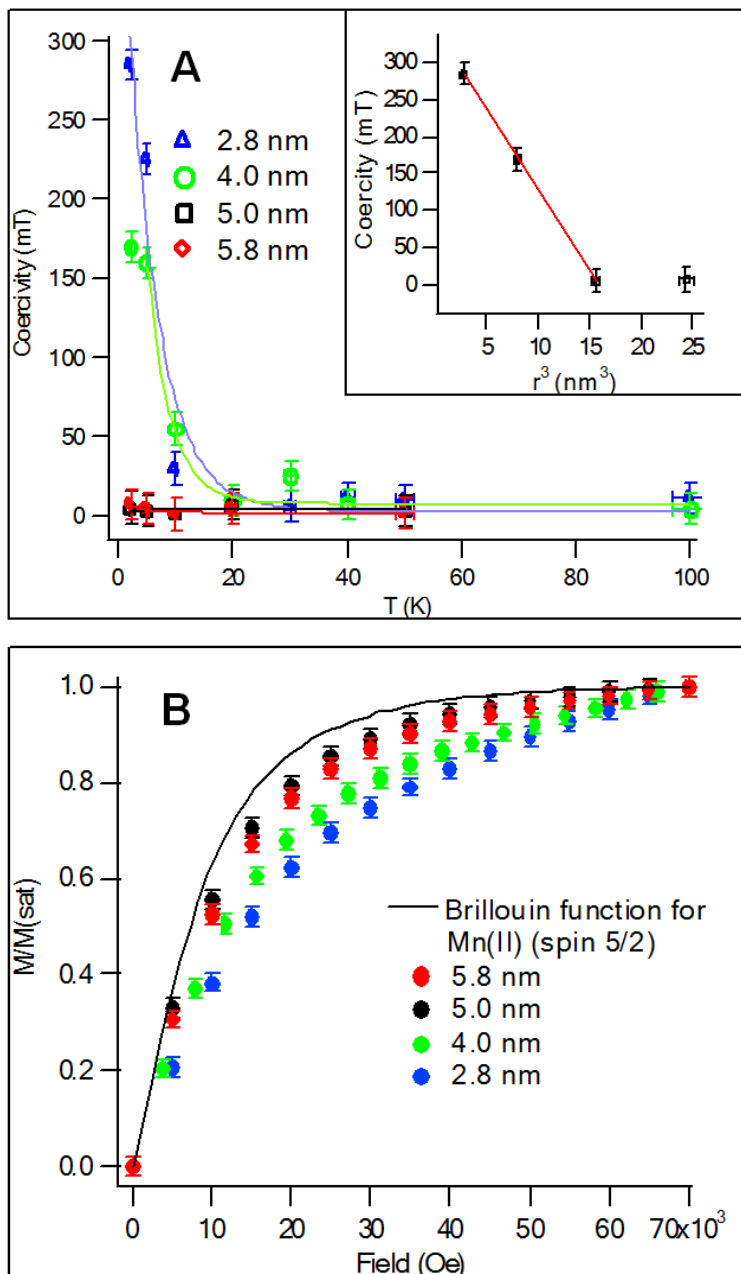


Figure 2.6. Plot of the A) Temperature dependent coercive field (mT) for 2.8 nm, 4.0 nm, 5.0 nm, and 5.8 nm Mn:CdSe QDs. The dependence of the coercive at 2 K vs volume of the QD is plotted in the inset. B) Theoretical Brillouin function assuming $S = 5/2$, $g = 2.0$ compared to the normalized magnetization data.

order to account for the decrease in volume at constant Mn concentration. For the Mn:CdSe samples in the < 4.0 nm size regime, however, the measured values for the energy barrier and relaxation lifetime are size independent within experimental error, which is inconsistent with the magnetization behavior arising from simple Domain theory predictions. The failure to follow simple domain theory predictions may reflect contributions from surface induced carriers, which would increase with decreasing QD size, the inverse of the predicted Domain theory behavior for a SPM system.

2.4 Discussion

The observation of the size dependent magnetic behavior of the Mn:CdSe DMSQD sample is surprising. The exchange interaction in Mn:CdSe in the absence of carriers involves primarily Mn-Mn nearest neighbor exchange interactions, leading to antiferromagnetic (AFM) exchange.²⁴ At a doping level of 0.6% Mn(II) ($x = 0.006$ in $\text{Mn}_x\text{Cd}_{1-x}\text{Se}$) the Mn(II) separation distance should approach a theoretically calculated mean value of 2.1 ± 0.6 nm assuming a Poisson distribution of doping. The large separation distance for Mn(II) centers should lead to PM behavior for all the samples with no observable magnetic transition above 1 K.²⁴ An assumption of the magnetic exchange in the Mn:CdSe DMSQD of a simple Mn(II)-Mn(II) nearest neighbor exchange interaction cannot account for the observation of size-dependent ferromagnetic (FM) exchange in the Mn:CdSe QDs in this study.

Ferromagnetic exchange can arise from formation of spin clusters at high doping levels, as previously reported,³⁷ however at 0.6% doping levels within a 2.8 nm Mn:CdSe QD, only *two* Mn(II) ions would be present and a calculation of spin-cluster formation at $< 1\%$ suggests the magnetic behavior cannot be easily attributed to spin-cluster formation in this doping and size regime. An alternative possibility is the presence of intrinsic carriers in the Mn:CdSe DMSQD

arising from the non-stoichiometric Cd to Se ratios¹⁹ or the presence of ligand induced states at the QD surface.^{32,41} The presence of weakly localized or delocalized carriers can result in the observation of magnetic exchange via a carrier mediated process in PbSnMnTe,⁶⁰ where intrinsic carriers arise from non-stoichiometric Te content. The carrier mediated RKKY process in PbSnMnTe leads to FM exchange over a narrow carrier density range, with PM behavior for $p < 3 * 10^{20} \text{ cm}^{-3}$ and FM behavior reported for $p > 3 * 10^{20} \text{ cm}^{-3}$.⁶⁰ Although carriers have not been invoked to describe magnetic exchange in Mn:CdSe QDs previously, in undoped CdSe QDs generation of intrinsic carriers has been reported to arise from surface states.^{15,16} The presence of hole carriers in CdSe QDs may explain the various reports of magnetic behavior in magnetically doped CdSe QDs where ferromagnetic, spin-glass, and paramagnetic have been reported depending on the doping level and QD size.^{30,37}

For surface induced carriers, an increase in carrier density is anticipated to follow the surface to volume ratio for the QD, which changes dramatically below 4 nm in diameter.^{60,61} The size dependent carrier density in the Mn:CdSe QD samples in this study can be analyzed by fitting the normalized magnetization plots for the various QD sizes in order to extract the concentration of the temperature dependent and temperature independent spins (Figure 2.6B and Figure 2.7). The spin density is analyzed by fitting the field dependent SQUID data to a Brillouin function (eq 1a) in order to estimate the spin moment per Mn ion, where the Brillouin function (eq 2.1b) can be written as

$$M = Ng\mu_B JB_j(\eta) \quad (2.1a)$$

$$B_j(\eta) = \frac{2J+1}{2J} \coth\left(\frac{2J+1}{2J}\eta\right) - \frac{1}{2J} \coth\left(\frac{1}{2J}\eta\right) \quad (2.1b)$$

$$\eta = \frac{g\mu_B H}{k_B T} \quad (2.1c)$$

where N is the molar volume, μ_B is the Bohr magneton, g is the free electron Landé g -value, and J is the spin. To fit the magnetization, the Brillouin function is used with η (eq 2.1c) being equal to the ratio between the spin components and the thermal energy, where H is the applied magnetic field and k_B is Boltzmann's constant. Equation 2.1a is fit by allowing the values for J to float with $g = 2.0$. The results reveal the magnetization behavior is size dependent with the 2.8 nm QD showing slower saturation than predicted for a theoretical fit to a $S = 5/2$ ($J = S$, since $L = 0$ for Mn(II) ion), $g = 2.0$ system. The lower slope for the Brillouin function indicates a lowering of the total spin moment in the QD sample than theoretically predicted for a Mn(II) center. As the QD size increases (5.0 nm and 5.8 nm), the saturation behavior approaches the theoretical plot indicating the observed spin moment is consistent with the theoretical prediction for Mn(II) centers within the QD.

In Figure 2.7, the temperature dependent fit of the Brillouin function for the 2.8 nm (2 K, 40 K and 100 K), 4.0 nm (2 K, 40 K and 100 K), 5.0 nm (2 K and 50 K) and 5.8 nm (2 K and 50 K) Mn: CdSe QD is shown. The Brillouin fit of the 2.8 nm and 4.0 nm Mn: CdSe QD at 2 K does not follow the theoretically predicted behavior (shape and total spin magnetic momentum) for a $S = 5/2$ Mn(II) dopant (2.8 nm ($S = 1.4$), 4.0 nm ($S = 1.0$)) for the doping levels measured by XRF. At 100 K the 2.8 nm QD can be fit to $S = 2.5$ as theoretically predicted for the Mn(II) ion, while the 4.0 nm is fit to $S = 2.2$. The lower value for S than theoretically predicted in the 4.0 nm data at 100 K is believed to reflect experimental error due to a small sample size for the SQUID measurements leading to the necessity of a large diamagnetic correction to the original SQUID data for this sample. The Brillouin analysis of the 5.0 and 5.8 nm QD shows the magnetization behavior is close to the theoretical value of $S = 5/2$ for both samples at 2 K and 50 K. The fits

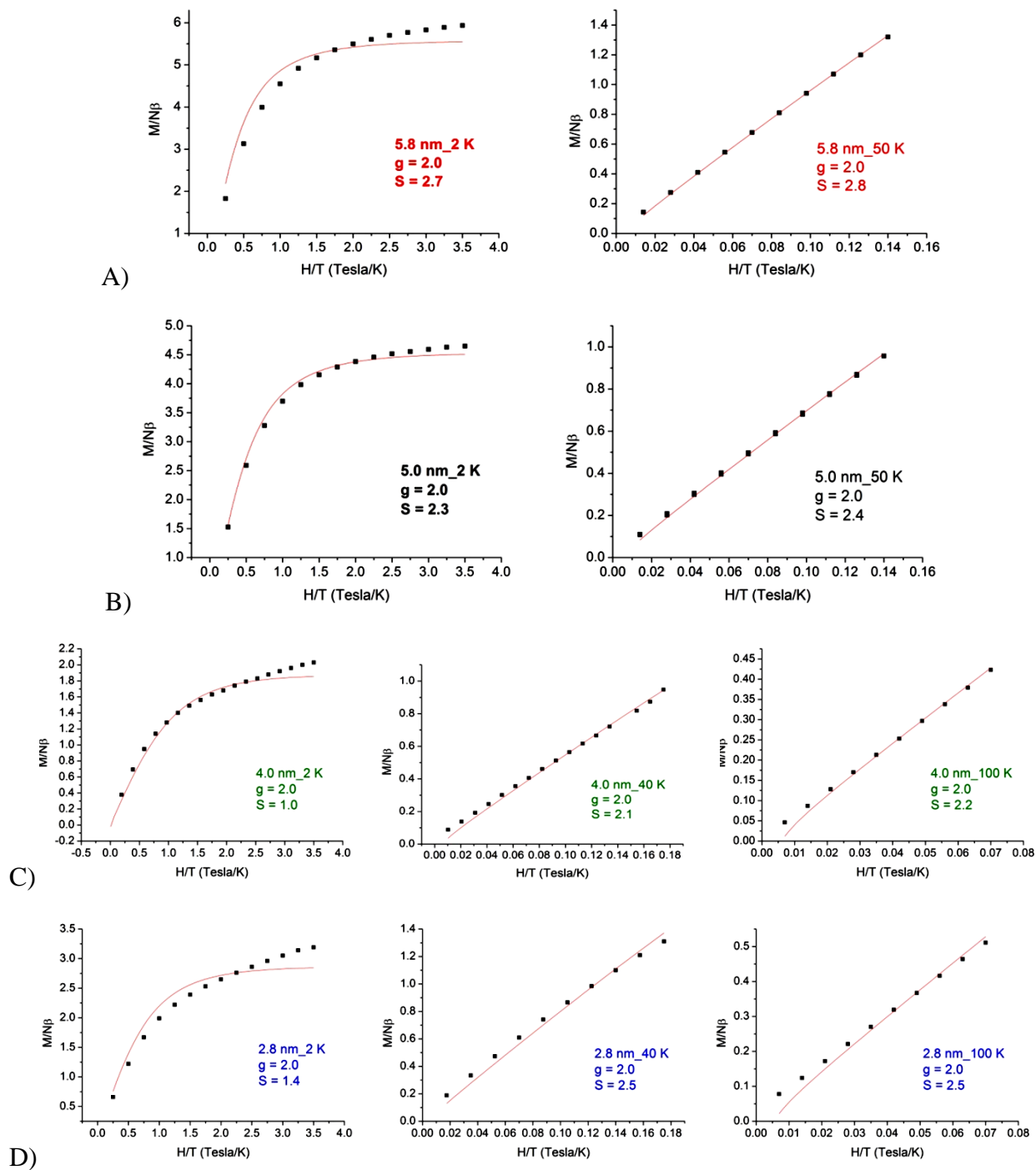


Figure 2.7. Brillouin function fitting of A) 5.8 nm (2 K and 50 K), B) 5.0 nm (2 K and 50 K), C) 4.0 nm (2 K, 40 K, and 100 K), and D) 2.8 nm (2 K, 40 K, and 100 K) Mn: CdSe QDs.

indicate the Mn(II) centers conserve their spin magnetic momentum of 5 Bohr magneton for the large QDs (2 K and 50 K) and for the small QDs at >40 K, but exhibit low spin magnetic moment and a poor Brillouin fit at 2 K for the small QDs (2.8 nm and 4.0 nm QDs). A decrease in the value of spin magnetic moment with decreasing volume but increasing magnetic exchange interactions (coercivity) supports the assumption of potential surface induced contributions to the total magnetization behavior in these materials, where carriers AFM couple to the Mn(II) spins in the lattice at low-T for the small QDs.

In Figure 2.8A, a Currie-Weiss (C-W) law susceptibility plot of the temperature dependent SQUID data, $1/\chi = (T - \theta) * C^{-1}$ (C is the Currie constant, T is temperature in Kelvin, and θ is the Curie temperature) deviates from classical Currie-Weiss behavior for all sizes of Mn:CdSe, exhibiting a temperature dependent paramagnetic and a temperature independent Pauli-paramagnetic contribution to the susceptibility data. Since the temperature independent term is size dependent with a decreasing contribution to the magnetization data with increasing QD size, the data for the 2.8 nm and 4.0 nm cannot be fit to C-W behavior. A fit of the data for the 5.0 and 5.8 nm Mn:CdSe reveal high temperature PM behavior where a negative Currie temperature indicative of AFM exchange with a θ of -4.7 K (5.8 nm) and -11.8 K (5.0 nm). The negative Curie temperature (θ) indicative of AFM exchange interactions in the lattice. The negative deviation for the low-T susceptibility data in Figure 2.8A can be interpreted in term of a ferrimagnetic phase behavior in the Mn:CdSe DMSQDs.¹

Extraction of the temperature independent Pauli-paramagnetic (PPM) component from the susceptibility data in Figure 2.2 can be achieved using a modified Curie-Weiss plot (Figure 2.8B), since $\chi_{\text{exptl}}T = C + \chi_{\text{PPM}}T$. In Figure 2.8B, the PPM contribution is extracted from the slope of the plot at high temperature, while the Currie constant can be extracted from the y-intercept. The measured Curie constants for the samples are $4.3 \text{ emu}\cdot\text{K}/(\text{mol}\cdot\text{Oe})$ (5.8 nm), 2.8

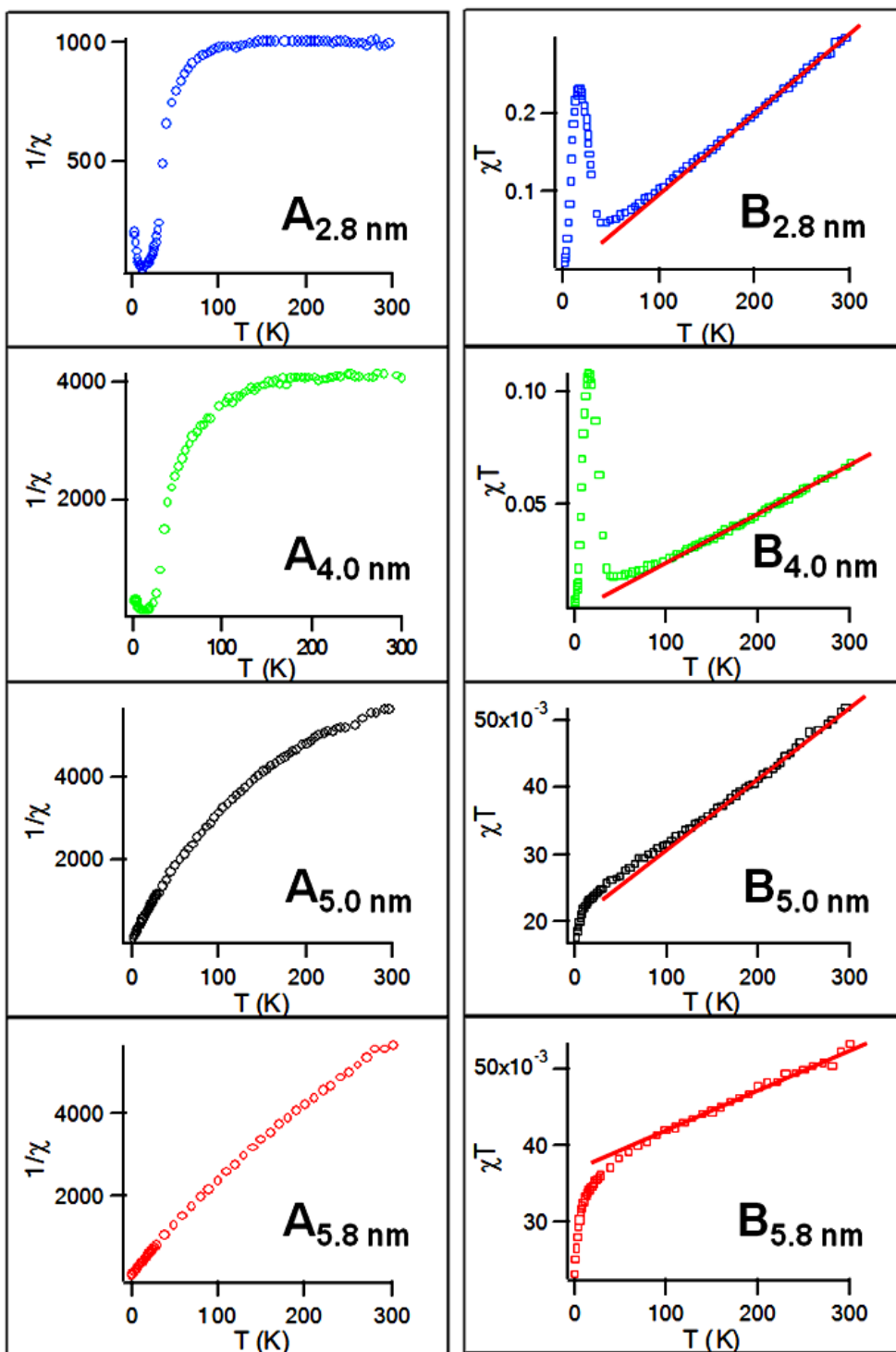


Figure 2.8. Size Dependent A) Curie-Weiss law and B) χT vs. T plots for Mn:CdSe QDs.

emu•K/(mol•Oe) (5.0 nm), 0.9 emu•K/(mol•Oe) (4.0 nm), and 0.6 emu•K/(mol•Oe) (2.8 nm) which does not agree with the theoretical value of 4.4 (emu•K/mol) for $S = 5/2$ except for the largest QD. The Curie constant (C) is reported in terms of the emu per mole of Mn(II) ion in the sample from the χ_{exptl} data.

The strongest PPM contribution to the susceptibility data is observed for the 2.8 nm QD, with decreasing PPM contributions as the QD increases in size. Assuming the susceptibility for the PPM arises only from intrinsic carriers, the PPM susceptibility can be related to the concentration of carriers within the QD implying as the QD decreases in size the carrier concentration per unit volume increases. In Figure 2.9, a plot of the carrier concentration versus inverse QD diameter shows an exponential dependence on the PPM concentration with size. The inverse dependence on diameter in Figure 2.6 suggests the decrease in carrier density reflects the surface to volume ratio for the QD, as suggested in earlier SQUID and XMCD measurements.^{32,41} Although the experimental observation is consistent with carrier density measured for CdSe QDs and the reported increase in carrier concentration in CdSe with decreased QD size, it can not distinguish between donor levels generated by the ligand, the Cd to Se ratio, or a combination of the two.^{19,32,41}

2.5 Conclusion

The $1/d$ dependence of the PPM contributions to the susceptibility data supports the presence of intrinsic carriers in the Mn:CdSe QDs, that are likely associated with surface states. The presence of carriers generates electron density at the Fermi level, as suggested in earlier studies on CdSe QDs,^{32,41} which leads to indirect carrier mediated RKKY interaction as described in Figure 2.10. Increasing carrier densities with decreasing QD size leads to the onset of SPM DMSQD exhibiting a magnetic transition at 12 K for the 2.8 nm and 4.0 nm QDs. The

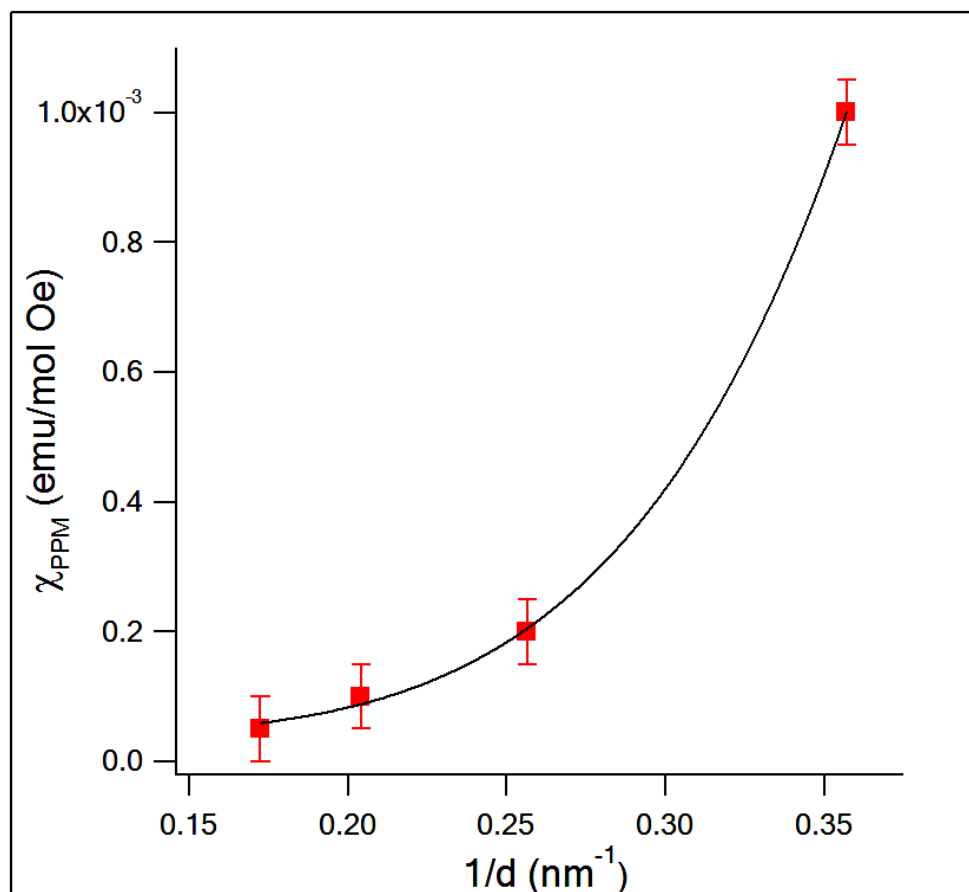


Figure 2.9. The size dependent magnetic susceptibility arising from the temperature independent Pauli paramagnetic contribution to the total susceptibility.

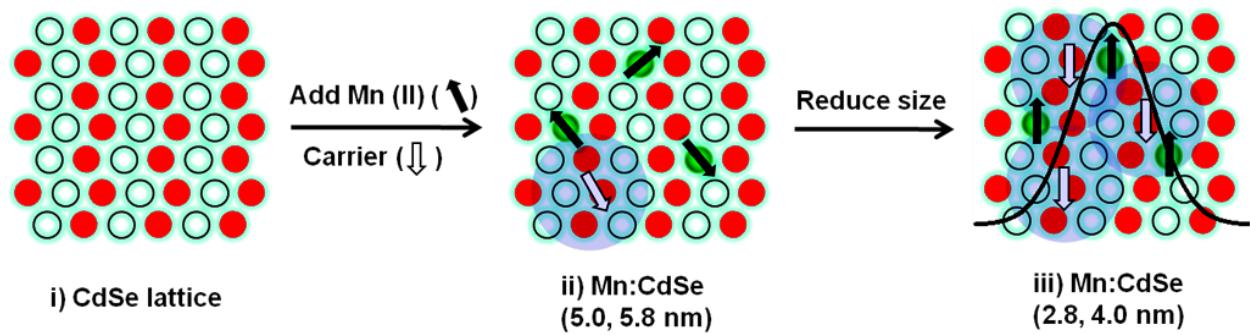


Figure 2.10. Proposed model of the onset of magnetic exchange in Mn: CdSe QDs governed by long-range carrier mediated RKKY processes.

onset of magnetization below 4.0 nm where the susceptibility data exhibits blocking behavior reflects the critical threshold for the carrier density to induce the exchange interactions within a SPM-like single domain (Figure 2.10). The magnetization study for Mn: CdSe QD suggests with an increase in size the reduction in surface to volume ratio lowers the carrier density below the critical threshold due to the decrease in ligand induced surface states per QD volume. The larger QDs exhibit paramagnetic behavior when the carrier density is below the percolation threshold in the 5.0 and 5.8 nm Mn: CdSe DMSQDs.

The surface induced carriers, which are believed to arise from charge transfer effects associated with the ligation layer, must be weakly localized in order to result in the long-range RKKY exchange coupling. The long-distance carrier mediated exchange coupling attributed to AFM exchange between Mn(II) spins and weakly bound carriers, as proposed by MacDonald, et al,⁶¹ generates ferrimagnetic phase behavior in the QDs below 4.0 nm in diameter. The participation of carrier mediated exchange would explain the decreased magnetic saturation value observed for the smallest QDs (Figure 2.2). Similar behavior has been reported for ligand induced carrier mediated exchange in Mn(II) doped ZnO QDs³³ and in semi-magnetic II-VI bulk semiconductors.^{27,60,62} Further studies investigating the ligand dependent influence on the magnetic susceptibility is underway to deduce the importance of ligand passivation on the observed magnetic properties.

CHAPTER THREE

PROBING THE LOCAL SITE ENVIRONMENTS IN Mn:CdSe QUANTUM DOTS

A quantum dot (QD) contains a well-defined surface passivated by ligands and a bulk-like core. Surface passivation and lattice truncation leads to local structural and electronic micro-environments within the QD. Probing the local micro-environments that exist at the surface or core of the QD is difficult but can be achieved by use of a Mn(II) impurity ion doped into a CdSe QD using electron paramagnetic resonance (EPR). Using high frequency EPR (HF-EPR) spectroscopy, the site dependent perturbation experienced for Mn(II) incorporated as a guest ion into CdSe QDs allows the distinguishing of two unique micro-environments within the QD, namely an unperturbed core and an electronically distorted surface. Analysis of the Landé g -factor, hyperfine constant (A), and the distribution of g and D (Δg , ΔD) allows the local microenvironments within CdSe to be probed as a function of size, ligand passivation, and site of Mn(II) incorporation.

3.1 Introduction

The physical properties of a quantum dot (QD) are strongly influenced by local structural and electronic perturbations that are produced in response to the ligation of the dangling bonds at the QD surface to minimize surface energy.^{17,18,22,51,63-65} In the simplest perspective, a CdSe QD is composed of several Cd-Se layers, which are defined by the lattice planes, and are unique from the macroscopic single crystal counterpart in that a QD possesses a high surface to volume ratio which is passivated through a metal-ligand interaction. A CdSe QD that is 2 nm in diameter

consists of a volume containing ~six lattice planes, wherein the surface passivated layer accounts for 48% of the atoms. At 5 nm, the CdSe QD consists of ~14 planes and a surface to volume ratio of 21%. Passivation of the surface leads to differences in the micro-environments of atoms that are passivated relative to the core of the QD. Earlier studies on the QDs have revealed size dependent changes to the lattice occur that are dissipated over several lattice planes reflecting the passivant effects on the quantum dot.^{63,66,67} While it is accepted surface passivation will impact the properties of the QDs;^{65,68,69} recent studies have shown that the nature of the passivant can perturb the growth behavior of the quantum dots,⁷⁰ influence the observed optical properties,^{19,71-74} and even result in the observation of paramagnetism due to charge transfer contributions in CdSe QDs.^{32,41} Understanding the size and ligand dependent changes in the local micro-environments of an organically passivated QD is critical for application of these materials.

In CdSe QDs, there are many approaches to probing the surface relative to the core of a QD, namely ligand dependent changes in the optical properties,⁷⁵ Raman spectroscopy,⁷⁶ magnetism,^{32,33,77} x-ray absorption,^{24,32} and NMR.^{51,78-80} Insight into the changes within a QD arising from surface passivation can be analyzed by intentionally incorporating a spectator ion into the lattice capable of reporting on the local electronic and structural micro-environments experienced at the surface and in the core of the QD. Electron paramagnetic resonance (EPR) spectroscopy is very effective at probing subtle changes in the crystal field around the paramagnetic guest ion.³⁵ In EPR, theoretical calculations have shown the g-value responds to changes in the crystal field and charge transfer properties of the lattice,⁴³ while the hyperfine constant (A) is sensitive to site symmetry and changes in the electronic structure around the paramagnetic ion of interest. Probing the crystal field and structural local environment surrounding a guest ion, such as Mn(II) which is an isoelectronic dopant in II-VI semiconductors, through EPR can allow the site dependent electronic micro-environments within CdSe QDs to be

analyzed. The doping of Mn(II) into CdSe QDs, which is well described by a substitutional occupation of the Cd(II) site by the Mn(II) guest ion,^{29,37} is an ideal probe of the micro-environments within the II-VI lattice since the II-VI lattice is diamagnetic and EPR silent while the paramagnetic Mn(II) ion is sensitive to changes in crystal field and orbital admixture.⁴⁴

In this manuscript, the size (1.3, 2.8, 5.0, and 5.8 nm) and ligand (dodecanitrile (DDN), dodecylamine (DDA), pyridine (py), tri-n-octylphosphine (TOP), and TOP-Se dependent perturbation of the electronic micro-environments within a Mn(II) doped CdSe QD is probed using high frequency EPR (HF-EPR) measurements at 406.4 GHz on 0.6% Mn:CdSe. The changes in the Mn(II) HF-EPR parameters (g-tensor, Hyperfine constant (A), Zero-field splitting anisotropy term (D), and linewidth (ΔH) allow interpretation of the changed in crystal field and charge transfer properties for the surface and core sites to be spectrally probed. Although low frequency EPR has been carried out on QDs, the use of HF-EPR allows for the first time the spectral resolution⁴⁸ of the individual surface and core components in the EPR and therefore in-depth insight into the effects of size and passivation. Discrete surface and core sites within the QD are assigned by HF-EPR demonstrating the effect of surface passivation by an organic ligand strongly perturbs the surface layer but exhibits no impact on the core of the QD. The surface hyperfine constant tracks the crystal-field strength of the passivant. The size dependence of the EPR properties suggest the QD core is bulk like for QDs larger than 2 nm, but dominated by the surface passivated layer for QDs less than 2 nm. The population ratio of the surface and core Mn(II) sites scales linearly with the QD surface to volume ratio, as expected for a Poissonian distribution for Mn(II) doped CdSe QDs. Chemical etching experiments confirm the surface Mn(II) sites reflect bound Mn(II) centers and not adventitious Mn(II) ions in the passivant layer.

3.2 Experimental

Chemicals. Dodecylamine (DDA) (98+%, Alfa Aesar), MnBr_2 (anhydrous, 99%, Alfa Aesar), cadmium stearate (CdSA, 90%, Strem Chemicals), selenium powder (99.99%, Strem Chemicals), tri-n-octylphosphine (TOP, 90%, Alfa Aesar), decane (99%, Acros Organics), dodecanonitrile (DDN, 98%, Alfa Aesar) toluene (>99.9%, EMD Chemicals) and methanol (MeOH, >99.8%, VWR) were used as supplied. $\text{Li}_4[\text{Cd}_{10}\text{Se}_4(\text{SeC}_6\text{H}_5)_{16}]$ (Cd_{10}) and TOP-Se stock solution was prepared as described previously.^{51,81}

Preparation of stochastically doped DDA- $\text{Mn}_x\text{Cd}_{1-x}\text{Se}$ ($x = 0.006$). The series of Mn:CdSe (1.3, 2.8, 5.0, and 5.8 nm) with a 5–6% size distribution was prepared by reaction of $\text{Li}_4[\text{Cd}_{10}\text{Se}_4(\text{SeC}_6\text{H}_5)_{16}]$ (Cd_{10}) and MnBr_2 in dodecylamine (DDA) as reported previously.⁷⁷ Briefly, the QDs are prepared by the dissolution of 200 mg (0.05 mmol) of Cd_{10} in ~20 mL of DDA at 100 °C under N_2 . To the solution, 4.34 mg (0.02 mmol) MnBr_2 is added and the reaction allowed to stir for 1h to induce ion exchange into the Cd_{10} cluster. The reaction mixture was heated to 220 °C (10 °C/min) inducing QD growth. The solution was cooled to room temperature, dissolved into toluene, precipitated by the addition of MeOH, and centrifuged to isolate the QDs (4×). The QDs were dissolved in a minimum of pyridine, precipitated (3×) by the addition of hexane to remove Mn(II) impurities, and isolated by centrifugation. Sequential dissolution/re-precipitation steps has been shown to effectively remove unreacted Mn(II).^{36,37} The samples were analyzed by UV-vis spectroscopy, transmission electron microscopy (TEM), and powder X-ray diffraction (pXRD) to verify size, shape, dispersity, and structure. The Mn(II) concentration was analyzed by XRF and verified by fitting of the SQUID data to a Brillouin function.

Passivant Exchange. The surface passivant on the 5.0 nm Mn:CdSe sample was exchanged for DDN (dodecanonitrile), TOP (tri-n-octylphosphine), TOP-Se (tri-n-

octylphosphine selenide), DDA (n-dodecylamine), and py (pyridine) following ligand exchange procedures in the literature.^{32,82} Briefly, excess passivant of interest was added to a saturated QD solution in toluene, the mixture sonicated for ~3 hrs at 60 °C, and precipitated by the addition of MeOH. The samples were dissolved in toluene and re-precipitated three times to ensure excess ligand removal.

Preparation of Surface Doped Mn_xCd_{1-x}Se (x = 0.004). Surface doped Mn:CdSe was prepared using a microwave synthetic approach in a single mode CEM Discover System operating at 300 W, 2.45 GHz. For the Mn(II) surface doped CdSe QD reaction, 135.9 mg (0.2 mmol) of CdSA in 4 mL of decane, 1.0 mL (1.0 mmol) of a 1 M TOP-Se stock solution and 4.3 mg (0.02 mmol) MnBr₂ was added in a static 10 mL reaction vessel (5 mL reaction volume). The reaction was carried out for 30 s in the microwave cavity using 300 W, 300 psi and a reaction temperature of 220 °C. The Mn:CdSe surface doped sample is isolated as described previously⁸¹ and analyzed analogous to the method above.

Acid Etching of Mn:CdSe QDs. Surface etching to remove the outermost 1–3 layers of the Mn:CdSe QD samples was carried out using 20 µL H₃PO₄:HCl (1:1 V:V)⁸³ in 1 mL saturated DDA/toluene. The QD samples were etched for 2 seconds at room temperature. The shift in the exciton absorption value for the first exciton was used as an approximate measure of the number of outer shells removed by the etching step. The etched samples were precipitated by the addition of MeOH, re-dissolved in toluene and re-precipitated by MeOH addition prior to EPR experiments.

Quantum Dot Characterization. Spherical, wurtzite stochastically doped Mn_{0.006}Cd_{0.994}Se QDs were isolated from solution with a 5–6% size dispersity on average. The prepared QD samples were analyzed for total Mn, Cd and Se concentration by X-ray fluorescence analysis using the Cu K_α line for analysis of Mn(5.9 KeV), Cd(23.1 keV) and

Se(11.2 keV). The metal (Cd + Mn) to Se ratio is ~0.9 to 1, which is in agreement with the metal to chalcogenide ratio in pure CdSe QDs of 0.9:1. Since incorporation of Mn(II) should lead to ion vacancies,^{52,84} the XRF results confirm the Mn(II) assignment in which the Mn ion is incorporated as a substitutional element at a Cd T_d site rather than interstitial incorporation. The QD size and dispersity was analyzed by TEM for QDs dispersed on holey carbon (400 mesh) from a toluene solution using a JEOL-2010 microscope operated at 200 kV. The TEM measurements confirm the optical sizing of the QD using absorption spectroscopy.⁵³ pXRD measurements confirm the structural assignment of wurtzite. Mn₃O₄ was not observed as an impurity in the samples based on analysis of the powder XRD pattern or vibrational analysis of the powdered sample using FT-IR.^{85,86} Complete absorption data for all four samples (1.3, 2.8, 5.0 and 5.8 nm) and representative TEM, pXRD, and FT-IR data for the 5.0 nm Mn:CdSe sample are provided in Figure 3.1. pXRD and TEM spectra for the 2.8 and 5.8 nm Mn:CdSe samples were previously reported.⁷⁷

X-ray Absorption Spectroscopy. Soft x-ray absorption near edge spectroscopy (XANES) to assess the Mn oxidation state was performed at the National Synchrotron Lightsource, Brookhaven National Laboratory, on beamline U4B. QD powders were affixed to carbon tape, mounted on a stainless steel paddle, and inserted into an ultra-high vacuum (UHV) chamber. XANES experiments were conducted using the total electron yield detection method where the total photocurrent is measured as the photon energy is scanned through the absorption edges. All spectra are normalized to the photocurrent from a gold grid placed upstream from the sample UHV chamber. The experimental energy resolution was ~0.10-0.20 eV for Mn L_{3,2}.

EPR Measurements. The Q-band EPR (34 GHz) spectra were recorded on a Bruker Elexsys-500 spectrometer. High frequency EPR measurements at room temperatures were performed at the National High Magnetic Field Laboratory (NHMFL), Tallahassee, FL. The

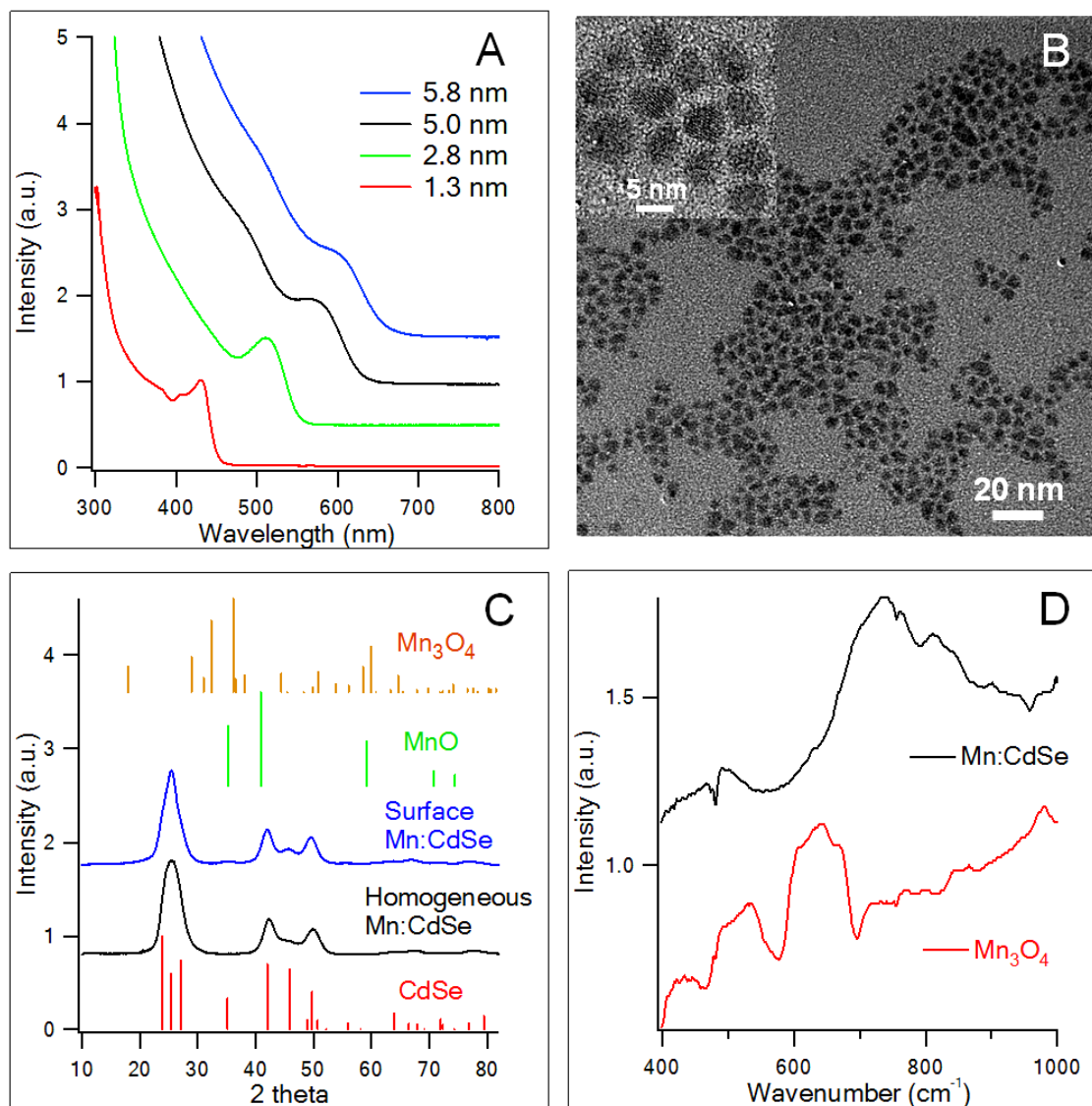


Figure 3.1. Characterization data for 5.0 ± 0.3 nm 0.6% homogeneously doped Mn: CdSe QDs. A) Absorption spectra in toluene (spectra for other sizes are included), B) TEM image (HR-TEM inserted), C) pXRD pattern (surface doped Mn: CdSe included), and D) FT-IR spectra. In Figure S1D, the lack of FT-IR absorptions for Mn–O at 411 , 524 , and 630 cm^{-1} is suggestive that the presence of Mn(III) impurities are well below the detectable limit for the experiment ($<0.01\%$).

setup operates in transmission mode and employs oversized cylindrical waveguides.^{42,87} Microwave detection was performed with a low-noise, fast-response InSb hot-electron bolometer (QMC Ltd.). Microwave frequencies in the range of 216–406.4 GHz were chosen for our experiments to allow for optimal spectral dispersion and frequency resolution. For the EPR experiments, all samples were analyzed as powder. The microwave frequency was measured with a built-in digital counter and the magnetic field was calibrated using 2,2-diphenyl-1-picrylhydrazyl (DPPH, $g = 2.0037$). Modulation amplitude and microwave power were optimized for high signal-to-noise ratio and narrow peaks.

2.3 Results and discussion

A Mn(II) guest ion can be substituted as an iso-electronic ion onto the metal Cd(II) ion sites within CdSe QDs. It has been observed that Mn(II) ion incorporation is achievable to high doping levels (50%) without spinodal decomposition and no significant perturbation to the average lattice parameters are observed at doping levels of $< 1\%$.^{24,88} The Mn(II) distribution is expected to be Poissonian exhibiting a statistical distribution between the core and QD surface (Figure 3.2A).⁷⁷ At a doping level of 0.6%, the number of Mn(II) ions on average that are present in the Mn:CdSe QD are *~one* (1.3 nm), *~two* (2.8 nm), *~seven* (5.0 nm), and *~ten* (5.8 nm). At 1.3 nm in diameter, the QD is comprised of just *four* lattice planes, which results in the Mn(II) site being statistically at the QD surface and therefore passivated by a ligand. At 5.8 nm diameter, the QD is composed of ~ 16 lattice planes with a ratio of surface to volume of 18%, resulting in the Mn(II) occupying predominately core sites in the QD if doping is statistical, as reported earlier.⁷⁷ For comparison to the statistically doped Mn:CdSe sample, a surface *only* doped 5.5 nm QD doped at 0.4% (as used in this study) will contain *~six* Mn(II) ions incorporated at the

passivation layer. The QDs used in this study have been previously reported⁷⁷ and therefore only selected characterization data is provided in Figure 3.2.

EPR Parameters for Mn:CdSe. As a dopant ion in the naturally anisotropic wurtzite lattice of CdSe QDs, the Mn(II) ion will exhibit a sextet hyperfine splitting pattern arising from the $S = 5/2$, $I = 5/2$, $L = 0$ ground state (6A_1) (Figure 3.2B). Earlier EPR studies on single crystal Mn:CdSe, showed the natural anisotropy within a wurtzite Mn:CdSe, requires the use of higher order terms for the spin Hamiltonian to account for axial (D ($\sim 10^{-3}$ cm $^{-1}$), F ($\sim 10^{-4}$ cm $^{-1}$)) distortion.⁴⁵ Although not absolutely correct, the broader linewidths observed in QD powdered samples coupled to the small value for D and F do not allow the full spin Hamiltonian to be accurately analyzed and therefore the EPR pattern for Mn:CdSe QDs is typically fit to a simplified spin Hamiltonian showing only the second-order axial term (D -term) (eqn. 3.1).^{89,90}

$$\hat{H} = \sum_{n=1}^n \{g\beta H \cdot S + AS \cdot I + D[S_z^2 - \frac{1}{3}S(S+1)]\} \quad (3.1)$$

where H is the Zeeman field, g is the Landé g -factor, β is the Bohr magneton, A is hyperfine constant, S and I are the electron and nuclear spin operators, and D is the axial zero-field splitting. The Hamiltonian in eqn (1) leads to the observation of five EPR transitions between electron spin quantum number ($M_s = \pm 5/2$) each split into six components by the hyperfine coupling to the $5/2$ nuclear spin of ${}^{55}\text{Mn}$ (Figure 3.2B). The hyperfine split terms will overlap at small values of D leading to the simplified EPR pattern typically observed in Mn(II) compounds.

The splitting pattern will be further impacted by the surface and core for a QD and the distribution in QD size, shape, and doping concentration. In a Mn:CdSe QD small changes in the crystal field around the Mn(II) centers will lead to small variation of the EPR parameters, as suggested in Mn(II) doped CdSe/ZnS core shell QDs.⁶⁷ In a QD, the spin Hamiltonian in eqn (3.1)

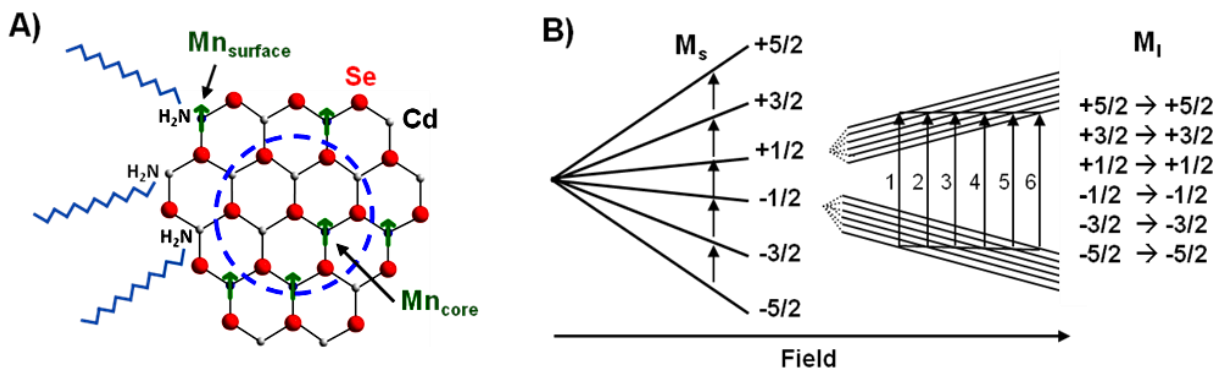


Figure 3.2. A) Schematic representation of a QD depicting the surface and core doping sites for a 2 nm Mn: CdSe QD showing the core and surface site for Mn(II). B) EPR splitting pattern for a Mn(II) ion ($S = 5/2$, $I = 5/2$ and $L = 0$) occupying a pseudo- T_d site in CdSe showing only first-order perturbation. The transition fields of hyperfine splitting are marked by vertical arrows corresponding to the six allowed transition ($\Delta M_S = \pm 1$, $\Delta M_I = 0$), corresponding to the M_I : $5/2 \rightarrow 5/2$, $3/2 \rightarrow 3/2$, $1/2 \rightarrow 1/2$, $-1/2 \rightarrow -1/2$, $-3/2 \rightarrow -3/2$, and $-5/2 \rightarrow -5/2$ nuclear transitions.

will therefore be better represented as a distributed average of all sites within the QD reflecting the ensemble averaged particle. The distribution can be treated using a g-strain and D-strain model to account for the distribution of EPR parameters.^{91,92}

Using the g- and D-strain model,⁹¹ Δg can be accounted for by measuring the frequency dependence of the linewidth (ΔH) of the EPR spectra. A linear shift in ΔH with resonance frequency will occur with increasing field, such that a plot of ΔH vs. frequency (ν) yields the equation, $\Delta H \approx h\nu/g^2\beta(\Delta g)$.⁹³ In addition to the g-strain term, the distribution of Mn(II) centers will produce line broadening reflecting the various crystal fields and axial distortion. Griscom, et al⁹⁴ treated this problem in glasses and observed that the linewidth can be defined as $\Delta H \propto D^2/(g^2\beta^2H_0)$. In the D-strain model,^{91,92} the distribution in Mn(II) sites produces a ΔD reflecting the average environment.

It is anticipated that a minimum of two sites (core and surface) each with their own distributions will be required to account for the EPR of Mn:CdSe QDs reflecting a core Mn(II) center surrounded by four-Se atoms and a surface passivated Mn(II) site surrounded by three or fewer Se atoms. Therefore the linewidth of the EPR spectra should be a combination of average contributions from g- and D- for the two Mn(II) sites within the QD. Contributions from g- and/or D- strain will appear as line-broadening at low-field reflecting the ensemble of Mn(II) sites, but can appear as separate distributions if the core and surface of the QD can be spectrally resolved at high field.^{91,92} It is worth noting that earlier low field EPR measurements have not identified discrete surface and core Mn(II) sites directly for Mn:CdSe QD samples;⁸⁹ however, broad EPR lines are observed. Early attempts at analyzing the EPR pattern have suggested that either overlapping sextets are present that arise from surface and core sites,^{47,89,90,95} or contributions from a large D-value⁸⁹ and/or presence of forbidden transitions.⁹⁵ The field dependence of the EPR spectra for Mn:CdSe should elucidate the presence of overlapping Mn(II)

signals arising from micro-environment differences between the core and surface or the presence of axial asymmetry. In addition the linewidth response and frequency response for the g-, A-, and D- EPR parameters will allow the elucidation of the electronic microenvironments within Mn: CdSe QDs.

Field Dependent EPR Measurements. In Figure 3.3A, the frequency dependent EPR spectra for a 5.0 nm Mn(0.6%):CdSe sample measured at 34, 216, 324, and 406.4 GHz (298 K) are shown. In the EPR pattern at ≥ 216 GHz, two independent overlapping sextet patterns are resolved that overlap at low frequency (34 GHz in Figure 3.3A). Globally fitting the frequency dependent EPR spectra for the two discrete sextet patterns (Figure 3.3B and Figure 3.4) allows an accurate value of g-, A- and D, as well as the distribution in D (ΔD) and g (Δg) to be obtained for the sites. The frequency dependence of g-, A-, and ΔH are shown in Figure 3.5. The g-value for site 1 and site 2 is extracted from the frequency dependence of the center field (Figure 3.5A and B), since the center field is field dependent; which means the g-value is field independent. The Δg value is extracted from the frequency dependence of the linewidth (Figure 3.5D). The value of ΔD is generated by fitting to a D-strain model.⁹¹

The extracted EPR parameters for site 1 and site 2 are $g_1 = 2.0042$ and $g_2 = 2.0014$, hyperfine constants $A_1 = 66.8$ G and $A_2 = 90.9$ G, and D values of $<10^{-5} \text{ cm}^{-1}$ (which is below the experimental resolution $3.3 \times 10^{-5} \text{ cm}^{-1}$) are measured in the 5.0 nm Mn: CdSe samples. A Δg_1 value of 0.0007 (site 1) and Δg_2 value of 0.0004 (site 2), and a ΔD_1 value of 0.03 cm^{-1} and $\Delta D_2 = 0.08 \text{ cm}^{-1}$ are obtained from the fit to the strain model. Values for g of 2.003 to 2.0123 and A-values from 66 to 70 G have been reported for Mn(II) doped into wurtzite CdSe QDs.^{29,45,89} The g- and A-values for the two sites are independent of field (Figure 3.5B and 3.5C); however the axial distortion (ΔD) is much larger and represents a larger ensemble average of environments for site 2.

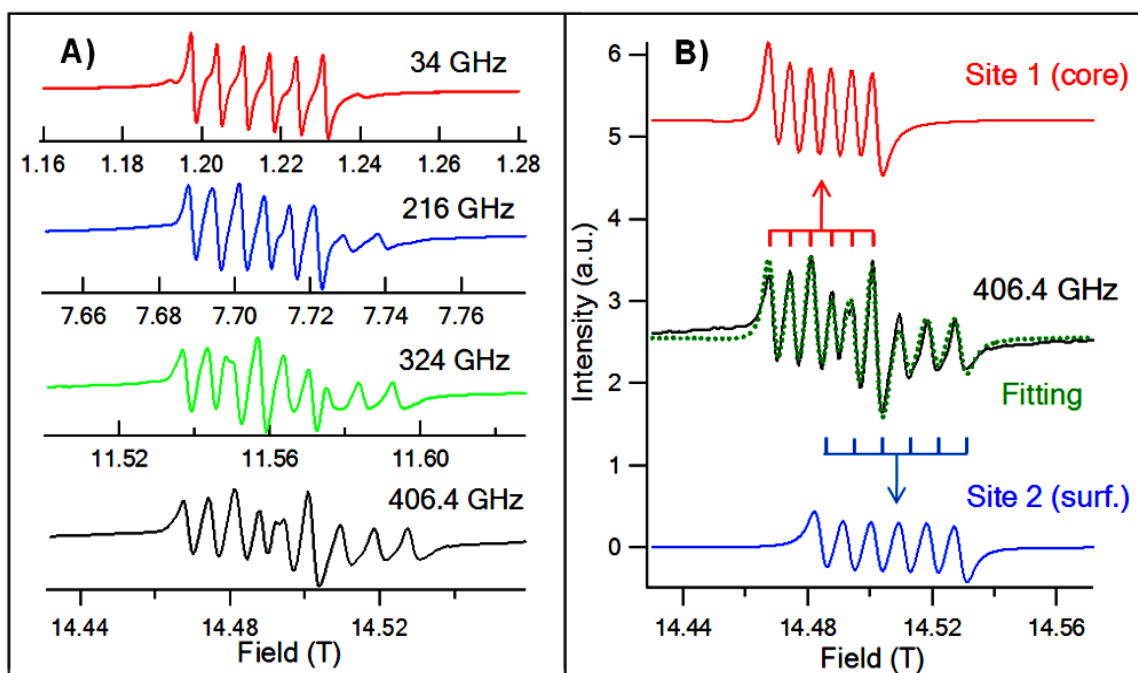


Figure 3.3. A) Frequency dependent EPR spectra (298K) for 5.0 nm diameter $\text{Mn}_x\text{Cd}_{1-x}\text{Se}$ ($x = 0.006$) (6% RMS size dispersity) measured at 34, 216, 324, and 406.4 GHz. B) Theoretical fit and deconvolution of the 406.4GHz HF-EPR spectra allowing definitive assignment of discrete sites for the Mn(II) occupying a substitutional Cd(II) site within the core (site 1, red), and surface (site 2, blue).

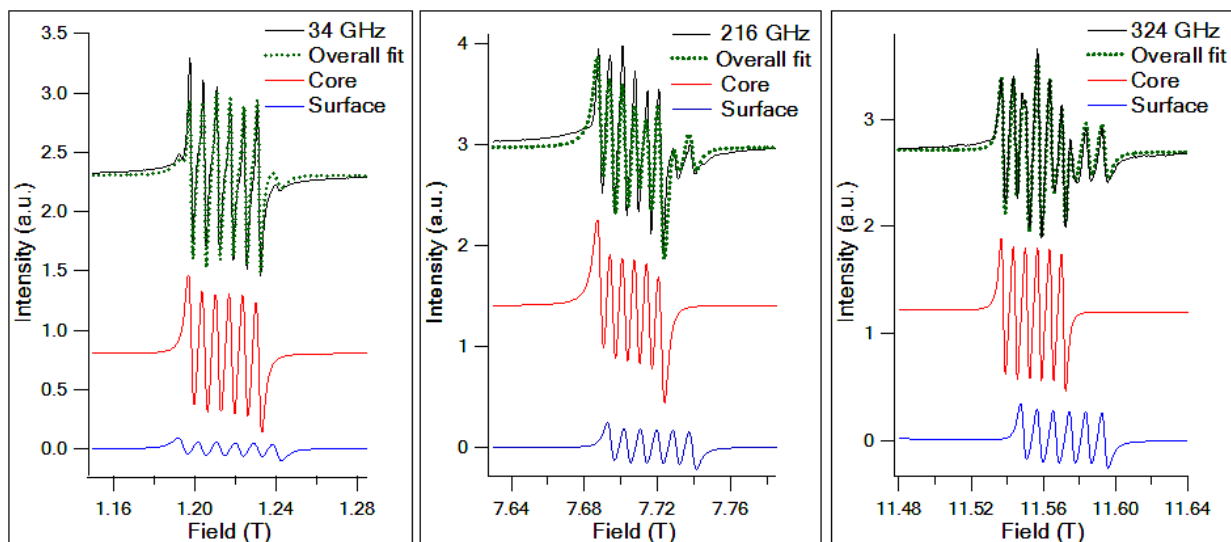


Figure 3.4. Fitting of the frequency dependent 5.0 nm Mn:CdSSe QD EPR spectra identifying the core (red), and surface (blue) components at 34 GHz, 216 GHz and 324 GHz EPR data.

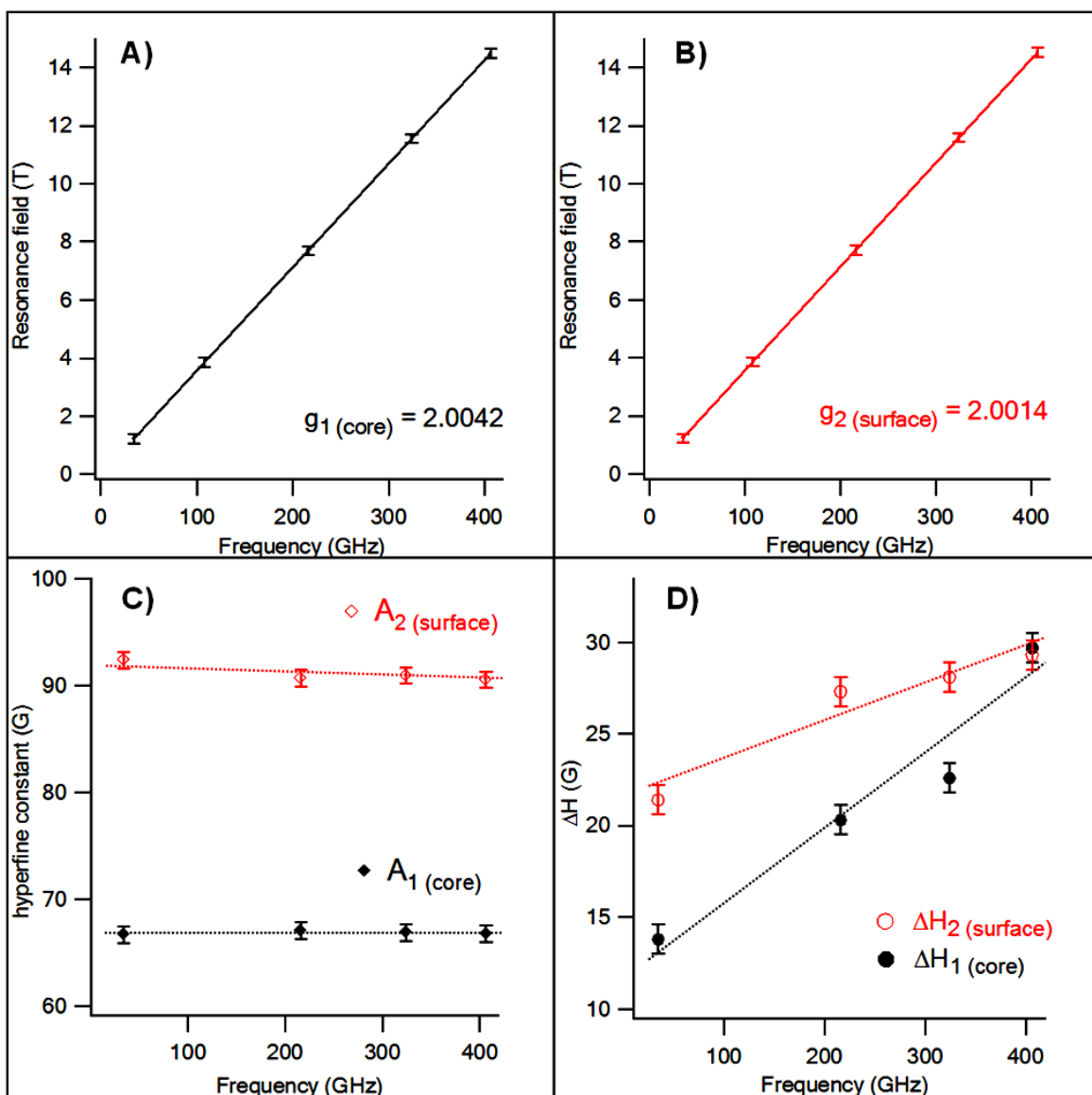


Figure 3.5. Frequency dependence of central resonance field for A) site 1 and B) site 2, C) Hyperfine constant (A), and D) Linewidth (ΔH) at 298 K for the 5.0 nm diameter Mn_xCd_{1-x}Se (x = 0.006). The dashed lines are guides to the eye.

The calculated value of D for the 406.4 GHz EPR spectra extracted from the spin Hamiltonian fit for the two sites in the 5.0 nm Mn:CdSe sample (Figure 3.3B) is smaller than reported in single crystal Mn:CdSe samples likely reflecting the distribution of Mn(II) in the QD. Fitting the high frequency data of site 1 to the D -value observed in single crystal Mn(0.0025%):CdSe ($D = 15.0 \times 10^{-4} \text{ cm}^{-1}$)⁴⁵ or the previously reported value for D extracted from a 4.6 nm Mn(0.1%):CdSe QD ($D = -82 \times 10^{-4} \text{ cm}^{-1}$)⁸⁹ does not allow the HF-EPR spectra to be adequately fit (Figure 3.6). The distribution in D and contributions from g -strain likely obscures the D -value in the QD power sample. Contribution to the line broadening from size dispersity is considered in the size dependent EPR data.

Remembering that the linewidth for a site will be linearly dependent on the field,⁹¹ one expects ΔH to exhibit a slope of *zero*, since $H/\nu = 0.071448/g$, if no distribution in the Mn(II) centers exist.⁹³ Therefore, the frequency dependent EPR linewidth (ΔH) for the 5.0 nm Mn:CdSe sample in Figure 3.5D can allow some insight into the Mn(II) distribution of microenvironments experienced within the QD. In Figure 3.5D, the positive slope for ΔH_1 and ΔH_2 is observed that is indicative of the presence of Mn(II) distributions in both the site 1 and site 2. Analyzing the slope yields a value of g -strain of 0.0007 for site 1 and a g -strain of 0.0004 for site 2. The larger g -strain for the site 2 can be interpreted as a greater distribution of crystal sites for Mn(II) doping within the site 2 of the QD.

Assignment of the Mn(II) Sites. The observation of two frequency resolvable sextet patterns indicate two similar but discrete Mn(II) sites exist within the QD sample. Of the two sites in the EPR, site 1 is the more easily assigned from literature values for Mn:CdSe single crystals.⁴⁵ Site 1 in the HF-EPR spectrum can be assigned to a Mn(II) center surrounded by four Se atoms in a wurtzite crystal by comparison to reported values of g - and A - in single crystal

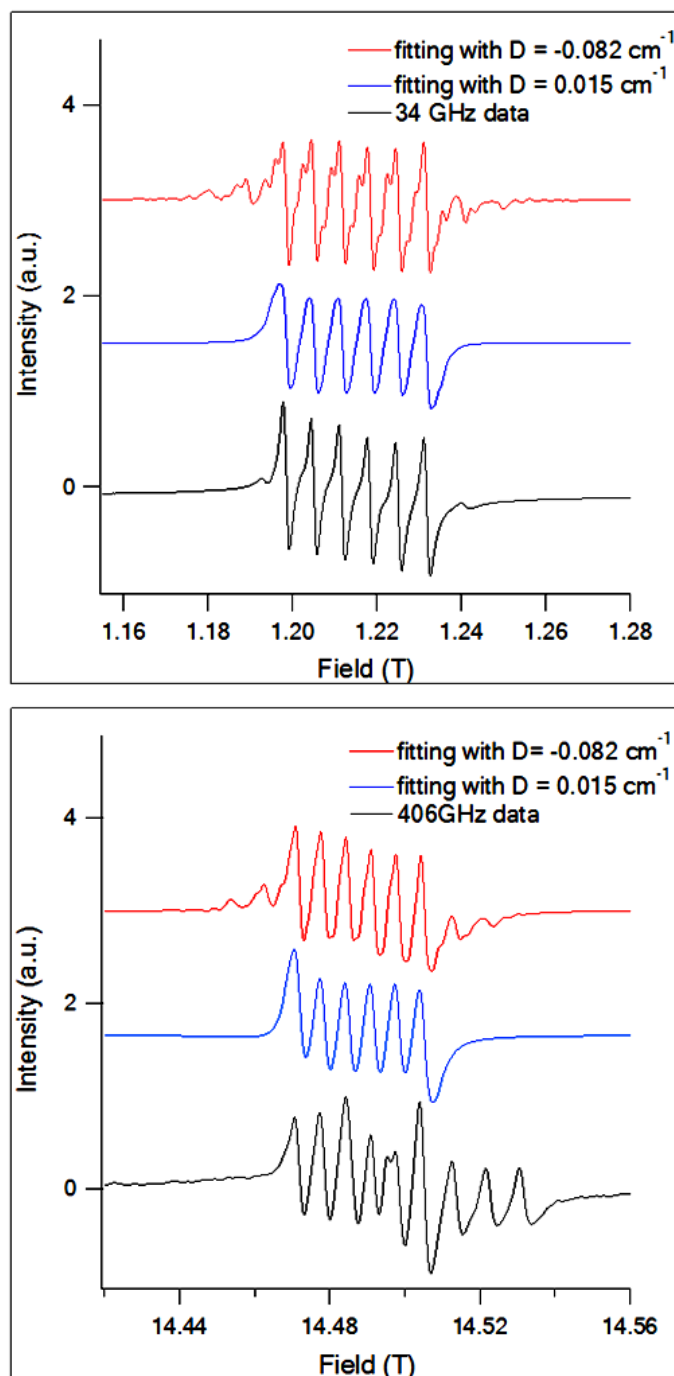


Figure 3.6. Fitting site 1 (core) of the EPR spectra for the 5.0 nm Mn:CdSe QD at fixed values of D for the single crystal ($D = 0.015 \text{ cm}^{-1}$) and for reported Mn:CdSe QDs ($D = -0.082 \text{ cm}^{-1}$).

Mn:CdSe ($g = 2.003$, $A = 67.2$ G, $D = 15 \times 10^{-4}$ cm⁻¹).⁴⁵ The EPR pattern for site 2 however is inconsistent with a core doped Mn(II) center in wurtzite symmetry.

Site 2 may arise from a discrete site within the QD reflecting a surface site, the presence of two different QD structures (wurtzite vs sphalerite) present in the QD ensemble, or the presence of an impurity Mn(II) transition metal coordination compound trapped in the ligand layer (not bound to the QD). Contributions from Mn(III) impurities in the QD sample can be rejected based upon the lack of the observation of an EPR signature for Mn(III) ($S = 2$).⁹⁶

Mn L_{3,2} edge XANES data (Figure 3.7) spectra confirm the presence of Mn(II) and the absence of Mn(III) or Mn(IV) in the sample by comparison to the reported Mn L_{3,2} edge XANES data for MnO, Mn₂O₃ and MnO₂ standards.⁹⁷ Additionally, the absence of Mn oxides in the samples is confirmed by pXRD and FT-IR measurements (Figure 3.1), where no spectral features are observed.

Experimental insight into the lattice structural environment for the Mn(II) center can be gained by fitting the XANES data. The Mn L_{3,2} edge spectra is consistent with the description of the Mn(II) ion in a tetrahedral crystal field as inferred from multiplet simulations⁹⁸ of a Mn(II) ion in a T_d crystal field ($10Dq \sim 300$ meV). This crystal field energy value mimics the bulk CdSe crystal field $10Dq$ values suggesting that the Mn(II) ions are occupying Cd(II) sites within the wurtzite CdSe lattice, confirming doping of the CdSe QD is achieved. Unfortunately in the XANES data, it is unclear if a discrete surface or core site can be assigned or information pertaining to the magnitude of axial distortion at the Mn(II) center present in a wurtzite crystal due to the Mn L_{3,2} edge due to line broadening. The reduction in the absorption features at ca. 638 and 644 eV could be explained by a size dependent change in the crystal field energy, a distribution in the crystal field energy for the Mn(II) ions doped at various depths within the QD, or to an increase in surface related features at smaller particle sizes.. The inherent

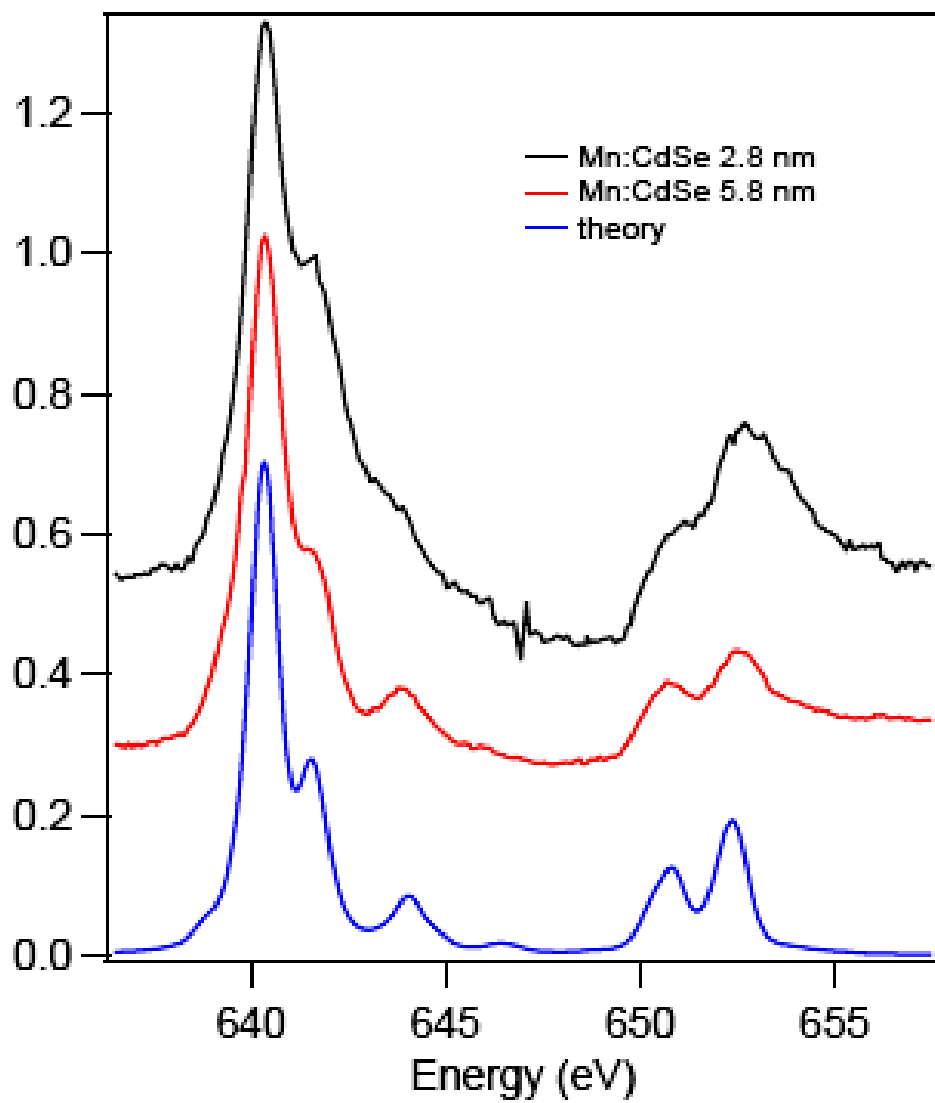


Figure 3.7. Mn L_{3,2} edge X-ray absorption spectra of the Mn:CdSe QDs.

inhomogeneous broadening present in QDs leaves quantitative analysis of these absorption features unachievable at this stage.

The possibility that site 2 arises from a sphalerite impurity phase in the isolated wurtzite QDs cannot be rejected, although the pXRD and TEM diffraction patterns are assignable as wurtzite.⁷⁷ Although no EPR data is available for Mn:CdSe in the sphalerite phase, it is believed that the sphalerite phase cannot account for the large shift in the EPR parameters of site 2, since the wurtzite and sphalerite phase for Mn:ZnS have nearly identical values for g - ($g_{(w)} = 2.0016$, $g_{(s)} = 2.0021$) and A - ($A_{(w)} = 69.6$ G, $A_{(s)} = 68.2$ G).^{99,100} The similarity in the values suggest sphalerite contamination cannot explain the observation of two discrete EPR signatures for Mn:CdSe.

Unfortunately the two other possibilities, Mn(II) isolated in the ligand matrix and Mn(II) occupying a QD surface site, cannot be as summarily ruled out since the g - and A -value for site 2 can be accounted for by coordination of the Mn(II) ion by a strong-field ligand either for a Mn(II) coordination complex trapped in the ligand layer or for a ligand passivated Mn(II) center at the surface of the QD. Distinguishing between these possibilities can be initially accomplished by considering the intensity ratio of site 2 to site 1 in the EPR spectra for the 5.0 nm Mn:CdSe QD. In Figure 3.3, site 2 accounts for 33% of the signal at 406.4 GHz which is in good agreement with the theoretically predicted value for the surface to volume ratio of Cd sites within a 5.0 nm CdSe QD. The agreement with the predicted surface to volume ratio suggests the assignment of site 2 can be described as a Mn(II) site at the surface of the QD rather than a Mn(II) coordination complex in the ligand matrix.

Influence of Ligand Exchange on EPR Parameters. Further evidence of the assignment of site 2 to the QD surface can be gained by measuring the EPR spectra for 5.0 nm Mn:CdSe QD ligand exchanged by a series of moderate to strong coordinating ligands, namely DDN, TOP,

TOP-Se, DDA, and py (Figure 3.8). The studied ligands represent strong field ligands with various π -acceptor capabilities (DDN>TOP>TOP-Se>DDA~py). As shown earlier, the ligand back-bonding strength can have a dramatic effect on the surface state energies in CdSe QDs³² and thus should perturb the observed hyperfine exchange for Mn(II). For all ligand exchanged samples, the number of EPR sextets, the g-value for the EPR sextets, and the intensity ratio of site 1 to site 2 are constant across the *five* samples as expected for a Mn(II) at a surface site on the QD; however, the A-value for site 2 is not constant. The A-value for site 1 does not shift (A = 66.8 G) following ligand exchange, which is not surprising for a core site (Table 3.1). The A-value for site 2 shifts for the ligand series with values of 91.3 G (DDN), 91.2 (TOP), 91.1 (TOP-Se), 90.9 (DDA), 90.5 (py). The increase in A-value across the ligand series tracks the increased π -acceptor strength for the ligand, which would be consistent with assignment of site 2 to a surface passivated site.^{32,101} Although the same observation could be achieved for a Mn(II) coordination complex in the ligand matrix, the reproducibility of the intensity ratios and the A-values across multiple repeat experiments coupled to the lack of a change in the intensity ratio of site 1 to site 2 for each ligand exchange strongly suggests the Mn(II) site 2 EPR spectra arises from a Mn(II) occupying a surface site on the QD. Consistent with the assignment of site 2 not being associated with a transition metal coordination complex in the ligand matrix, a sample prepared by reaction of MnBr₂ with DDA produces a larger A-value (94.1 G) than the observed value for site 2 (Figure 3.9).

Surface Doped Mn:CdSe EPR Parameters. Further evidence of site 2's assignment being associated with a Mn(II) ion bound at the surface of the QD can be observed by inspection of the EPR spectrum for a surface doped Mn:CdSe QD, wherein no core doping by Mn(II) exists. The EPR data for a 5.5 nm surface doped Mn(0.4%):CdSe sample reveals an EPR signature

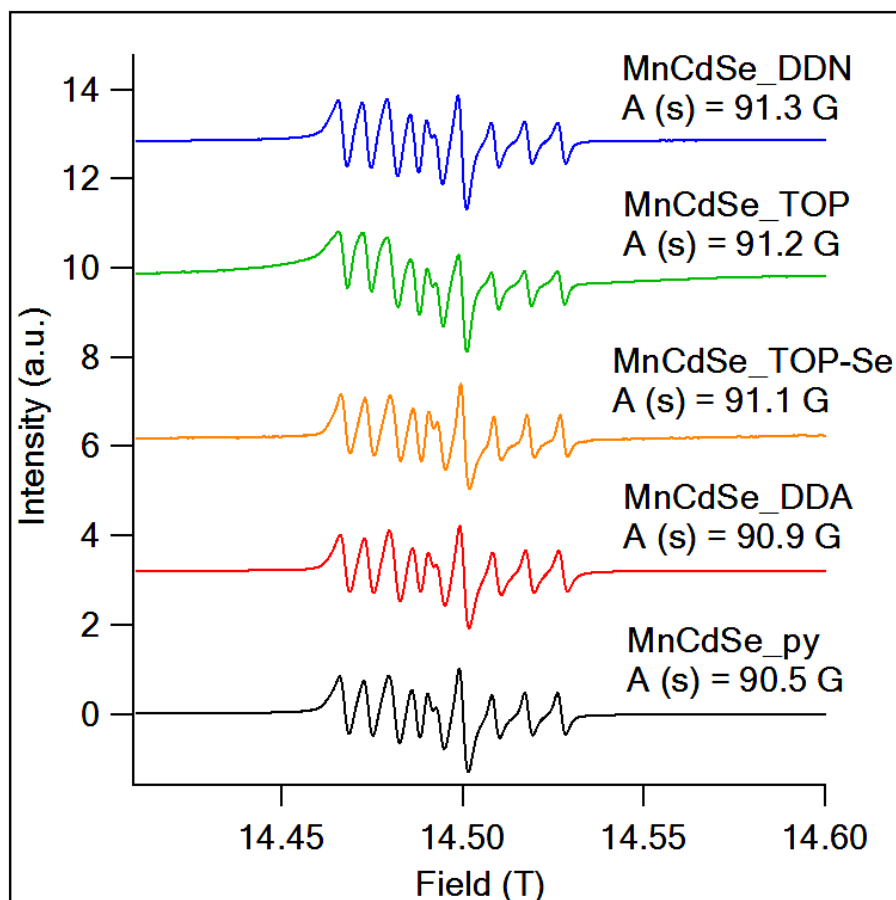


Figure 3.8. 406.4 GHz HF-EPR spectra for 5.0 nm $\text{Mn}_x\text{Cd}_{1-x}\text{Se}$ ($x = 0.006$) ligand exchanged by DDN, TOP, TOP-Se, DDA, and py.

Table 3.1. Influence of ligand exchange on EPR parameters of Mn:CdSe QDs.

	g		A (G)		D(cm ⁻¹)		ΔD (cm ⁻¹)	
	Surf.	Core	Surf.	Core	Surf.	Core	Surf.	Core
DDN	2.0042	2.0014	91.3	66.8	0	0	0.09	0.04
TOP	2.0042	2.0014	91.2	66.8	0	0	0.09	0.04
TOP-Se	2.0042	2.0014	91.1	66.8	0	0	0.08	0.04
DDA	2.0042	2.0014	90.9	66.8	0	0	0.08	0.03
py	2.0042	2.0014	90.5	66.8	0	0	0.08	0.04

consistent with only site 2 (Figure 3.10) with a $g = 2.0014$; $A = 91.1$ G, and $D = 0$ cm^{-1} value for the surface doped Mn:CdSe sample.

Proof of the presence of the Mn(II) ion at the QD surface only in the 5.5 nm surface doped Mn:CdSe QD can be gained by following the EPR pattern as the QD is chemically etched. Chemically etching using an oxidizing acid ($\text{HCl}/\text{H}_3\text{PO}_4$) removes ~ 1 nm of the QD diameter (~ 0.5 nm radius) based upon the shift in the absorption data for the Mn:CdSe sample (Supporting Figure 3.11). As shown in Figure 3.10C, complete loss of the EPR signal for the surface doped QD is observed following etching, as expected. Chemically etching of stochastically doped 5.0 nm Mn:CdSe QD containing both core and surface doped sites results in both site 1 and site 2 being observed in the EPR during all etching steps (Figure 3.10B). Plotting the change in the intensity ratio for site 2 (surface) versus the change in size of the QD for the stochastically doped 5.0 nm Mn:CdSe sample, where the size is extracted from the optical absorption of the first exciton (Figure 3.11B), reveals the intensity of site 1 to site 2 follows the trend-line for a theoretical surface to volume ratio in an oblate QD (Figure 3.12). The oblate shape for the QD with a 1.2:1 c/a axis ratio used in the theoretical trend line in Figure 3.12 is extracted from inspection of the TEM data in Figure 3.1B. It is clear from comparison of the data, that the trend line underestimates the site intensity in the EPR data. The theoretical line is only a trend line as it assumes a 1:1 Cd to Se ratio in the QD and does not attempt to correct for QD faceting. The deviation of ideal spherical shape and particle faceting may account for the higher surface contribution than theoretically calculated.

Size Dependent EPR properties. The assignments of a core (site 1) and surface (site 2) for the two frequency resolved EPR signatures in a ~ 5.0 nm Mn(0.6%):CdSe sample can be further confirmed by inspection of the size dependent HF-EPR spectra (406.4 GHz) for 1.3, 2.8, 5.0, and 5.8 nm Mn(0.6%):CdSe (Figure 3.13A). The EPR parameters (g , A , D , ΔD , and ΔH) are

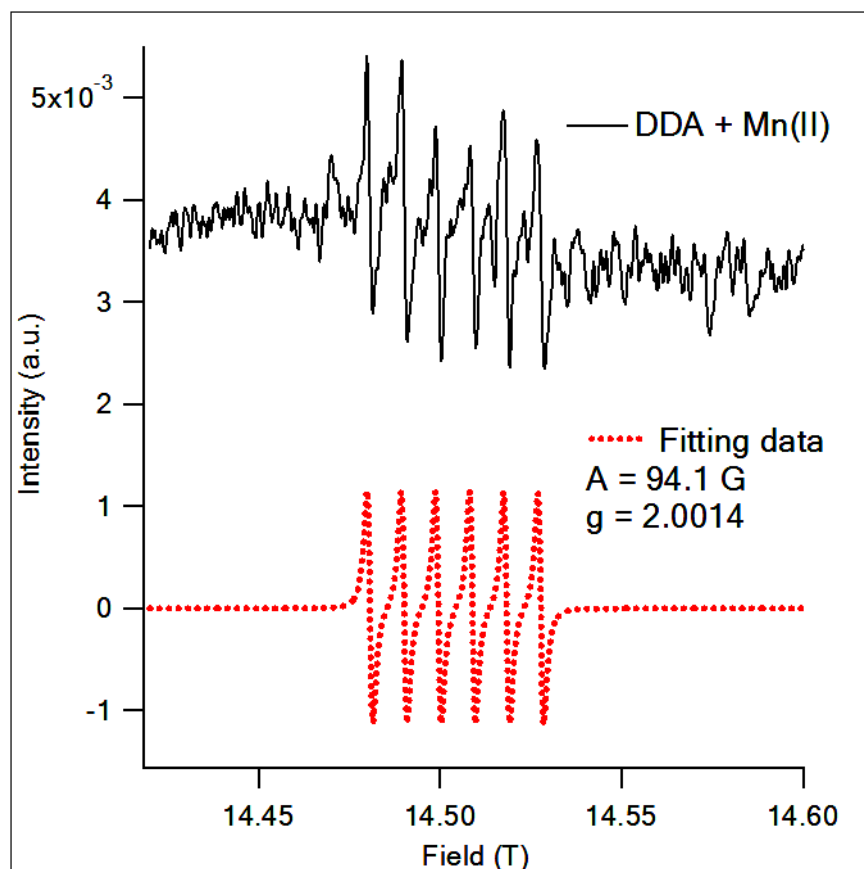


Figure 3.9. 406.4 GHz HF-EPR spectra for the MnBr_2 with DDA, the fitted A-value is 94.1 G.

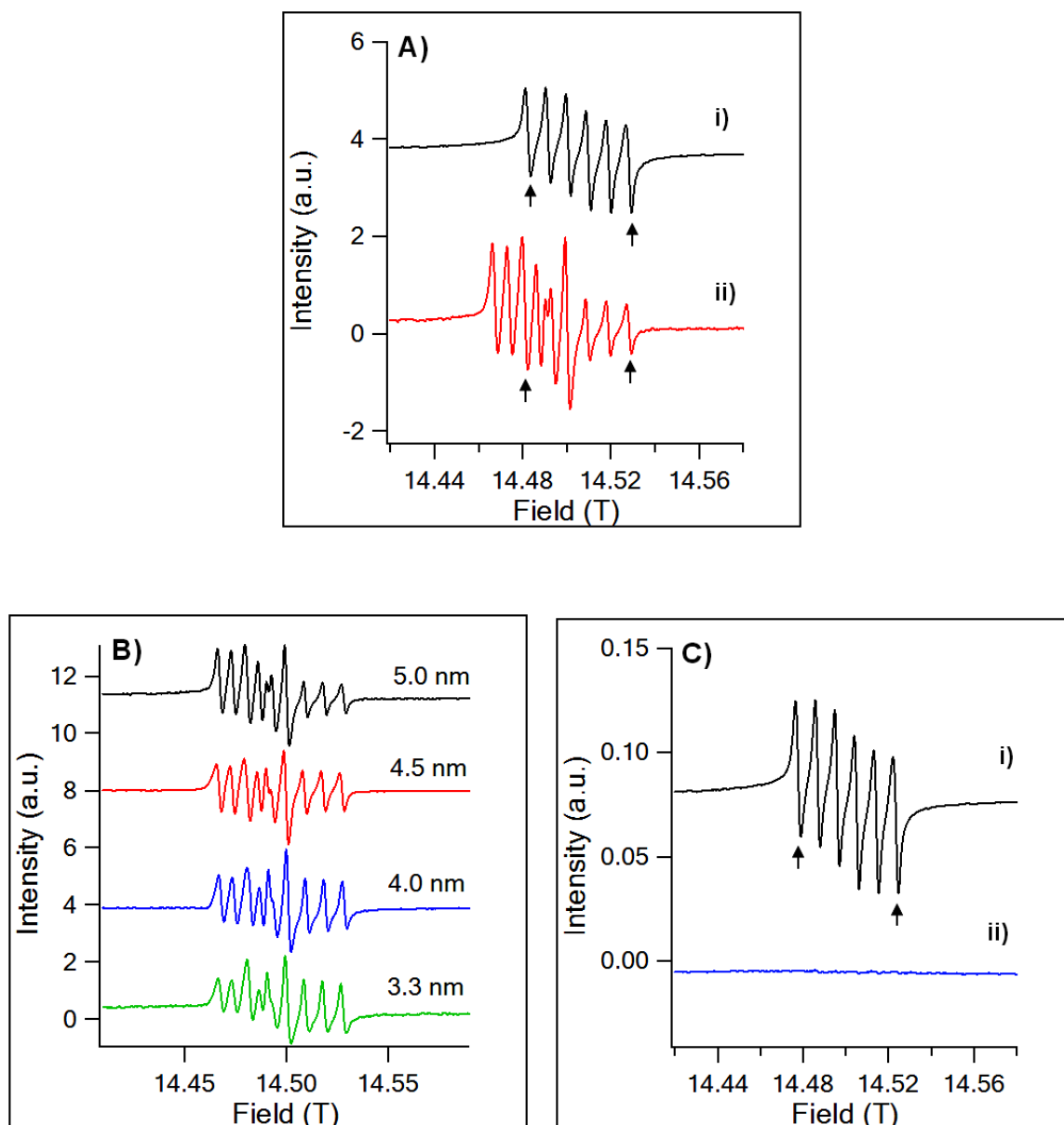


Figure 3.10. A) EPR measurements at 406.4 GHz (298 K) for i) 5.5 nm surface doped (black) Mn:CdSe (0.4%) and ii) 5.0 nm stochastically doped (red) Mn:CdSe (0.6%), EPR evolution of Mn:CdSe QDs following acid etching of B) 5.0 nm stochastically doped Mn:CdSe, and C) 5.5 nm surface doped Mn:CdSe. The arrows in A) and C) indicate the surface component of the EPR spectra in Mn:CdSe corresponding to $M_I: 5/2 \rightarrow 5/2$ (left) and $-5/2 \rightarrow -5/2$ (right) transitions.

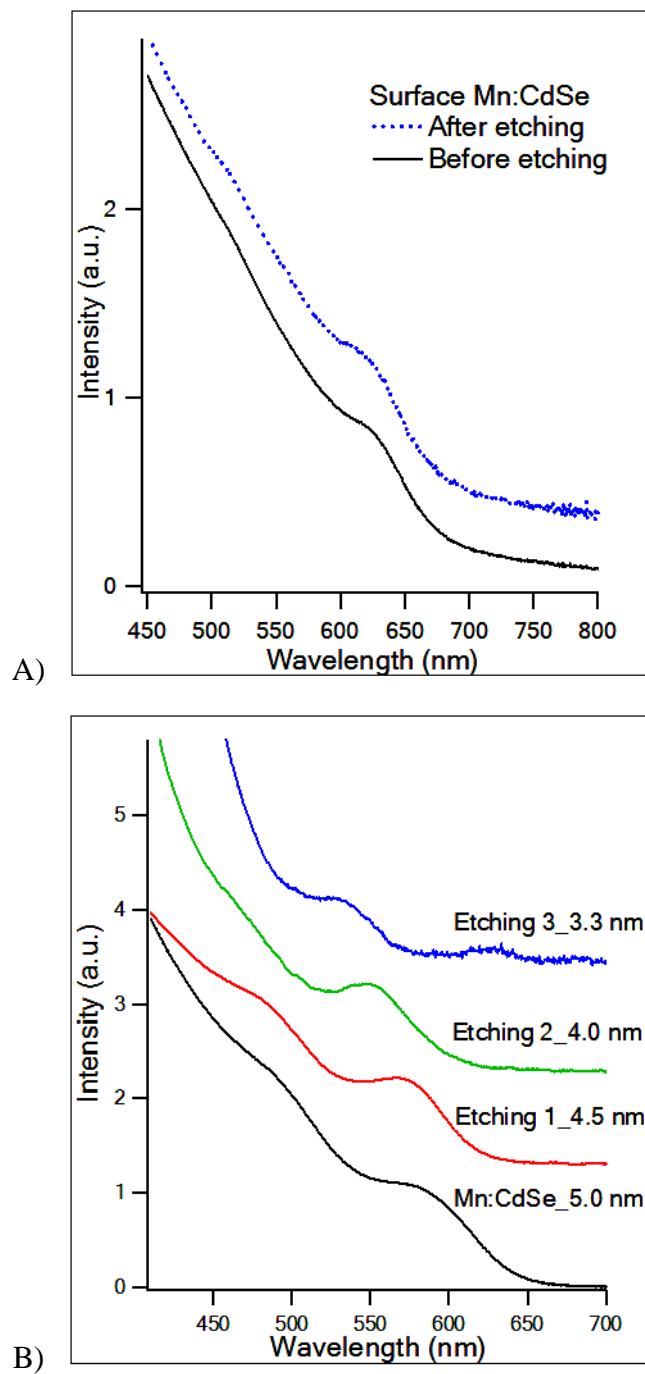


Figure 3.11. Absorption spectra before and after acid etching for A) 5.5 nm surface doped and B) 5.0 nm stochastically doped Mn: CdSe QDs.

listed in Table 3.2. A doping concentration of 0.06 ± 0.003 for all samples is confirmed by XRF analysis of the Mn to Cd ratio. The EPR spectra in Figure 3.13 exhibit two distinguishable EPR sextets for the 2.8, 5.0, and 5.8 nm QDs, but a single EPR sextet for the 1.3 nm QD sample. The two sites in the 2.8 to 5.8 nm size regime have identical g- and A-values to the measured properties for site 1 and site in the 5.0 nm Mn: CdSe sample, therefore allowing assignment of site 1 to a QD core and site 2 to a QD surface site. An earlier X-band EPR study suggested a size dependence for the g-value is observed for Mn: CdSe;⁹⁰ however, no significant size dependence is observed in our study which involves measurements with a much higher degree of precision.

In Figure 3.13, the 1.3 nm Mn: CdSe sample's EPR spectra has a g- and A-value consistent with only the surface site (site 2) and no distinguishable feature assignable to site 1 (core-site), implying the 1.3 nm QD does not contain a core site or more likely the Mn(II) does not occupy a core site in the 1.3 nm QD sample. While the observation of only site 2 in the 1.3 nm QD is intriguing, it is not surprising. At 1.3 nm, the QD contains only four lattice planes and is on the order of the size predicted to be the critical nuclei size for CdSe QD growth.^{31,83} Nucleation theory predicts the QD must form as a pure nucleus prior to growth. Such behavior would result in the exclusion of Mn(II) centers from the QD core prior to the growth phase and therefore isolation of the Mn(II) to the surface sites in CdSe QDs below 2 nm.

The ratio for site 2 (surface) relative to site 1 (core) is observed to decrease with increasing QD size in Figure 3.13A. A linear relationship is observed for the intensity of site 2 with increasing surface to volume ratio (decreasing QD size) as demonstrated in Figure 3.13D. The increasing intensity for site 2 scales linearly in rough agreement with the theoretically calculated surface to volume ratio for an oblate QD with a 1.2:1 c/a ratio. The lack of agreement in the line is likely reflective of particle faceting and the approximation of the QD as a spherical particle, as discussed in the previous section.

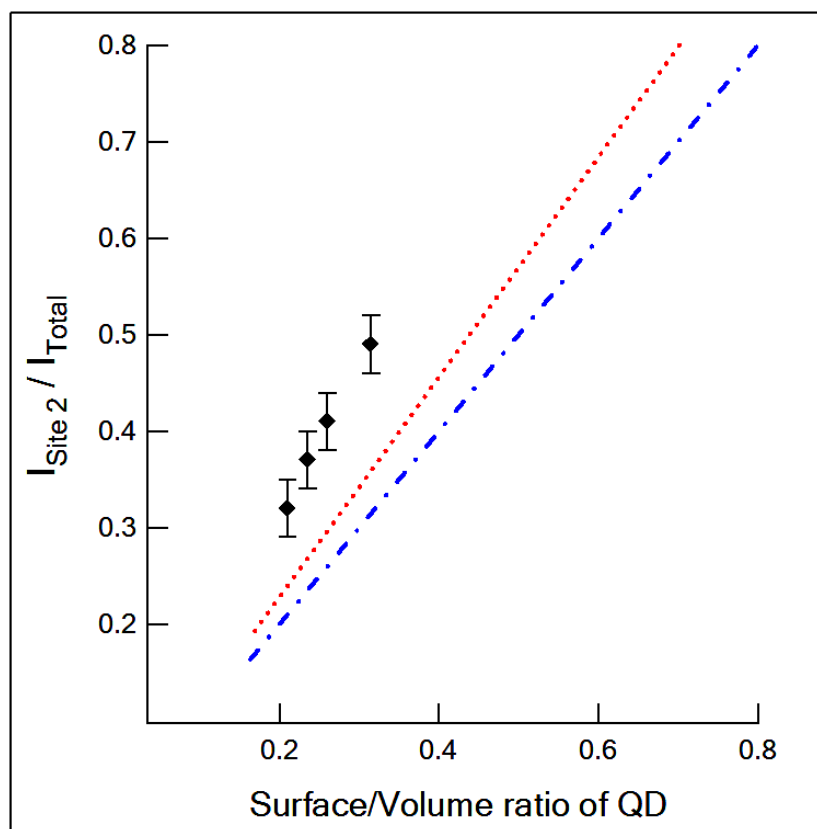


Figure 3.12. Plot of the change in the site 2 to total Mn(II) sites intensity for acid etched QDs measured by 406.4 GHz EPR. The dotted lines represent theoretical plots for a spherical CdSe QD (blue) and for an oblate QD with a 1.2:1 c/a ratio (red).

Table 3.2. Size dependent EPR parameters of Mn: CdSe QDs.

Size (nm)	g		A (G)		D(cm ⁻¹)		ΔD (cm ⁻¹)		ΔH (G)	
	Surf.	Core	Surf.	Core	Surf.	Core	Surf.	Core	Surf.	Core
1.3	2.0013	-	89.1	-	0	-	0.10	-	19.5	-
2.8	2.0014	2.0042	90.8	66.8	0	0	0.06	0.04	24.2	25.8
5.0	2.0014	2.0042	90.8	66.8	0	0	0.08	0.03	26.4	28.1
5.8	2.0014	2.0042	90.7	66.8	0	0	0.05	0.03	24.2	23.5

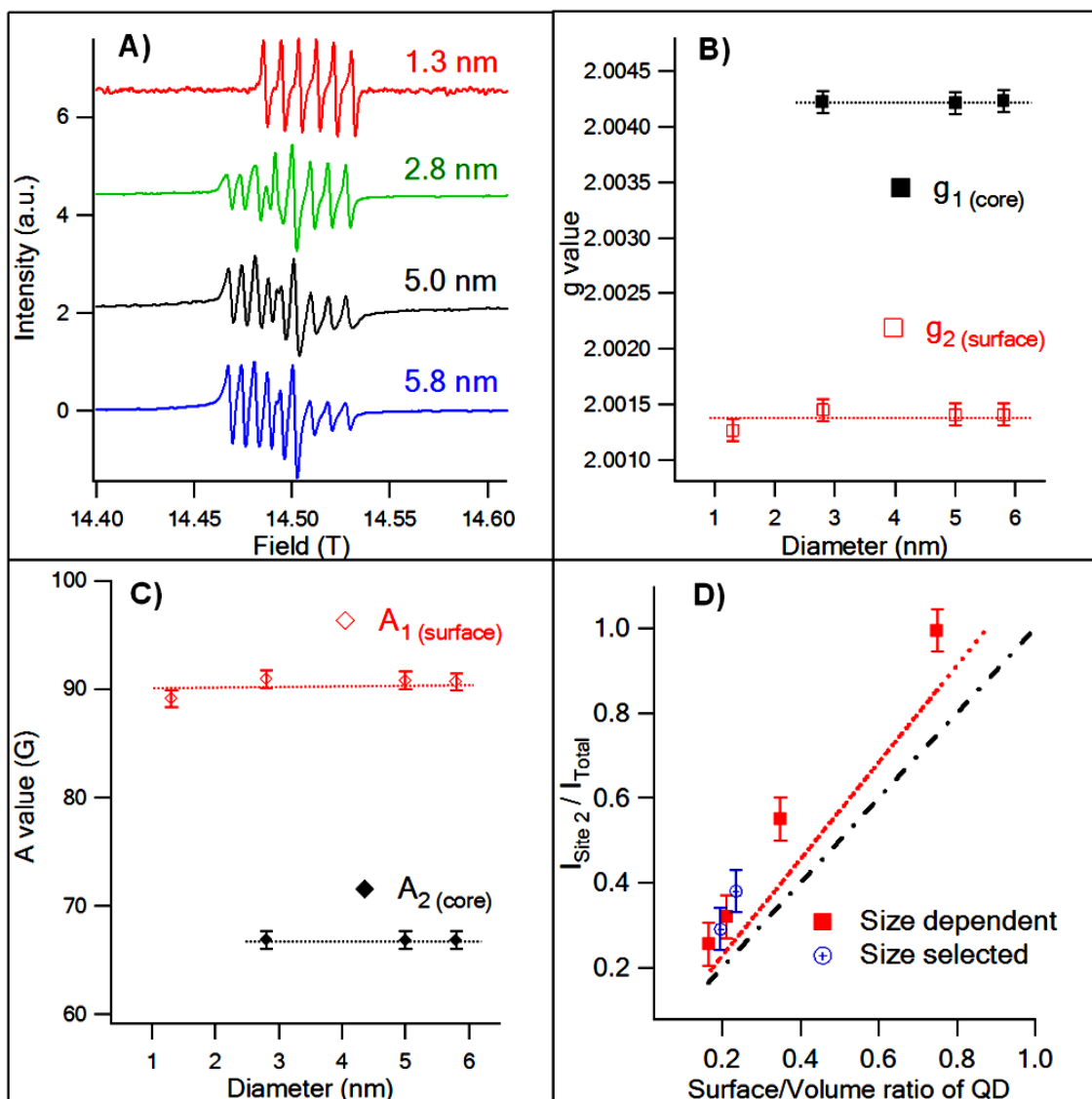


Figure 3.13. Size dependent A) EPR measurements at 406.4 GHz (298 K) for 1.3 nm, 2.8 nm, 5.0 nm and 5.8 nm $\text{Mn}_x\text{Cd}_{1-x}\text{Se}$ ($x = 0.006$), B) g-value, C) Hyperfine constant (A), and D) Plot of the size dependence of the intensity of site 2 relative to the total Mn(II) EPR intensities (at 406.4 GHz and 298 K). Theoretical lines for an ideal spherical CdSe (black dot line) and for an oblate QD with a 1.2:1 c/a ratio (red dot line) are shown.

Although no effect on the g- or A-value for site 1 and site 2 are observed across the size domain and the g- and D-strain model accounts for line-broadening in the EPR due to a distribution of Mn(II) sites,^{91,92} the effect of size dispersity on the EPR spectra can be analyzed by selectively precipitating Mn:CdSe QDs to narrow the size dispersity. The EPR spectra for selective precipitation of the 5.0 nm Mn:CdSe QD sample with a 5-6% size dispersity is shown in Figure 3.14. Inspection of the linewidth (ΔH) for the three samples indicates a narrowing of the EPR pattern is observed following size selective precipitation resulting in a reduction in $\Delta H_{5.0 \text{ nm (core)}} = 29.7 \text{ G}$ to $\Delta H_{4.6 \text{ nm (core)}} = 26.8 \text{ G}$ and $\Delta H_{5.2 \text{ nm (core)}} = 25.3 \text{ G}$ for site 1 and for site 2 from $\Delta H_{5.0 \text{ nm (surface)}} = 29.3 \text{ G}$ to $\Delta H_{4.6 \text{ nm (surface)}} = 21.7 \text{ G}$ and $\Delta H_{5.2 \text{ nm (surface)}} = 22.1 \text{ G}$. The rather small reduction in linewidth indicates size dispersity plays a small role in the observed EPR linewidth, cannot be the only factor in the linewidth of the EPR spectra. It is worth noting, the g-value and A-values for the 4.6 nm and 5.2 nm selectively precipitated samples are identical to the parent 5.0 nm Mn:CdSe EPR parameterization values, however, the intensity ratio of site 1 to site 2 is observed to change. Plotting the samples on the size dependent EPR plots (Figure 3.13D) reveals the site ratio tracks the size of the QD. This provides further proof the Mn(II) site 2 is from a Mn(II) coordinated to the QD surface and not free in the ligand layer.

3.4 Conclusion

The HF-EPR experiments confirm that the QD micro-environment can be divided into a surface (site 2) and core (site 1) site. Based on the large A-value (90.9 GHz), passivant dependence for A-value, lower EPR intensity for site 2 to site 1 with increasing size, and the observed changes in the EPR in the etching experiment, the EPR pattern for site 2 is assigned to a ligand passivated surface site of the QD. Similar A-values ($A = 89\text{--}95 \text{ G}$) have been reported for Mn(II) occupying surface sites on QDs obtained from low frequency EPR measurements in

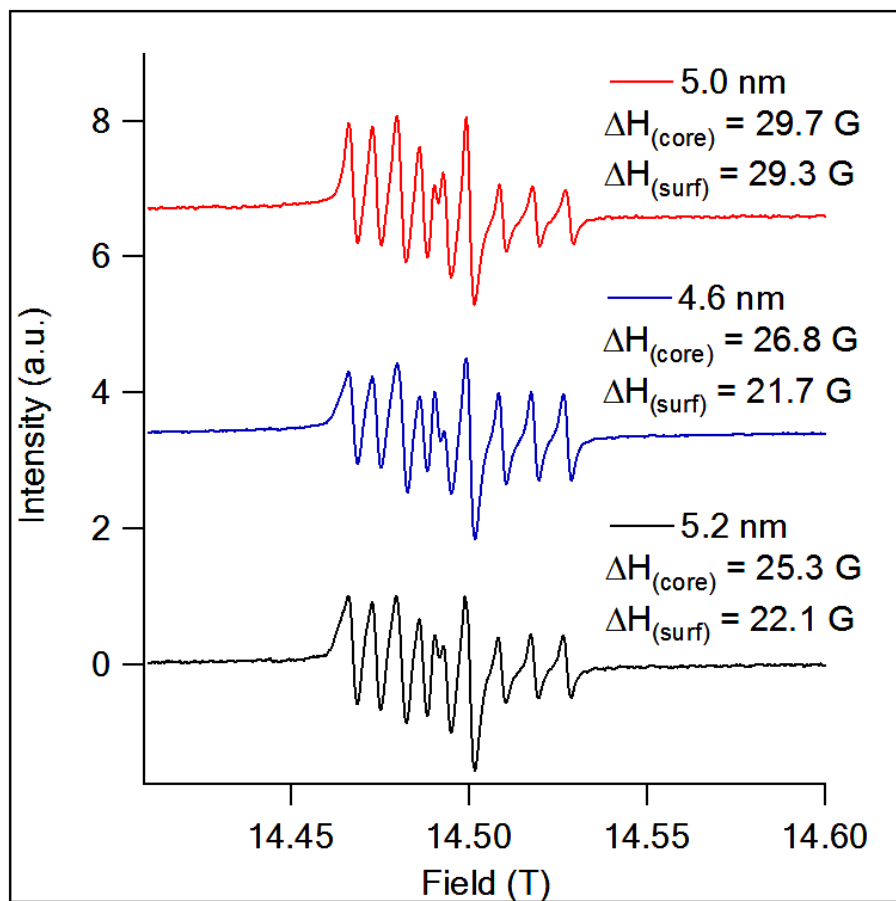


Figure 3.14. EPR measurements at 406.4 GHz (298K) on size selected QDs for A) 5.0 nm prior to size selection (red), B) the 4.6 nm (blue) and C) 5.2 nm (black).

Mn:CdSe,³⁶ Mn:CdS,¹⁰² and Mn:ZnSe⁴⁶ QDs. The difference in A- and g-values for the two sites reflect the difference in the crystal field experienced by the Mn(II) ion at their respective sites. As anticipated the change in the A-value for site 2 (surface) with increasing π -acceptor strength of the passivant shell confirms the reports of greater stabilization in QDs passivated by ligands containing d-backbonding.^{32,51}

As anticipated the Mn(II) local environment depends on the site of Mn(II) doping, whether in or near the passivant shell. Insight into the distribution for the crystal field surrounding the Mn(II) sites within the core and surface of the QD is elucidated by the g- and D-strain model. The results are consistent with an earlier report that a Mn(II) doped into a shell of a core-shell QD experiences different chemical environments as the Mn(II) center is moved away from the core QD towards the passivant shell.^{67,69} Although further temperature dependent HF-EPR studies are needed to confirm this distribution of Mn(II) environments within the core and surface of the QD, the magnitude of Δg and ΔD values potentially reflects the larger number of Mn(II) micro-environments for the core relative to the surface based on extrapolation of the Δg values in the 5.0 nm Mn:CdSe QD, but the surface has a larger distribution in the axial distortion (ΔD) in all QDs studies which is believed to reflect the surface ligation of the Mn(II) centers. The observation of a distribution is consistent with the line broadening in the XANES Mn L_{2,3} spectroscopy data. Analysis of the effects of ligation on the core and surface of a QD provides a better model of how a QD reconstructs as a function of size following ligand passivation.

CHAPTER FOUR

EVIDENCE OF SPINEL PHASE FORMATION IN Cr DOPED ZnSe QUANTUM DOTS

Cr doped ZnSe quantum dots (QDs) have been prepared from a single source precursor method. Surprisingly Cr(III) incorporation is obtained instead of Cr(II), as demonstrated by soft x-ray absorption near edge (XANES) spectroscopy, absorption spectra, EPR, and magnetization measurements. The Cr $L_{2,3}$ edge spectra in XANES measurement found the Cr(III) ion exists in a distorted octahedral (O_h) crystal field. Room temperature ligand field spectra confirm the pseudo- O_h symmetry of the Cr(III) sites by assign the ${}^4A_{2g} \rightarrow {}^4T_{2g}$ transition. The crystal field splitting energy is estimated from absorption spectra to be 2.07 eV. ZFC/FC susceptibility measurement shows paramagnetic (PM) behavior of the QDs with antiferromagnetic (AFM) coupling at low temperature, which can be understood by the dominating direct AFM exchanging between Cr(III) in the $ZnCr_2Se_4$ phase embedded in the ZnSe lattice. The formation of the $ZnCr_2Se_4$ phase may suggest unique stabilities can be obtained due to the growth mechanism trapping kinetic structures or the nature of critical domain formation to initiate QD growth.

4.1 Introduction

Incorporating chromium into metal chalcogenides results in complex phase diagrams with multitude of possible structure and Cr oxidation state incorporation. The ion incorporation of Cr(I),^{103,104} Cr(II)^{105,106} and Cr(III)^{107,108} have been reported. These materials have attracted attention for nearly half a century due to their unique optical and magnetic phases reflecting the

complex interplay between electronic, lattice and spin degrees of freedom.^{109,110} Cr(I) is believed to be generated due to charge transfer between the chalcogenide sublattice and the Cr ion, while Cr(II) is a substitutional ion at the metal site forming a perfect solid solution with interesting near IR lasing properties.¹¹¹ The incorporation of Cr(III) into a metal chalcogenide lattice results in the formation of a AB_2X_4 spinel structure with the metal ion from group II occupying a tetrahedral (T_d) site and the Cr occupying an octahedral (O_h) site.¹¹² The phase diagram for Cr(III) to form of the chromium chalcogenide spinel exhibits a single phase point for MCr_2Se_4 ($M = Cd, Zn, Hg$), and formation of a co-crystal of MSe and Cr_2Se_3 outside this concentration region.¹¹³ The Cr-based chalcogenide spinels are perhaps the most exciting materials behave as magnetic semiconductors,^{112,114} where magnetic Cr(III) spins are viewed as naturally introduced into II-VI semiconductors AX ($ZnS, ZnSe, ZnTe, CdS, CdSe, CdTe$). The magnetic ordering behavior of the Cr(III) spins range from a ferromagnetic (FM) state in $CdCr_2Se_4$ to a helical spin state in $ZnCr_2Se_4$.¹¹⁵⁻¹¹⁷

The ability to dope Cr(III) into a metal chalcogenide quantum dot (QD) could allow new dilute magnetic semiconductor QDs (DMSQDs) to be investigated. Recent studies on $MM'X$ ($X =$ chalcogenide) ternary metal chalcogenide QDs have revealed that a rich magnetic behavior is obtained depending on the reaction conditions.^{52,84} Since QDs are generally isolated in a kinetically controlled reaction, the ability to isolate a core/shell, homogenous doped, or phase segregated structures arising from spinodal decomposition due to effective zone refinement as the nanocrystal grows in size, is dependent on the reaction conditions.^{22,31,51,118} In general, the incorporation of the secondary metal ion having the same charge leads to substitutional incorporation on the metal lattice site with only an average lattice perturbation that follows the empirical predictions of Vegard's law.³⁰ Doping with a metal ion with a different oxidation state often leads to vacancy formation or phase segregation to ensure the principle of charge neutrality

is obeyed.^{52,84} In Al:ZnO, doping is allowed but appears to motivate vacancies.¹¹⁹ Such richness in the phase diagrams has been reported in bulk metal chalcogenides where internal phase inclusions are incorporated endotaxially into the crystal.¹²⁰

In this manuscript, we explore the incorporation of Cr(III) ions into a ZnSe QD. The incorporation of between 0.4% to 4% Cr(III) into the ZnSe is observed to result in spinel inclusions within the otherwise sphalerite QD lattice. Evidence for spinel inclusions is evidenced by the ${}^4A_{2g} \rightarrow {}^4T_{2g}$ ligand field transition in the optical data, high temperature Curie-Weiss behavior with an AFM coupling ($\theta \sim -125$ K) in the magnetic data, evidence of a tetragonal distortion at the Cr(III) center in the XANES data, and EPR data consistent with the oxidation state assignment. Based on analysis of the XANES data, the spinel inclusion forms as a dimer occupying an octahedral site generated by the loss of three Zn(II) ions opening two octahedral holes. A similar inclusion resulting in vacancy driven octahedral site formation was reported earlier for Eu(III) incorporation into CdSe, as verified by XANES and EXAFS analysis.⁸⁴ Etching experiments on the Cr:ZnSe QDs provide evidence of the presence of the spinel inclusions within the core of the QD and not the presence of two separate phases or surface segregation of the defect.

Due to the competition between kinetic and thermodynamics during QD growth, QDs often form non-thermodynamic structures due to surface effects,¹²¹ ion disorder,¹²² vacancy formation,^{52,84} and glide plane errors during growth without loss of the natural crystal habit.^{123,124} The potential for the QD to accommodate structural disorder suggest that unique structures might be able to be isolated using dopants capable of forming several oxidation states. The incorporation of Cr ions into ZnSe and other II-VI materials are a perfect example of a material in which different phases can be formed that have applications ranging from magnetic to optical applications.¹²⁵⁻¹²⁷ The observation can be understood by considering that the growth of a QD is

initiated by critical nucleation, wherein, the critical nuclei formed will reflect the stoichiometry and stability of the material.³¹ While in the bulk, the isolation of a single phase reflects the thermodynamics of the reaction, for a QD growth the kinetic phases are trapped.¹¹⁸

4.2 Experimental

Synthesis of Cr(III) doped ZnSe DMSQDs. The synthesis of Cr doped ZnSe QDs was performed under airless conditions using lyothermal methods based on the reaction of the single source precursor $\text{Li}_4[\text{Zn}_{10}\text{Se}_4(\text{SePh})_{16}]$ (Zn_{10}) cluster¹²⁸ with CrCl_2 in ~40 mL of hexadecylamine (HDA) at 220 °C under N_2 for 6 h, in analogy to early doping reactions.^{37,77} Isolation of the Cr:ZnSe QDs is achieved by addition of a minimal amount of toluene followed by dropwise addition of methanol to induce nanocrystal aggregation and precipitation. The precipitate is collected via centrifugation, re-dissolved in toluene and the process repeated 3 times to ensure reagent free particles. The samples are isolated and maintained under N_2 in a drybox to prevent formation of ZnO. Cr:ZnSe samples were prepared at 0% Cr, 0.4% Cr, 1.0%, 2.4% Cr, and 4.0% Cr based upon X-ray fluorescence (XRF) analysis by carrying out the reactions at 0 % Cr, 2 % Cr, 5 1% Cr, 10 % Cr, and 20 mol% Cr to Zn in the reaction.

The Cr, Zn and Se content were determined by using an Oxford Instruments ED₂₀₀₀ X-ray fluorescence (XRF) spectrometer with a Cu- K_α source. For a standard XRF measurement, the powdered samples were completely dissolved in 90 % HNO_3 , heated to remove excess NO_x , and then diluted to ~3 mL with a 2% HNO_3 solution to allow compatibility with the XRF sample holder.

QD Characterization. The isolated Cr:ZnSe QD size, dispersity, morphology, and structure were analyzed by transmission electron microscopy (TEM) and TEM-selected area electron diffraction (TEM-SAED) using a JEOL-2010 microscope operated at 200 kV. The size

dispersity is analyzed over 100 QDs. The SAED map for the QDs was assigned to lattice planes based upon the observed d-spacing. The QDs were dispersed on holey carbon (400 mesh) from a toluene solution.

The size of the QD measured by TEM is verified by analysis of the first exciton transition ($1S_{3/2} \rightarrow 1S_e$) for ZnSe in the optical absorption spectroscopy by analyzing the first exciton.¹²⁸ The room temperature optical absorption spectra were measured on toluene solutions of the Cr:ZnSe QDs at $\sim 10^{-6}$ M concentrations in a 1-cm quartz cuvette using a Varian Cary 50 UV-Vis spectrophotometer.

Ensemble structural characterization of the isolated QDs is performed using a powder X-ray (pXRD) diffractometer. The pXRD patterns were recorded on about 10 mg samples on a Rigaku DMAX 300 Ultima III Powder X-ray diffractometer using Cu K_α ($\lambda = 1.5418 \text{ \AA}$). QD sizing by Scherer analysis of the (110), (220), and (311) reflection in pXRD provides validation of the optical and TEM size analysis, and more importantly provides further support for the high crystallinity of the samples.

High frequency electron paramagnetic resonance (HF-EPR) measurements between 100–406.4 GHz at 10 K were measured for the 2.5% Cr:ZnSe QD. The HF-EPR measurements were conducted at the Florida State University National High Magnetic Field Laboratory (FSU-NHMFL) in Tallahassee, FL. The HF-EPR operates in transmission mode and employs oversized cylindrical waveguides. Microwave detection was performed with a low-noise, fast-response InSb hot-electron bolometer (QMC Ltd.). For the EPR experiments, all samples were analyzed as powdered samples.

Assignment of the Cr Oxidation State and Site-Symmetry. Assignment of the oxidation state to Cr(III) and the site of occupation (distorted O_h) for the Cr ion in the ZnSe QD is accomplished by analysis for the Cr $L_{2,3}$ line by soft X-ray absorption Near Edge (XANES)

spectroscopy between 570 to 600 eV for the 2.5% Cr:ZnSe. Crystal field absorption spectroscopy on all doping concentrations confirms the assignment of Cr(III) in a distorted octahedral site. XANES measurements were acquired at the spherical grating monochromator beamline at the Canadian Light Source at the University of Saskatchewan. The QD samples were dissolved in toluene, allowed to slowly evaporate on a Si wafer, mounted onto carbon tape, and introduced into an ultra-high vacuum chamber ($P \sim \text{low } 10^{-8} \text{ to low } 10^{-9} \text{ Torr}$). XANES experiments were conducted using the total electron yield method where the total photocurrent into the sample is measured as the photon energy is scanned through the absorption edge. The current from a highly transmissive gold grid was used to normalize the XANES spectra. Crystal field absorption spectra of solution samples by UV-Vis on all doping concentrations confirm Cr oxidation state and site symmetry.

Magnetic Characterization. The magnetic properties of the 2.5% Cr:ZnSe QDs were measured on powdered samples using a Quantum Design MPMS XL7 superconducting quantum interference device magnetometer (SQUID). Zero-field cooled (ZFC) and field cooled (FC, 0.02T) susceptibility measurements were collected for dc-susceptibility over the range of 2 to 300 K. Field dependent magnetization (M) was measured between -7 to $+7$ T.

4.3 Results and discussion

Preparation of the Cr:ZnSe QD from the single source precursor leads to formation of spherical 2.8 ± 0.1 nm Cr:ZnSe QD with $\sim 5\%$ size dispersity based on TEM analysis (Figure 4.1). The Cr doping of the ZnSe is experimentally measured by XRF yielding values of Cr incorporation at 0%, 0.4%, 1.0%, 2.5%, and 4.0% in the ZnSe QDs.

Ion incorporation at concentration lower than the reaction mole ratio is common for doping in QDs reflecting the difficult in precursor activity and ion inclusion rate to the growing

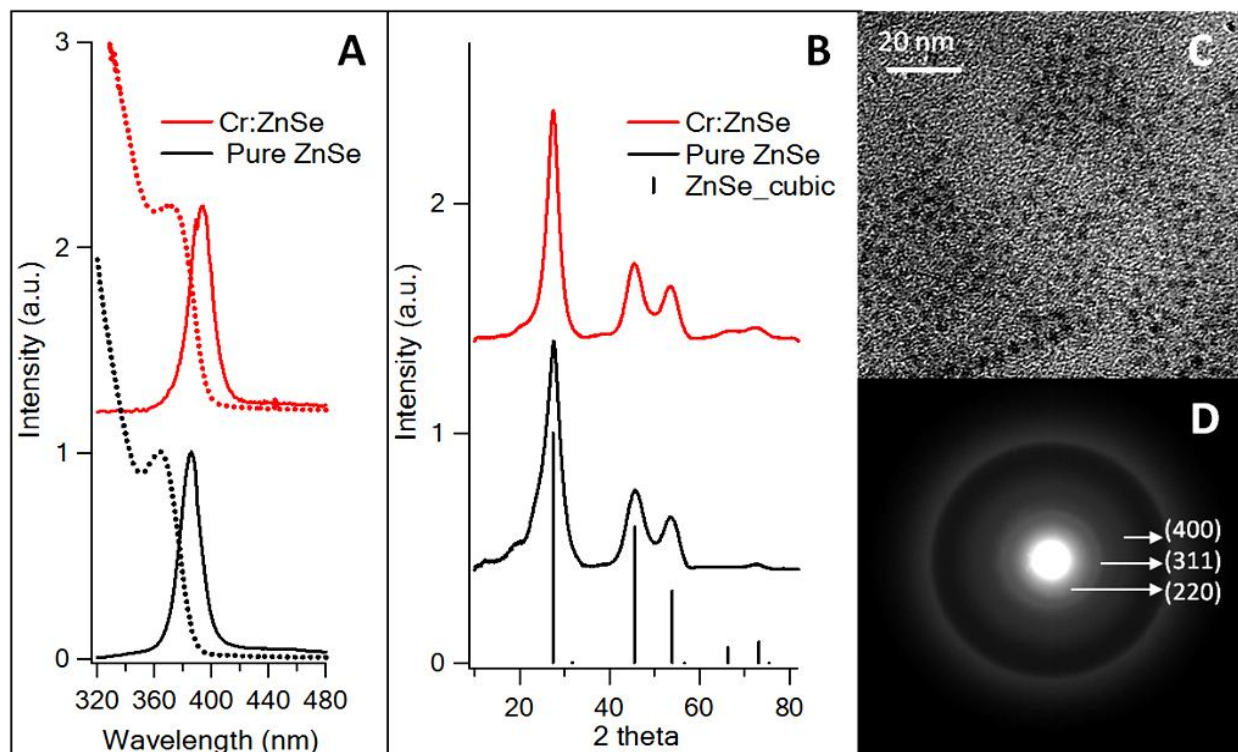


Figure 4. 1. Characterization data A) absorption (dashed) and photoluminescence (solid) spectra for ZnSe and Cr:ZnSe QDs, B) pXRD patterns for ZnSe and Cr:ZnSe QDs, C) TEM image for Cr:ZnSe QD, and D) TEM electron diffraction image for Cr:ZnSe QDs.

QDs. The Cr ion occupies a T_d site by substitution of the Zn (II) ion or can occupy an O_h hole via Cd vacancy formation. Such vacancy formation in CdSe QDs has been reported for Eu(III) and Cu(I) inclusions.^{52,84} Incorporation of Cr(II) is substitutional with no vacancy formation, Cr(I) requires formation of Se vacancies, while formation of the Cr(III) ion requires Zn vacancy formation in a 2 Cr to 3 Zn ratio. The mole ratio of cation to anion is approximately constant across the doping concentrations (Table 4.1) reflecting the experimental uncertainty at the low Cr concentrations for estimating lattice vacancy formation. Unfortunately, XRF cannot distinguish within experimental error the vacancy population.

The pXRD data for Cr:ZnSe QDs is shown in Figure 4.1b and can be indexed to the sphalerite (zinc-blende) F-43m structure with reflections observed at 27.4 °, 45.5 °, and 53.9 °. No pXRD reflections are identified for Cr_2Se_3 or $ZnCr_2Se_4$ phases (Figure 4.2). The assignment of the zinc-blende phase is confirmed by inspection of the d-spacing for the (220), (331), and (400) reflections in the TEM-SAED pattern (Figure 4.1D). Using pXRD the TEM size can be confirmed by Scherrer analysis based on the width of the (111), (220), and (311) diffractions. The observation that the Scherrer broadening approximated of size is in good agreement with the TEM suggests the QDs are highly crystalline.

The optical absorption data (Figure 4.1A and Figure 4.3) for the QD samples exhibit well-defined excitonic features for the 2.5% Cr:ZnSe QDs at 374 nm (3.32 eV). The energy of the first absorption feature position corresponding to the $1S_{3/2} \rightarrow 1S_e$ is consistent with the measured TEM QD size.¹²⁸ The photoluminescence data shown in Figure 4.1A arises from bandgap recombination, exhibiting no distinguishable Cr based PL at RT between 300 nm and 700 nm (Figure 4.3).

The Cr $L_{2,3}$ edge XANES data in Figure 4.4, for the 2.5% Cr:ZnSe sample shows two features, a broad absorption feature at ~578 eV with a shoulder to higher energy (L_3 edge), and a

Table 4.1. The cation/anion mole ratio of Cr:ZnSe QDs

% Cr:ZnSe	Cation/Anion
0	1.34
0.4	1.21
1.0	1.23
2.5	1.23
4.0	1.23

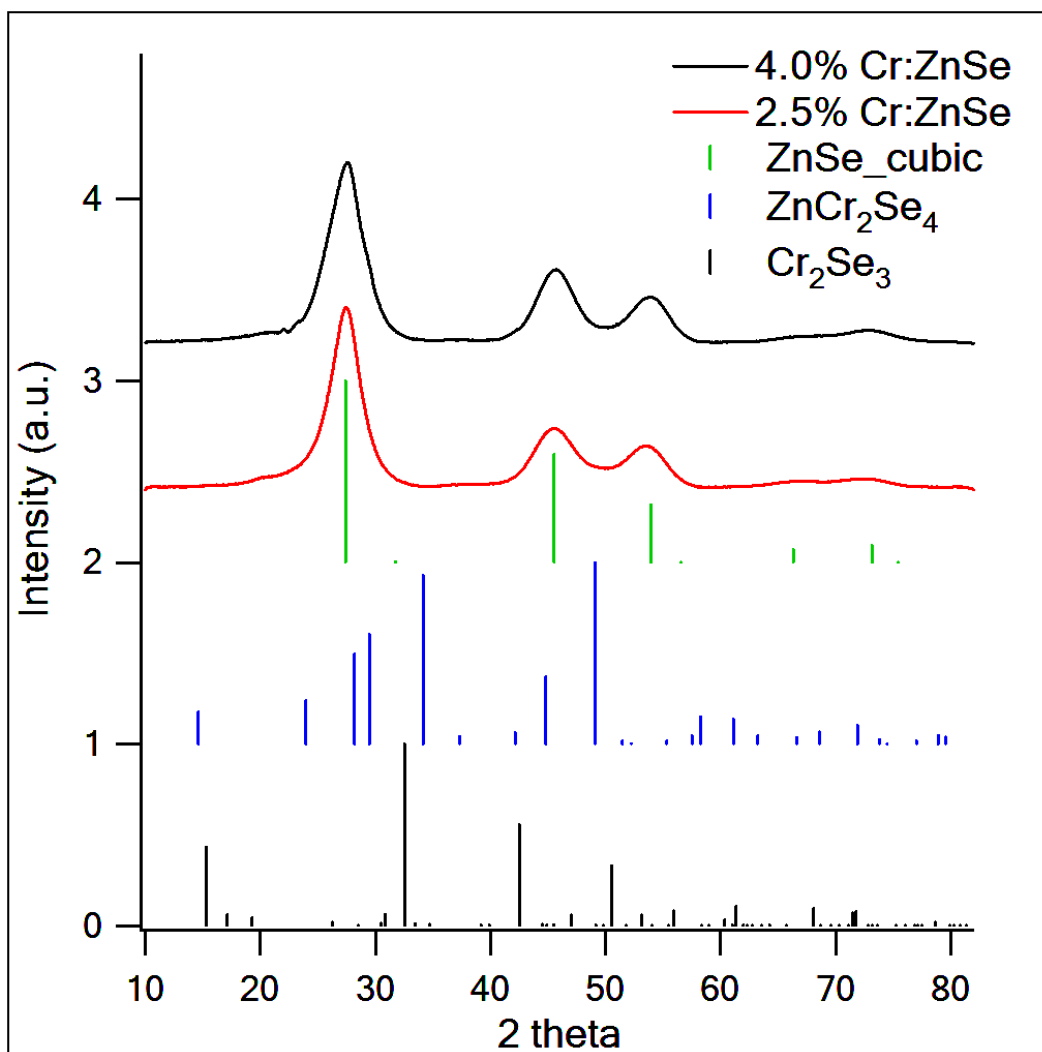


Figure 4. 2. The pXRD data for 2.5% and 4.0 % Cr:ZnSe QDs.

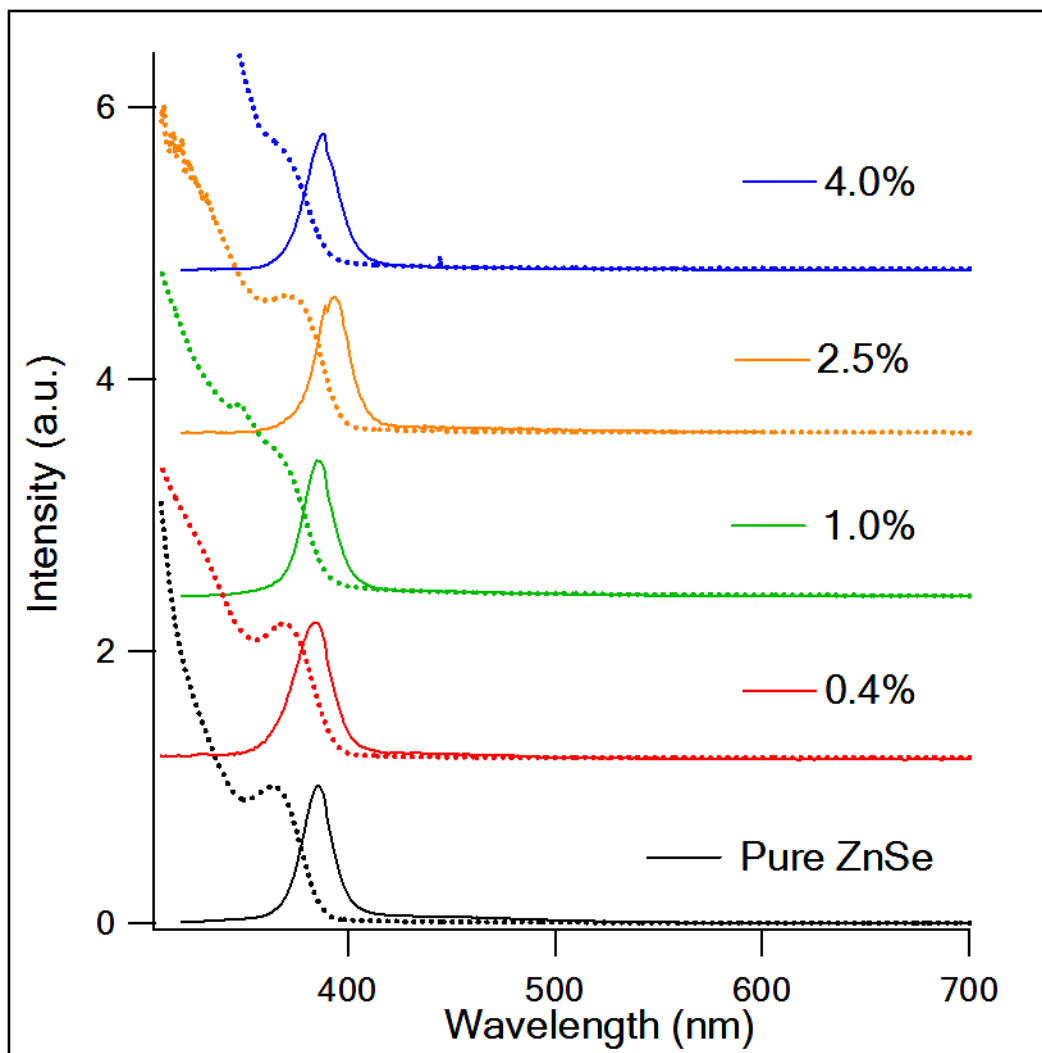


Figure 4. 3. Absorption (dashed) and photoluminescence (solid) spectra for 0%, 0.4%, 1.0%, 2.5%, 4.0% Cr:ZnSe QDs.

weaker split feature at ~586 eV (L_2 edge). From the XANES data, the Cr oxidation state in the Cr:ZnSe QD can be assigned to Cr(III) based upon comparison of the energy for the measured Cr $L_{2,3}$ edge data in spectra for Cr(II), Cr(III), and Cr(IV) occupying a perfect O_h field with a crystal field energy of $10Dq \sim 2.07$ eV. The XANES data for the 2.5% Cr:ZnSe QD requires incorporation of a tetragonal distortion of the O_h field ($10Dq = 2.07$ eV) about the Cr center to properly fit the XANES pattern. The tetragonal distortion effectively broadens the L_2 edge. The crystal field terms for that distortion, which include the terms D_s and D_t , suggest compression along the z-axis. The spectra are in good agreement with previously reported XANES Cr standards and a XANES study of $CdCr_2Se_4$.¹²⁹

The assignment of the Cr(III) oxidation state occupying an O_h site with a crystal field of ~ 2 eV can be confirmed by inspection of the crystal field optical absorption in Figure 4.5. The absorption data reveal a broad, split absorption feature centered at 595 nm. The concentration dependent feature can be assigned to a ${}^4A_{2g} \rightarrow {}^4T_{2g}$ ligand field transition for Cr(III).¹³⁰ The higher lying crystal field transitions for Cr(III) at ~ 440 nm are obscured due to overlap with the 1st exciton transition in the ZnSe QD. The energy of the ${}^4A_{2g} \rightarrow {}^4T_{2g}$ ligand field transition in Cr(III) is equivalent to the crystal field energy, allowing a value of $10Dq = 2.07$ eV to be extracted from the optical measurement (Figure 4.5). The value of $10Dq$ is consistent with the XANES data. Comparison to the crystal field value for a $ZnCr_2Se_4$ spinel supports the suggestion of an inclusion in the crystal lattice.^{131,132} The splitting of the ${}^4A_{2g} \rightarrow {}^4T_{2g}$ ligand field transition in the absorption spectrum in Figure 4.5 is consistent with the symmetry breaking of a pure O_h site due to the tetragonal distortion of the Cr(III) center observed in the XANES data.

The XANES and optical data for the Cr:ZnSe QDs supports a model wherein a Cr(III) ion incorporation occurs by occupying an O_h hole generated by Zn vacancy formation. Since the structural data strongly implies a high degree of crystallinity, it is believed the vacancy generates

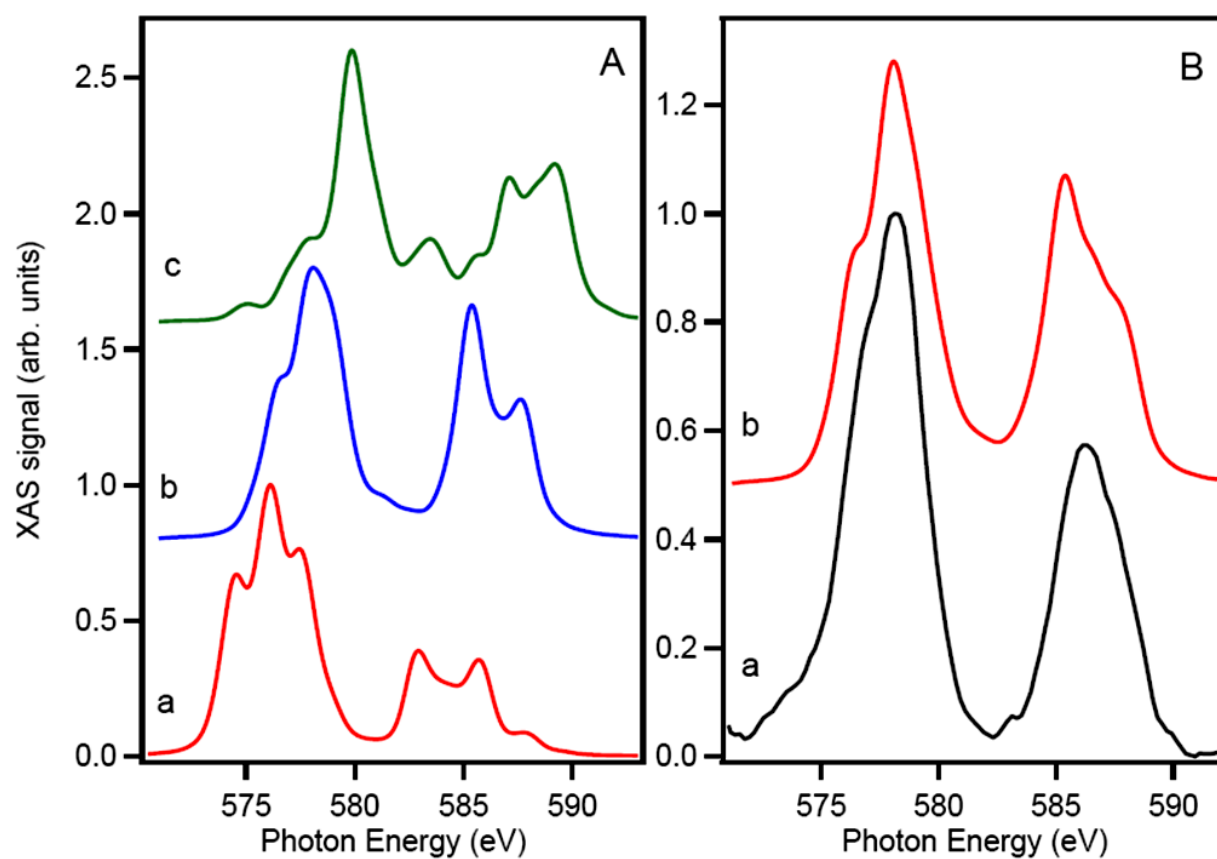


Figure 4. 4. Cr L_{2,3} edge X-ray absorption spectra. A) simulation of (a) Cr(II), (b)Cr(III), and (c) Cr(IV) in a perfect Oh field (10 Dq = 2.07 eV). B) (a) Cr:ZnSe QDs and (b) simulated distorted O_h crystal field for Cr(III).

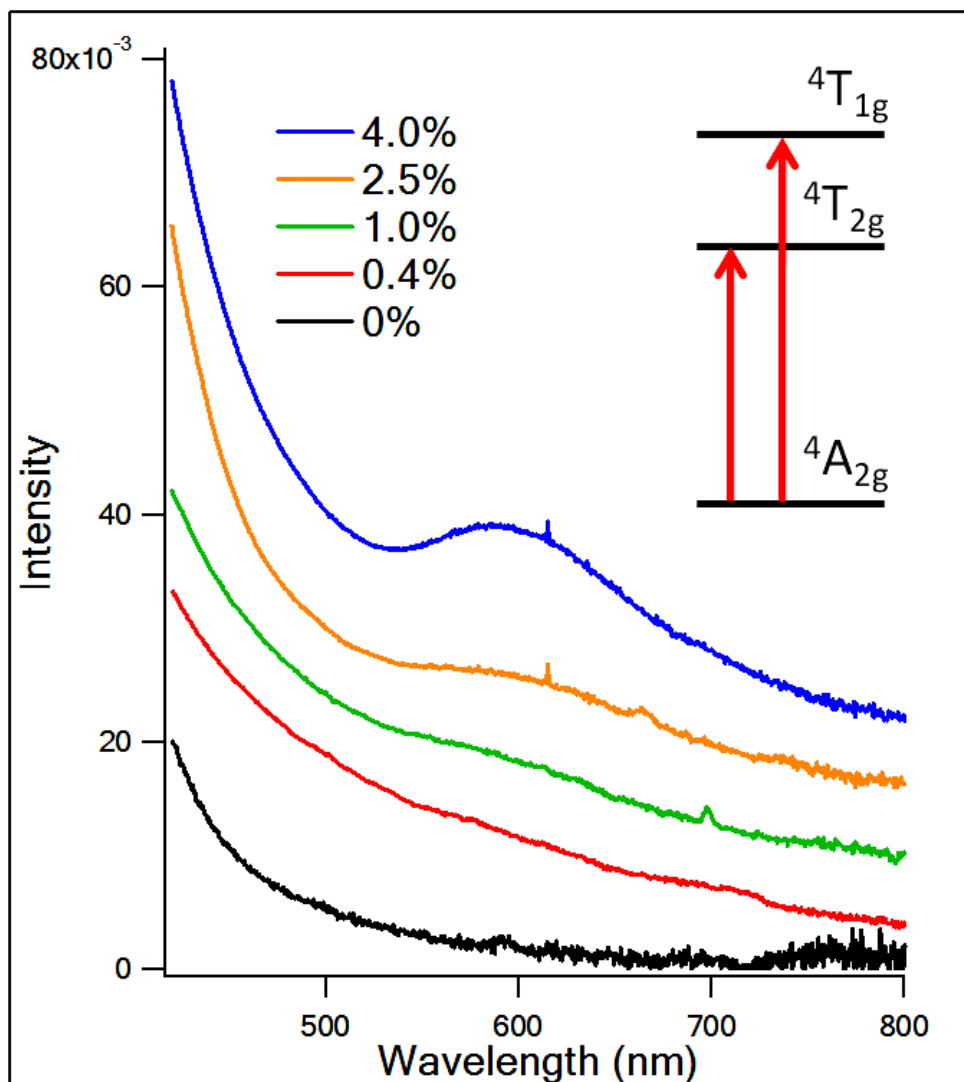


Figure 4. 5. Absorption spectra in concentrated toluene solution for 0%, 0.4%, 1.0%, 2.5%, 4.0% Cr:ZnSe QDs. Insert is the energy level of Cr(III) ion in a O_h crystal field.

a Cr(III) dimer in the lattice to minimize lattice distortion. A similar suggestion was made previously for Eu(III) incorporation onto vacancy driven octahedral holes in a CdSe QD.⁸⁴ The formation of a dimer is surprising as doping at 2.5% should form localized single Cr(III) sites with a 73% probability, and dimer formation at 19%. However, defect clustering within a QD is a common observation, and may play a role in the Cr:ZnSe QDs to pin the strain induced by the defect.

EPR confirmation of Cr(III) assignment. Further confirmation of the Cr(III) (d^3 , $S = 3/2$) assignment is available by measuring the high frequency EPR data. For Cr(III) in the octahedral crystal field, the 4A_2 orbital singlet is responsible for the observed EPR absorption. The EPR spectrum of the isotopes of Cr(III) without nuclear spin can be described by the Zeeman term and the spectrum will consist of a single peak with a g-value of 1.9808.¹³³ The deviation of the g-value from the spin only value of $g_e = 2.0023$ is caused by a contribution from triplet T_2 to the orbital moment of the ground state. Hyperfine contributions will not be observed in the powder spectra since the ^{53}Cr isotope is only 9.55% abundant each hyperfine structure line has an intensity of approximately 1/42 of that of the main peak.¹³⁴

The frequency dependent EPR spectra for the 2.8 nm Cr(2.5%):ZnSe sample measured at 100, 112, 200, 216, 304.8, 324, and 406.4 GHz (10 K) are shown in Figure 4.6. An accurate value of g for the Cr(III) center can be obtained by plotting the frequency dependence of the center field (Figure 4.6B). The plot yields a g-value of 1.9808 consistent with the prediction for Cr(III) ion in an O_h field and reported values for Cr(III) ions in a spinel lattice.¹³⁵ The observed EPR pattern can not be assigned to Cr(II) or Cr(I).^{105,133}

Evidence of core vs. surface occupation of Cr(III). The incorporation of Cr(III) could occur within the core or be isolated at the surface via QD self-healing. Evidence for core doped Cr(III) ions can be obtained by inspection of the EPR spectrum for the Cr(III) centers in Cr:ZnSe

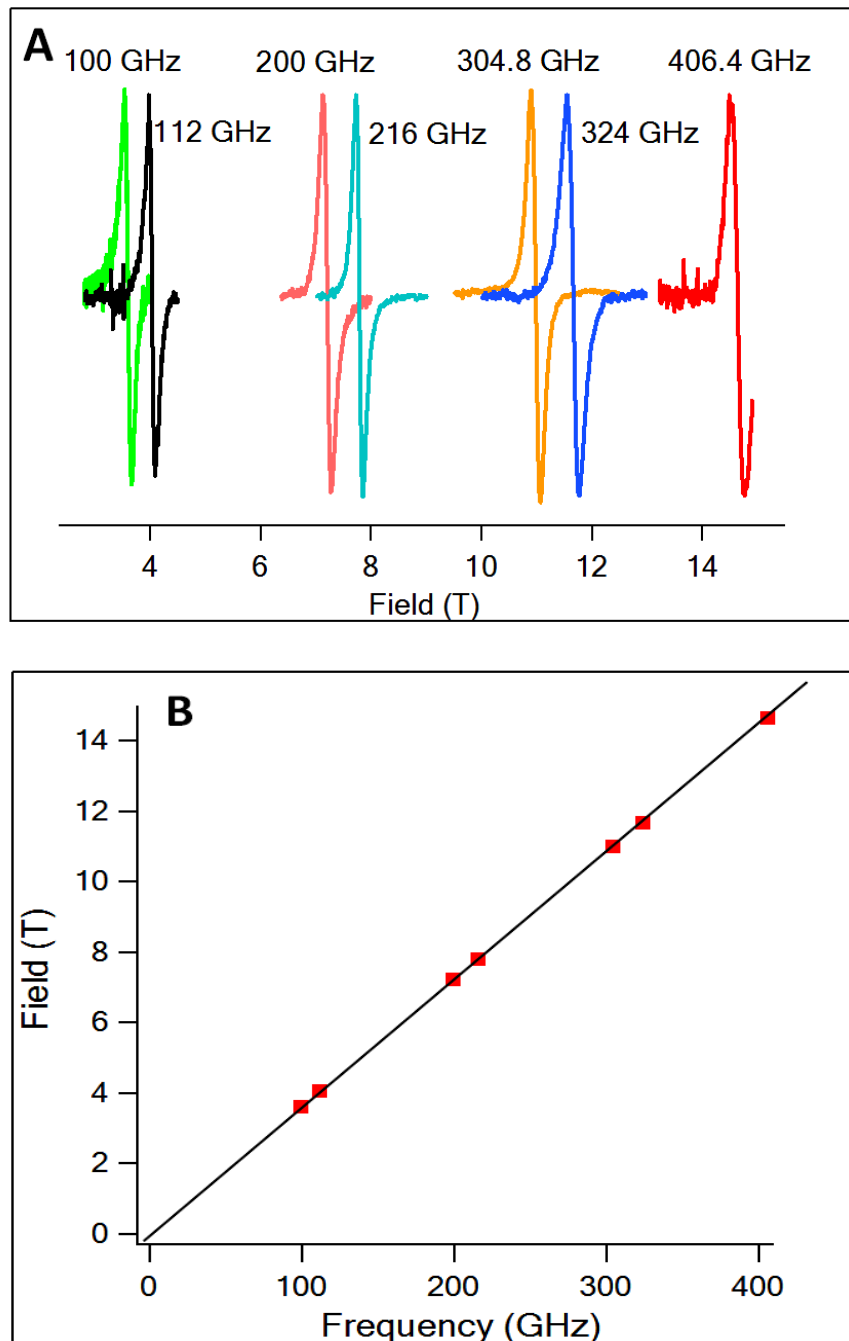


Figure 4. 6. A) Frequency dependent EPR measurements at 10 K for Cr:ZnSe QD, B) Frequency dependent of EPR central resonance field of 2.4% Cr(III):ZnSe QD which can fit to $g = 1.9808$ for Cr(III) ion.

following chemically etching of ~2 layer of the QDs. Surface etching is carried out using 20 μL $\text{H}_3\text{PO}_4\text{:HCl}$ (1:1 V:V) in 1 mL saturated toluene solution. The QD samples were etched for 2 seconds at room temperature. The etched samples were precipitated by the addition of MeOH, re-dissolved in toluene and re-precipitated by MeOH prior to conducting the EPR experiments. As observed in Figure 4.7 the Cr(III) EPR spectra is identical (shape and g-value) to the QDs prior to etching indicating the Cr(III) ions occupy core sites within the ZnSe QDs.

The results support a model wherein the Cr(III) spinel inclusions do not result in phase segregation due to self-healing in the QDs. Furthermore, the lack of a change in the EPR change in the EPR parameter in the 2.8 nm Cr:ZnSe QDs suggest the Cr spinel phase may act as the nucleus for QD growth since a 2.8 nm QD only consists ~10 monolayers of Zn-Se. If ~2 monolayer are etched uniformly during acid etching the presence of Cr(III) sites in the EPR suggest the Cr spinel phase is near the size of nuclei (~2 nm)^{31,51} for QD nucleation and growth.

Magnetic Properties of Cr:ZnSe. The magnetic properties of the 2.5% Cr:ZnSe QDs is shown in Figure 4.8A for the zero-field-cooled (ZFC) and field-cooled (FC, 200 Oe) susceptibility (χ) data. The insert shows the Currie-Weiss (C-W) law plot of the temperature dependent data, $1/\chi = (T - \theta) * C^{-1}$ (C is the Currie constant, T is temperature in Kelvin, and θ is the Curie-Weiss temperature). The experimental susceptibility and magnetization data for the Cr:ZnSe QDs exhibits the predicted paramagnetic (PM) behavior of the diluted magnetic QDs, and is consistent with the helical spin state observed in bulk ZnCr_2Se_4 .¹¹²

The field dependent magnetization (M) plot for 2.5% Cr:ZnSe is shown in Figure 4.8B. The magnetization data exhibits no hysteresis with a saturation value (M_{SAT}) for the sample above 2 T. The absence of ferromagnetic (FM) order in the 2.5% Cr:ZnSe QDs can be verified by plotting the field dependent data as an Arrott plot in Figure 4.8C (M^2 vs H/M at fixed temperatures T). In the Arrott plot, the Curie temperature (T_C) for ferromagnetism is determined

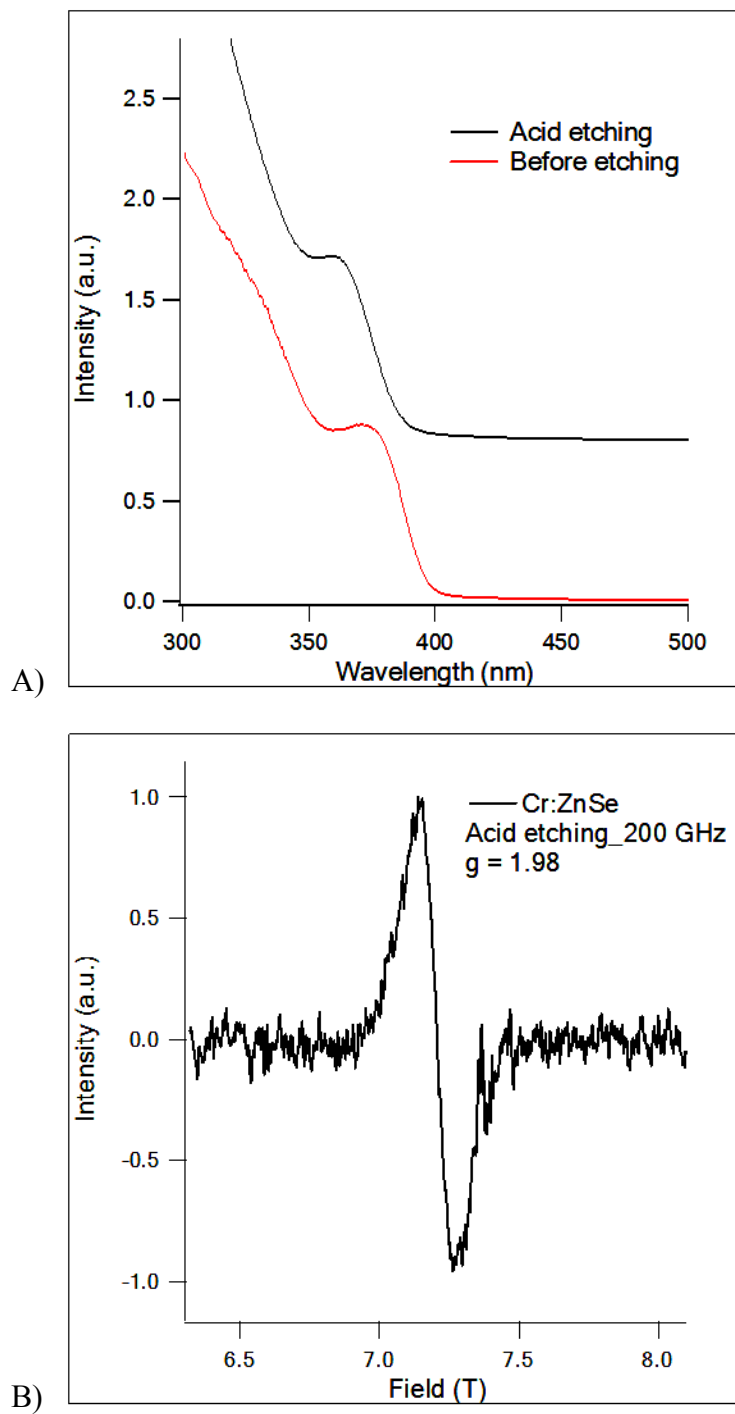


Figure 4. 7. A) Absorption spectra before and after acid etching for the Cr:ZnSe QDs, and B) 200 GHz EPR of Cr:ZnSe QDs after acid etching.

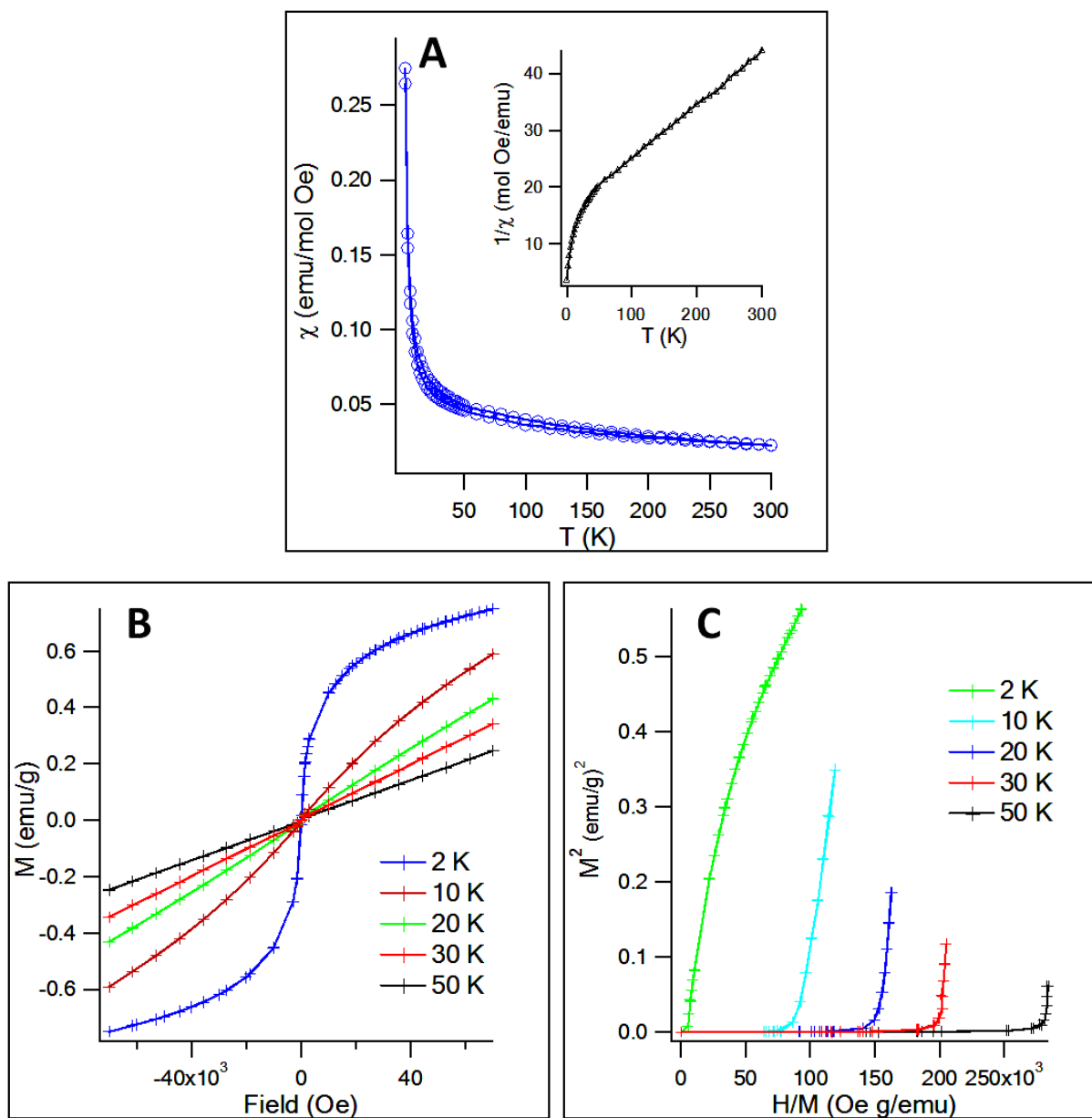


Figure 4. 8. A) Temperature dependent ZFC and FC (200 Oe) susceptibility data. The insert is the Curie-Weiss law plot showing negative Curie-Weiss temperature (-125 K), B) Field dependent magnetization (M) plots at 2, 10, 20, 30, 50 K, and C) Arrott plots (M^2 vs. H/M) for the Cr(2.5%):ZnSe QDs.

from the temperature where M^2 intercepts with the origin.¹³⁶ The Arrott plots shows a linear H/M-dependence from 10–50 K. Consistent with a PM material, the Arrott-plot approaches 0 indicating paramagnetic (PM) behavior of the QDs in the whole experimental temperature range. The data at 2 K exhibits curvature which can be understood in analogy to the Arrott-plot in bulk materials where competing magnetic exchange at low temperature exists.¹³⁷ The competing magnetic behavior may arise from the spinel inclusions within the QD lattice.

For a bulk ZnCr_2Se_4 spinel, the theoretical estimated direct exchange constant in spinel (–15.1 K),¹¹⁶ even though the long range superexchange must be considered for the overall helical spin state as the result of competing ferromagnetic (FM) and antiferromagnetic (AFM) interactions. Bulk ZnCr_2Se_4 at low temperature is antiferromagnet in spite of the fact that the Curie-Weiss temperature θ is +115 K which implies FM exchange.^{115,138} A helical magnetic structure is required to explain the positive Curie-Weiss temperature.¹³⁸ For the Cr:ZnSe QDs, the magnetic data exhibit high temperature paramagnetic (PM) behavior with a negative Currie temperature indicative of AFM exchange (θ of –125 K). The negative deviation in the C-W plot for the low-T susceptibility data can be interpreted in term of short range AFM interactions arising between the Cr(III) ions in a ZnCr_2Se_4 spinel inclusion. Assuming a spinel inclusion the exchange constant, J_{NN}/k , can be calculated from the equation $J_{\text{NN}}/k = 3\theta/2ZS(S + 1)$, where S is the spin and Z is the number of nearest neighbors.^{24,30} The calculated value of J_{NN} is –12.5 K for Cr:ZnSe QDs, which is close to the theoretical direct exchange constant in ZnCr_2Se_4 . The agreement in the J_{NN} value supports formation of a Cr(III)-Cr(III) dimer in the ZnSe lattice where the short range Cr(III)-Cr(III) interaction dominate the magnetic properties (Figure 4.9). In Figure 4.9, three Zn(II) T_d sites was removed to add two Cr(III) O_h sites, which illustrates the incorporation of the ZnCr_2Se_4 spinel structure in the ZnSe lattice.

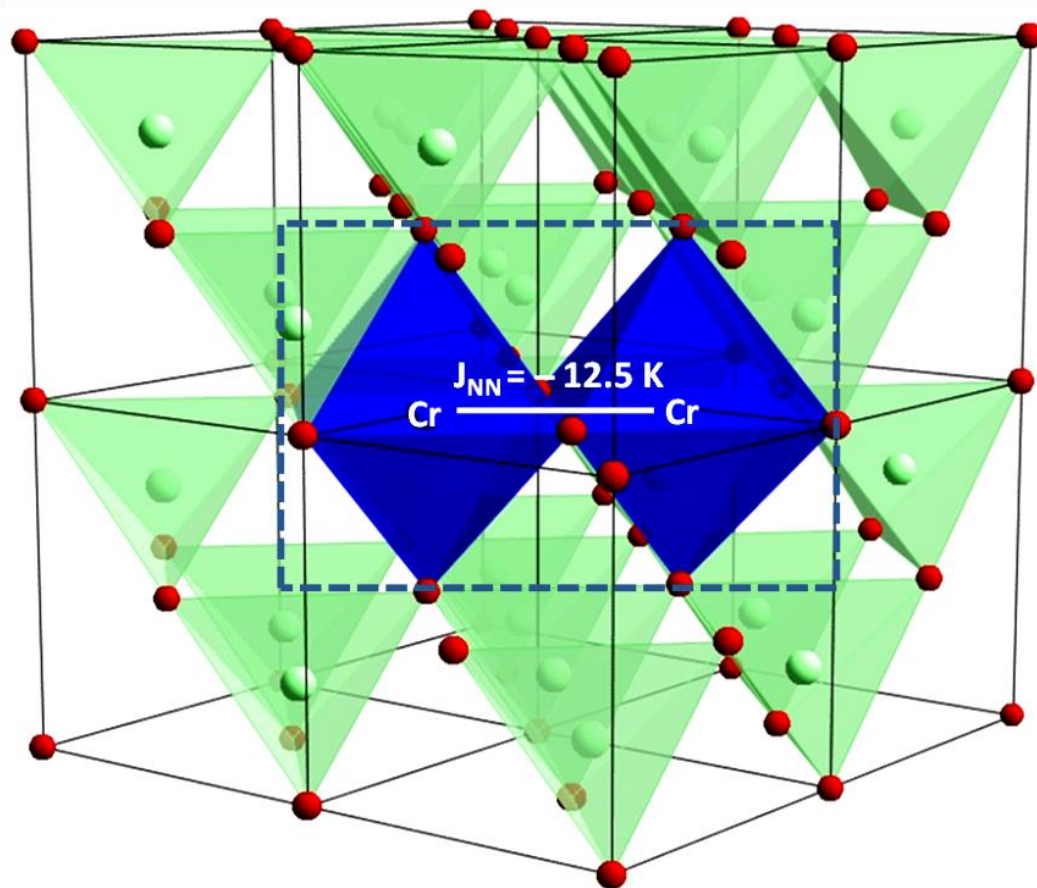


Figure 4. 9. Illustration of part of the ZnCr₂Se₄ spinel structure in the ZnSe lattice. The Cr(III) ions (blue balls) occupy O_h sites and Zn(II) ions (green balls) occupy T_d sites. Three Zn(II) T_d sites was removed to add two Cr(III) O_h sites.

4.4 Conclusion

The formation of ZnCr_2Se_4 spinel phase in Cr doped ZnSe QDs have been prepared from a single source precursor method. The Cr $L_{2,3}$ edge spectra in XANES measurement can be assigned as a Cr(III) in a distorted O_h crystal field in ZnCr_2Se_4 . The absorption spectra for the Cr:ZnSe QDs confirms the oxidation state assigned and allows the crystal field energy be calculated ($10 Dq = 2.07$ eV) from the ${}^4A_{2g} \rightarrow {}^4T_{2g}$ crystal field transition. ZFC/FC susceptibility measurement shows paramagnetic (PM) behavior of the QDs with AFM coupling at low temperature. A Curie-Weiss law plot indicates the AFM coupling at low temperature can be understood by short range AFM exchange between Cr(III) in the presence of ZnCr_2Se_4 phase. Calculation of the Cr-Cr J_{NN} value for the QD yields a value of -12.5 K, which is consisted with the reported J_{NN} for Cr-Cr nearest-neighbor interaction in bulk ZnCr_2Se_4 . The formation of the ZnCr_2Se_4 phase may suggest unique stabilities can be obtained due to the growth mechanism trapping kinetic structures or the nature of critical domain formation in the QD growth.

CHAPTER FIVE

CONCLUSIONS AND FUTURE DIRECTIONS

The size- and site-dependent magnetic properties for Mn(II) doped CdSe QDs were studied in this work. The goal of this chapter is to address some interesting directions in the field of magnetic properties for doped II-VI semiconductor QDs.

5.1 Future directions

Concentration dependent magnetic properties of Mn:CdSe QDs.

As was mentioned in Chapter 2, the study of the size dependent magnetic properties of Mn:CdSe QDs demonstrates that the carriers mediate the Mn(II)-Mn(II) ferromagnetic interaction by the RKKY model, leading to the superparamagnetic (SPM) behavior of the small QDs. The concentration in the study was maintained at 0.6% to ensure that the sample is below the percolation threshold for Mn:CdSe. However, a study of the concentration dependent magnetic properties in Mn(II) doped CdSe QDs would allow both size and concentration to be systematically varied and fit by the RKKY model.

The preliminary experimental data of the 1% doped Mn:CdSe QDs exhibits a size dependent trend similar to the 0.6% Mn:CdSe QDs, which display a decrease in coercivity with an increase in the QD size, as well as an increase in the carrier concentration with size (Figure 5.1). In addition, with increasing concentration a shift in blocking temperature (T_B) from 12 K (0.6% Mn:CdSe) to 32 K (1.0% Mn:CdSe) is observed for ~3 nm Mn:CdSe QDs, which is consistent with the effective decrease in Mn-Mn separation leading to enhanced RKKY coupling.

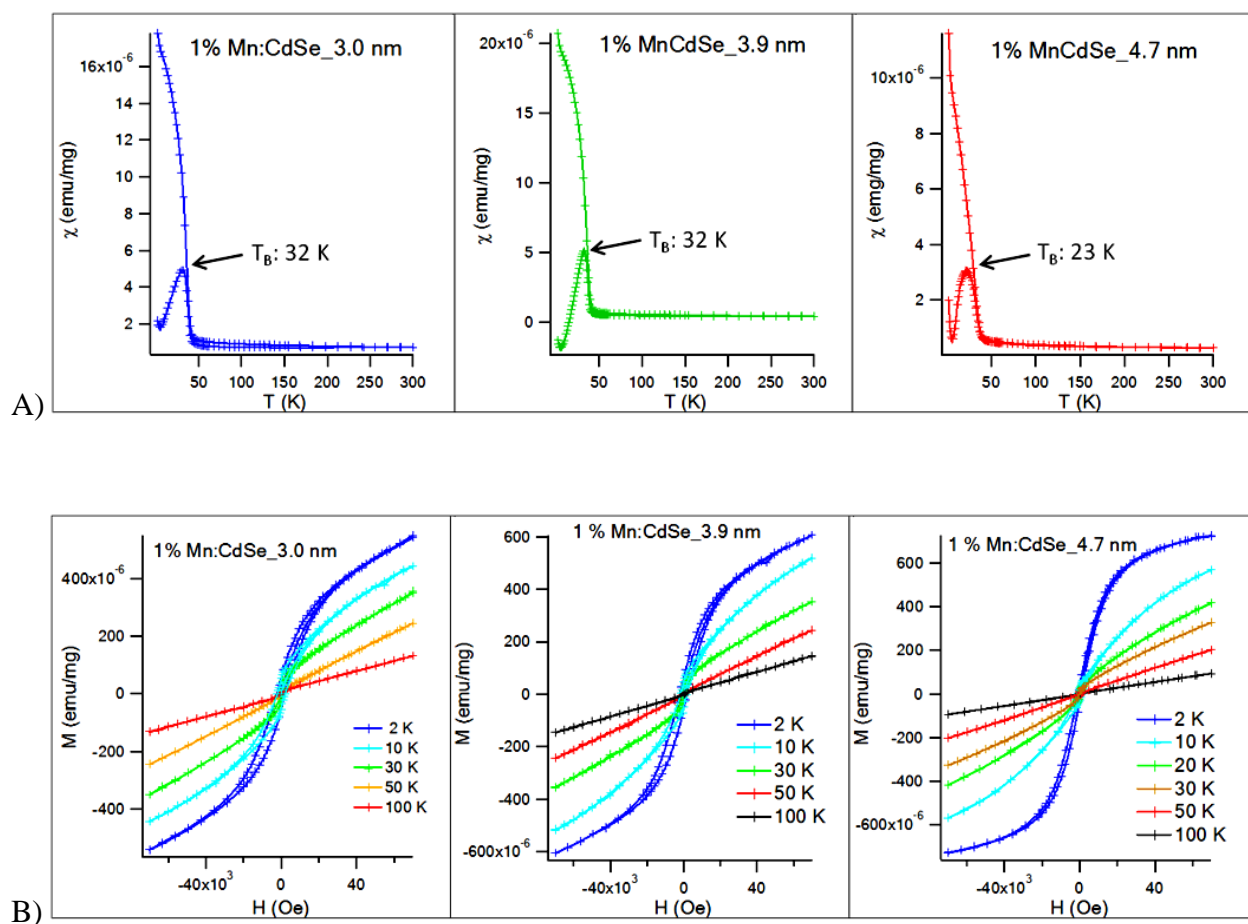


Figure 5. 1. A). Temperature dependent ZFC and FC (100 Oe) susceptibility data for 3.0 nm, 3.9 nm and 4.7 nm 1% Mn:CdSe QDs. Blocking temperature (T_B) is indicated in the plots. B). Magnetization plots for 3.0 nm, 3.9 nm and 4.7 nm 1% Mn:CdSe QDs. The coercive field decreases as the size of the DQs increases which is the same trend found in 0.6% Mn:CdSe QDs.

Surface ligand exchange.

The high frequency EPR experiments confirm that the QD micro-environment can be divided into a surface and core site. The difference in A and g values for the two sites reflect the difference in the crystal field experienced by the Mn(II) ion at their respective sites. As shown in chapter 3, the surface ligand back-bonding strength can have a dramatic effect on the surface state energies in CdSe QDs and can perturb the observed hyperfine exchange for surface Mn(II) ions. For the ligand exchanged samples, the hyperfine constant (A) for surface site shifts for the ligand series with values of 91.3 G (DDN), 91.2 (TOP), 91.1 (TOP-Se), 90.9 (DDA), 90.5 (py). The increase in A-value across the ligand series tracks the increased π -acceptor strength for the ligand. Analysis of the effects of ligation on the core and surface of a QD provides a better model for how a QD reconstructs as a function of size following ligand passivation.

The surface induced carriers, which are believed to arise from charge transfer effects associated with the ligation layer, must be weakly localized or delocalized in order to result in the long-range RKKY exchange coupling. The participation of carrier mediated exchange would explain the decreased magnetic saturation value observed for the smallest QDs. Similar behavior has been reported for ligand induced carrier mediated exchange in Mn(II) doped ZnO QDs. Further studies investigating the ligand dependent influence on the magnetic susceptibility is underway to deduce the importance of ligand passivation on the observed magnetic properties.

Core/shell QDs.

As anticipated, the Mn(II) local environment depends upon the site of Mn(II) doping, primarily whether it is inside a QD or near the passivant shell. The results are consistent with an earlier report that Mn(II) doped into a shell of a core-shell QD experiences different chemical environments, as the Mn(II) center is moved away from the core QD towards the passivant shell. It would be very interesting to coat the stochastically doped Mn:CdSe QDs with ZnS shell and

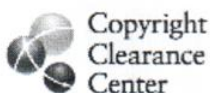
monitor the change of surface Mn signal using EPR spectra. The core/shell work unfortunately fell by the wayside, as we found that the ZnS shell was grown in a tetrapod which was not expected. Regarding the shelling Mn:CdSe QDs with other semiconductor lattice such as ZnS, one would anticipate a stronger core EPR signal as the result of despairing of surface Mn(II) site. However, a new set of hyperfine splitting was observed in EPR, which should arise from the interface between CdSe and ZnS lattice. The CdSe shelling for Mn:CdSe would be an ideal for the site occupation research since no lattice mismatch arise from the CdSe shell, however no successful CdSe shell was grown in my research thus far, so this might be a good project for a future graduate student interested in this work.

5.2 Conclusions

This dissertation studies the size- and site-dependent optical and magnetic properties of II-VI quantum dots (QDs). We have found that the carriers inside the small QDs can mediate the Mn(II)-Mn(II) ferromagnetic interaction by the RKKY model, which helps explain reasons for the observation of a superparamagnetism (SPM) in small Mn:CdSe QDs. Using high frequency EPR, the possible dopant sites in Mn:CdSe lattice can be identified as the surface and core position of Mn:CdSe QDs. The studies of concentration and ligand dependent magnetic properties of the Mn:CdSe QDs and core/shell QDs are very interesting and underway. This research opens the door to the combination of magnetic transition metals and surface carriers in II-VI QDs branches into a platform for future breakthroughs in optical or magnetic properties of diluted magnetic semiconductor QDs.

APPENDIX A

PERMISSION AND COPYRIGHT



RightsLink®

Home

Account Info

Help



ACS Publications
High quality High impact.

Title: Involvement of Carriers in the Size-Dependent Magnetic Exchange for Mn: CdSe Quantum Dots

Logged in as:
Weiwei Zheng

LOGOUT

Author: Weiwei Zheng et al.

Publication: Journal of the American Chemical Society

Publisher: American Chemical Society

Date: May 1, 2011

Copyright © 2011, American Chemical Society

PERMISSION/LICENSE IS GRANTED FOR YOUR ORDER AT NO CHARGE

This type of permission/license, instead of the standard Terms & Conditions, is sent to you because no fee is being charged for your order. Please note the following:

- Permission is granted for your request in both print and electronic formats.
- If figures and/or tables were requested, they may be adapted or used in part.
- Please print this page for your records and send a copy of it to your publisher/graduate school.
- Appropriate credit for the requested material should be given as follows: "Reprinted (adapted) with permission from (COMPLETE REFERENCE CITATION). Copyright (YEAR) American Chemical Society." Insert appropriate information in place of the capitalized words.
- One-time permission is granted only for the use specified in your request. No additional uses are granted (such as derivative works or other editions). For any other uses, please submit a new request.

BACK

CLOSE WINDOW

Copyright © 2011 Copyright Clearance Center, Inc. All Rights Reserved. [Privacy statement](#).
Comments? We would like to hear from you. E-mail us at customercare@copyright.com



RightsLink®

[Home](#) [Account Info](#) [Help](#)



ACS Publications

Title: Probing the Local Site Environments in Mn: CdSe Quantum Dots

Author: Weiwei Zheng et al.

Publication: The Journal of Physical Chemistry C

Publisher: American Chemical Society

Date: Oct 1, 2011

Copyright © 2011, American Chemical Society

Logged in as:

Weiwei Zheng

Account #:

3000451324

[LOGOUT](#)

PERMISSION/LICENSE IS GRANTED FOR YOUR ORDER AT NO CHARGE

This type of permission/license, instead of the standard Terms & Conditions, is sent to you because no fee is being charged for your order. Please note the following:

- Permission is granted for your request in both print and electronic formats.
- If figures and/or tables were requested, they may be adapted or used in part.
- Please print this page for your records and send a copy of it to your publisher/graduate school.
- Appropriate credit for the requested material should be given as follows: "Reprinted (adapted) with permission from (COMPLETE REFERENCE CITATION). Copyright (YEAR) American Chemical Society." Insert appropriate information in place of the capitalized words.
- One-time permission is granted only for the use specified in your request. No additional uses are granted (such as derivative works or other editions). For any other uses, please submit a new request.

[BACK](#)

[CLOSE WINDOW](#)

Copyright © 2011 [Copyright Clearance Center, Inc.](#) All Rights Reserved. [Privacy statement](#). Comments? We would like to hear from you. E-mail us at customer@copyright.com

REFERENCES

- (1) Spaldin, N. A. *Magnetic materials: fundamentals and device applications*; Cambridge University Press: UK, 1969.
- (2) Kittel, C. *Introduction to Solid State Physics (8th ed.)* John Wiley & Sons. New York, 2005.
- (3) Sessoli, R.; Tsai, H. L.; Schake, A. R.; Wang, S.; Vincent, J. B.; Folting, K.; Gatteschi, D.; Christou, G.; Hendrickson, D. N. *J. Am. Chem. Soc.* **1993**, *115*, 1804-1816.
- (4) Stoner, E. C.; Wohlfarth, E. P. *IEEE Trans. Magn.* **1991**, *27*, 3475-3518.
- (5) Chikazumi, S.; Taketomi, S.; Ukita, M.; Mizukami, M.; Miyajima, H.; Setogawa, M.; Kurihara, Y. *J. Magn. Magn. Mater.* **1987**, *65*, 245-251.
- (6) Lu, A.-H.; Schmidt, W.; Matoussevitch, N.; Bönemann, H.; Spliethoff, B.; Tesche, B.; Bill, E.; Kiefer, W.; Schüth, F. *Angew. Chem. Int. Ed.* **2004**, *43*, 4303-4306.
- (7) Gupta, A. K.; Gupta, M. *Biomaterials* **2005**, *26*, 3995-4021.
- (8) Li, Z.; Wei, L.; Gao, M. Y.; Lei, H. *Adv. Mater.* **2005**, *17*, 1001-1005.
- (9) Hyeon, T. *Chem. Commun.* **2003**, 927-934.
- (10) Takafuji, M.; Ide, S.; Ihara, H.; Xu, Z. *Chem. Mater.* **2004**, *16*, 1977-1983.
- (11) Weller, D.; Moser, A.; Folks, L.; Best, M. E.; Wen, L.; Toney, M. F.; Schwickert, M.; Thiele, J. U.; Doerner, M. F. *IEEE Trans. Magn.* **2000**, *36*, 10-15.
- (12) Bean, C. P.; Livingston, J. D. *J. Appl. Phys.* **1959**, *30*, S120-S129.
- (13) Iwaki, T.; Kakihara, Y.; Toda, T.; Abdullah, M.; Okuyama, K. *J. Appl. Phys.* **2003**, *94*, 6807-6811.
- (14) Jeong, U.; Teng, X.; Wang, Y.; Yang, H.; Xia, Y. *Adv. Mater.* **2007**, *19*, 33-60.
- (15) Goya, G. F.; Berquo, T. S.; Fonseca, F. C.; Morales, M. P. *J. Appl. Phys.* **2003**, *94*, 3520-3528.
- (16) Dietl, T.; Ohno, H.; Matsukura, F. *Phys. Rev. B* **2001**, *63*, 195205.

- (17) Sachleben, J. R.; Wooten, E. W.; Emsley, L.; Pines, A.; Colvin, V. L.; Alivisatos, A. P. *Chem. Phys. Lett.* **1992**, *198*, 431-436.
- (18) Tomaselli, M.; Yarger, J. L.; Bruchez, M.; Havlin, R. H.; deGraw, D.; Pines, A.; Alivisatos, A. P. *J. Chem. Phys.* **1999**, *110*, 8861-8864.
- (19) Jasieniak, J.; Mulvaney, P. *J. Am. Chem. Soc.* **2007**, *129*, 2841-2848.
- (20) Lu, A.-H.; Salabas, E. L.; Schüth, F. *Angew. Chem. Int. Ed.* **2007**, *46*, 1222-1244.
- (21) Alivisatos, A. P. *Science* **1996**, *271*, 933-937.
- (22) Rosenthal, S. J.; McBride, J.; Pennycook, S. J.; Feldman, L. C. *Surf. Sci. Rep.* **2007**, *62*, 111-157.
- (23) Jaworski, C. M.; Yang, J.; Mack, S.; Awschalom, D. D.; Heremans, J. P.; Myers, R. C. *Nat Mater* **2010**, *9*, 898-903.
- (24) Furdyna, J. K. *J. Appl. Phys.* **1988**, *64*, R29-R64.
- (25) Dietl, T. *Nat Mater* **2010**, *9*, 965-974.
- (26) Haury, A.; Wasiela, A.; Arnoult, A.; Cibert, J.; Tatarenko, S.; Dietl, T.; d'Aubigne, Y. M. *Phys. Rev. Lett.* **1997**, *79*, 511-514.
- (27) Dietl, T.; Sawicki, M.; Van Khoi, L.; Jaroszyński, J.; Kossacki, P.; Cibert, J.; Ferrand, D.; Tatarenko, S.; Wasiela, A. *phys. status solidi B* **2002**, *229*, 665-672.
- (28) Junnarkar, M. R.; Alfano, R. R.; Furdyna, J. K. *IEEE J. Quantum Electron.* **1988**, *24*, 315-324.
- (29) Erwin, S. C.; Zu, L. J.; Haftel, M. I.; Efros, A. L.; Kennedy, T. A.; Norris, D. J. *Nature* **2005**, *436*, 91-94.
- (30) Hanif, K. M.; Meulenberg, R. W.; Strouse, G. F. *J. Am. Chem. Soc.* **2002**, *124*, 11495-11502.
- (31) Bryan, J. D.; Gamelin, D. R. In *Progress in Inorganic Chemistry*; Karlin, K. D., Ed. 2005; Vol. 54, p 47-126.

- (32) Meulenberg, R. W.; Lee, J. R. I.; McCall, S. K.; Hanif, K. M.; Haskel, D.; Lang, J. C.; Terminello, L. J.; van Buuren, T. *J. Am. Chem. Soc.* **2009**, *131*, 6888-6889.
- (33) Kittilstved, K. R.; Gamelin, D. R. *J. Am. Chem. Soc.* **2005**, *127*, 5292-5293.
- (34) Beaulac, R.; Archer, P. I.; Ochsenein, S. T.; Gamelin, D. R. *Adv. Funct. Mater.* **2008**, *18*, 3873-3891.
- (35) Norris, D. J.; Efros, A. L.; Erwin, S. C. *Science* **2008**, *319*, 1776-1779.
- (36) Mikulec, F. V.; Kuno, M.; Bennati, M.; Hall, D. A.; Griffin, R. G.; Bawendi, M. G. *J. Am. Chem. Soc.* **2000**, *122*, 2532-2540.
- (37) Magana, D.; Perera, S. C.; Harter, A. G.; Dalal, N. S.; Strouse, G. F. *J. Am. Chem. Soc.* **2006**, *128*, 2931-2939.
- (38) Beaulac, R.; Schneider, L.; Archer, P. I.; Bacher, G.; Gamelin, D. R. *Science* **2009**, *325*, 973-976.
- (39) Yu, J. H.; Liu, X.; Kweon, K. E.; Joo, J.; Park, J.; Ko, K.-T.; Lee, D. W.; Shen, S.; Tivakornsasithorn, K.; Son, J. S.; Park, J.-H.; Kim, Y.-W.; Hwang, G. S.; Dobrowolska, M.; Furdyna, J. K.; Hyeon, T. *Nat Mater* **2010**, *9*, 47-53.
- (40) Brus, L. E. *J. Chem. Phys.* **1984**, *80*, 4403-4409.
- (41) Neeleshwar, S.; Chen, C. L.; Tsai, C. B.; Chen, Y. Y.; Chen, C. C.; Shyu, S. G.; Seehra, M. *S. Phys. Rev. B* **2005**, *71*, 201307.
- (42) Hassan, A. K.; Pardi, L. A.; Krzystek, J.; Sienkiewicz, A.; Goy, P.; Rohrer, M.; Brunel, L. *C. J. Magn. Reson.* **2000**, *142*, 300-312.
- (43) Li, L. L.; Wu, S. Y.; Wang, X. F.; Xu, P. *Phys. Scr.* **2010**, *82*, 055701.
- (44) McGarvey, B. R. *J. Phys. Chem.* **1967**, *71*, 51-66.
- (45) Title, R. S. *Phys. Rev.* **1963**, *130*, 17-19.
- (46) Kennedy, T. A.; Glaser, E. R.; Klein, P. B.; Bhargava, R. N. *Phys. Rev. B* **1995**, *52*, R14356-R14359.
- (47) Norris, D. J.; Yao, N.; Charnock, F. T.; Kennedy, T. A. *Nano Lett.* **2001**, *1*, 3-7.

- (48) Misra, S. K.; Andronenko, S. I.; Earle, K. A.; Freed, J. H. *Appl. Magn. Reson.* **2001**, *21*, 549-561.
- (49) Ohno, H. *Science* **1998**, *281*, 951-956.
- (50) Ferrand, D.; Cibert, J.; Bourgognon, C.; Tatarenko, S.; Wasiela, A.; Fishman, G.; Bonanni, A.; Sitter, H.; Kolesnik, S.; Jaroszynski, J.; Barcz, A.; Dietl, T. *J. Cryst. Growth* **2000**, *214-215*, 387-390.
- (51) Lovingood, D. D.; Achey, R.; Paravastu, A. K.; Strouse, G. F. *J. Am. Chem. Soc.* **2010**, *132*, 3344-3354.
- (52) Meulenberg, R. W.; van Buuren, T.; Hanif, K. M.; Willey, T. M.; Strouse, G. F.; Terminello, L. J. *Nano Lett.* **2004**, *4*, 2277-2285.
- (53) Qu, L.; Peng, X. *J. Am. Chem. Soc.* **2002**, *124*, 2049-2055.
- (54) Bawendi, M. G.; Kortan, A. R.; Steigerwald, M. L.; Brus, L. E. *J. Chem. Phys.* **1989**, *91*, 7282-7290.
- (55) Murray, C. B.; Norris, D. J.; Bawendi, M. G. *J. Am. Chem. Soc.* **1993**, *115*, 8706-8715.
- (56) Kodama, R. H. *J. Magn. Magn. Mater.* **1999**, *200*, 359-372.
- (57) Culp, J. T.; Park, J.-H.; Meisel, M. W.; Talham, D. R. *Inorg. Chem.* **2003**, *42*, 2842-2848.
- (58) Goya, G. F.; Segredo, V. *Phys. Rev. B* **2001**, *64*, 235208.
- (59) Liu, C.; Zhang, Z. *J. Chem. Mater.* **2001**, *13*, 2092-2096.
- (60) Story, T.; Galazka, R. R.; Frankel, R. B.; Wolff, P. A. *Phys. Rev. Lett.* **1986**, *56*, 777-779.
- (61) Abolfath, M.; Jungwirth, T.; Brum, J.; MacDonald, A. H. *Phys. Rev. B* **2001**, *63*, 054418.
- (62) Gałazka, R. R. *phys. status solidi B* **2006**, *243*, 759-767.
- (63) Huxter, V. M.; Lee, A.; Lo, S. S.; Scholes, G. D. *Nano Lett.* **2009**, *9*, 405-409.
- (64) Sachleben, J. R.; Colvin, V.; Emsley, L.; Wooten, E. W.; Alivisatos, A. P. *J. Phys. Chem. B* **1998**, *102*, 10117-10128.

- (65) Puzder, A.; Williamson, A. J.; Gygi, F.; ccedil; ois; Galli, G. *Phys. Rev. Lett.* **2004**, *92*, 217401.
- (66) Gilbert, B.; Huang, F.; Zhang, H. Z.; Waychunas, G. A.; Banfield, J. F. *Science* **2004**, *305*, 651-654.
- (67) Ithurria, S.; Guyot-Sionnest, P.; Mahler, B.; Dubertret, B. *Phys. Rev. Lett.* **2007**, *99*, 265501.
- (68) Alivisatos, A. P. *Science* **1996**, *271*, 933-937.
- (69) Guyot-Sionnest, P. *Comp. Rend. Phys.* **2008**, *9*, 777-787.
- (70) Owen, J. S.; Park, J.; Trudeau, P.-E.; Alivisatos, A. P. *J. Am. Chem. Soc.* **2008**, *130*, 12279-12281.
- (71) Fuke, N.; Hoch, L. B.; Kuposov, A. Y.; Manner, V. W.; Werder, D. J.; Fukui, A.; Koide, N.; Katayama, H.; Sykora, M. *ACS Nano* **2010**, *4*, 6377-6386.
- (72) Guyot-Sionnest, P.; Wehrenberg, B.; Yu, D. *J. Chem. Phys.* **2005**, *123*.
- (73) Kalyuzhny, G.; Murray, R. W. *J. Phys. Chem. B* **2005**, *109*, 7012-7021.
- (74) Hohng, S.; Ha, T. *J. Am. Chem. Soc.* **2004**, *126*, 1324-1325.
- (75) Kippeny, T. C.; Bowers, M. J.; Dukes, A. D.; McBride, J. R.; Orndorff, R. L.; Garrett, M. D.; Rosenthal, S. J. *J. Chem. Phys.* **2008**, *128*.
- (76) Hwang, Y.-N.; Park, S.-H.; Kim, D. *Phys. Rev. B* **1999**, *59*, 7285-7288.
- (77) Zheng, W. W.; Strouse, G. F. *J. Am. Chem. Soc.* **2011**, *133*, 7482-7489.
- (78) Becerra, L. R.; Murray, C. B.; Griffin, R. G.; Bawendi, M. G. *J. Chem. Phys.* **1994**, *100*, 3297-3300.
- (79) Berrettini, M. G.; Braun, G.; Hu, J. G.; Strouse, G. F. *J. Am. Chem. Soc.* **2004**, *126*, 7063-7070.
- (80) Ratcliffe, C. I.; Yu, K.; Ripmeester, J. A.; Badruz Zaman, M.; Badarau, C.; Singh, S. *Phys. Chem. Chem. Phys.* **2006**, *8*, 3510-3519.
- (81) Washington, A. L.; Strouse, G. F. *J. Am. Chem. Soc.* **2008**, *130*, 8916-8922.

- (82) Kuno, M.; Lee, J. K.; Dabbousi, B. O.; Mikulec, F. V.; Bawendi, M. G. *J. Chem. Phys.* **1997**, *106*, 9869-9882.
- (83) Lovingood, D. D.; Oyler, R. E.; Strouse, G. F. *J. Am. Chem. Soc.* **2008**, *130*, 17004-17011.
- (84) Raola, O. E.; Strouse, G. F. *Nano Lett.* **2002**, *2*, 1443-1447.
- (85) Du, J.; Gao, Y. Q.; Chai, L. L.; Zou, G. F.; Li, Y.; Qian, Y. T. *Nanotechnology* **2006**, *17*, 4923-4928.
- (86) Wang, D.-S.; Xie, T.; Peng, Q.; Zhang, S.-Y.; Chen, J.; Li, Y.-D. *Chem. Eur. J.* **2008**, *14*, 2507-2513.
- (87) Cage, B.; Hassan, A. K.; Pardi, L.; Krzystek, J.; Brunel, L.-C.; Dalal, N. S. *J. Magn. Reson.* **1997**, *124*, 495-498.
- (88) Wood, R. M.; Stucker, D. M.; Jones, L. M.; Lynch, W. B.; Misra, S. K.; Freed, J. H. *Inorg. Chem.* **1999**, *38*, 5384-5388.
- (89) Archer, P. I.; Santangelo, S. A.; Gamelin, D. R. *Nano Lett.* **2007**, *7*, 1037-1043.
- (90) Jian, W. B.; Fang, J. Y.; Ji, T. H.; He, J. B. *Appl. Phys. Lett.* **2003**, *83*, 3377-3379.
- (91) Park, K.; Novotny, M. A.; Dalal, N. S.; Hill, S.; Rikvold, P. A. *Phys. Rev. B* **2001**, *65*, 014426.
- (92) Park, K.; Novotny, M. A.; Dalal, N. S.; Hill, S.; Rikvold, P. A. *Phys. Rev. B* **2002**, *66*, 144409.
- (93) Abragam, A.; Bleaney, B. *Electron paramagnetic resonance of transition ions*; Dover Publications: New York, 1986.
- (94) Griscom, D. L.; Griscom, R. E. *J. Chem. Phys.* **1967**, *47*, 2711-2722.
- (95) Bhattacharyya, S.; Zitoun, D.; Gedanken, A. *J. Phys. Chem. C* **2008**, *112*, 7624-7630.
- (96) Arom í G.; Telsler, J.; Ozarowski, A.; Brunel, L.-C.; Stoeckli-Evans, H.-M.; Krzystek, J. *Inorg. Chem.* **2004**, *44*, 187-196.
- (97) Lita, A.; Ma, X.; Meulenberg, R. W.; van Buuren, T.; Stiegman, A. E. *Inorg. Chem.* **2008**, *47*, 7302-7308.

- (98) Stavitski, E.; de Groot, F. M. F. *Micron* **2010**, *41*, 687-694.
- (99) Walsh, W. M. *Phys. Rev.* **1961**, *122*, 762-771.
- (100) Keller, S. P.; Gelles, I. L.; Smith, W. V. *Phys. Rev.* **1958**, *110*, 850-855.
- (101) Huheey, J. E.; Keiter, E. A. E.; Keiter, R. L. *Inorganic Chemistry: Principles of Structure and Reactivity*; 4th ed. Prentice-Hall: Upper Saddle River, NJ, 1997.
- (102) Nag, A.; Sapra, S.; Nagamani, C.; Sharma, A.; Pradhan, N.; Bhat, S. V.; Sarma, D. D. *Chem. Mater.* **2007**, *19*, 3252-3259.
- (103) Title, R. S. *Phys. Rev.* **1964**, *133*, A1613.
- (104) Estle, T. L.; Holton, W. C. *Phys. Rev.* **1966**, *150*, 159.
- (105) Boonman, M. E. J.; Mac, W.; Twardowski, A.; Wittlin, A.; van Bentum, P. J. M.; Maan, J. C.; Demianiuk, M. *Phys. Rev. B* **2000**, *61*, 5358.
- (106) Vallin, J. T.; Watkins, G. D. *Phys. Rev. B* **1974**, *9*, 2051.
- (107) Rai, R.; Savard, J. Y.; Tousignant, B. *Physics Letters A* **1967**, *25*, 443-444.
- (108) Stefaniuk, L.; Bester, M.; Virt, I. S.; Kuzma, M. *Acta Phys. Pol., A* **2005**, *108*, 413-418.
- (109) Mac, W.; Khoi, N. T.; Twardowski, A.; Gaj, J. A.; Demianiuk, M. *Phys. Rev. Lett.* **1993**, *71*, 2327-2330.
- (110) Mac, W.; Twardowski, A.; Eggenkamp, P. J. T.; Swagten, H. J. M.; Shapira, Y.; Demianiuk, M. *Phys. Rev. B* **1994**, *50*, 14144-14154.
- (111) Vallin, J. T.; Slack, G. A.; Roberts, S.; Hughes, A. E. *Phys. Rev. B* **1970**, *2*, 4313.
- (112) Ohgushi, K.; Okimoto, Y.; Ogasawara, T.; Miyasaka, S.; Tokura, Y. *J. Phys. Soc. Jpn.* **2008**, *77*, 034713.
- (113) Kalinnikov, V. T.; Aminov, T. G.; Novotortsev, V. M. *Inorg. Mater.* **2003**, *39*, 997-1012.
- (114) Baltzer, P. K.; Lehmann, H. W.; Robbins, M. *Phys. Rev. Lett.* **1965**, *15*, 493-495.
- (115) Menyuk, N.; Dwight, K.; Arnott, R. J.; Wold, A. *J. Appl. Phys.* **1966**, *37*, 1387-1388.

- (116) Siratori, K. *J. Phys. Soc. Jpn.* **1971**, *30*, 709-719.
- (117) Akimitsu, J.; Siratori, K.; Shirane, G.; Iizumi, M.; Watanabe, T. *J. Phys. Soc. Jpn.* **1978**, *44*, 172-180.
- (118) Yang, Y.; Chen, O.; Angerhofer, A.; Cao, Y. C. *J. Am. Chem. Soc.* **2008**, *130*, 15649-15661.
- (119) Buonsanti, R.; Llordes, A.; Aloni, S.; Helms, B. A.; Milliron, D. J. *Nano Lett.* **2011**, **Article ASAP**.
- (120) Quarez, E.; Hsu, K.-F.; Pcionek, R.; Frangis, N.; Polychroniadis, E. K.; Kanatzidis, M. G. *J. Am. Chem. Soc.* **2005**, *127*, 9177-9190.
- (121) Liu, H.; Owen, J. S.; Alivisatos, A. P. *J. Am. Chem. Soc.* **2006**, *129*, 305-312.
- (122) Zhang, X.; Sun, Z.; Yan, W.; Wei, F.; Wei, S. Q. *Mater. Chem. Phys.* **2008**, *111*, 513-516.
- (123) Rogach, A. L.; Kornowski, A.; Gao, M.; Eychmüller, A.; Weller, H. *J. Phys. Chem. B* **1999**, *103*, 3065-3069.
- (124) Huang, F.; Banfield, J. F. *J. Am. Chem. Soc.* **2005**, *127*, 4523-4529.
- (125) Yokaichiya, F.; Krimmel, A.; Tsurkan, V.; Margiolaki, I.; Thompson, P.; Bordallo, H. N.; Buchsteiner, A.; Stüßer, N.; Argryriou, D. N.; Loidl, A. *Phys. Rev. B* **2009**, *79*, 064423.
- (126) Baltzer, P. K.; Robbins, M.; Wojtowicz, P. *J. Appl. Phys.* **1967**, *38*, 953-954.
- (127) F.K., L. *Solid State Commun.* **1965**, *3*, 347-349.
- (128) Cumberland, S. L.; Hanif, K. M.; Javier, A.; Khitrov, G. A.; Strouse, G. F.; Woessner, S. M.; Yun, C. S. *Chem. Mater.* **2002**, *14*, 1576-1584.
- (129) Kimura, A.; Matsuno, J.; Okabayashi, J.; Fujimori, A.; Shishidou, T.; Kulatov, E.; Kanomata, T. *Phys. Rev. B* **2001**, *63*, 224420.
- (130) Farvid, S. S.; Ju, L.; Worden, M.; Radovanovic, P. V. *J. Phys. Chem. C* **2008**, *112*, 17755-17759.
- (131) Koshizuka, N.; Yokoyama, Y.; Okuda, T.; Tsushima, T. *J. Appl. Phys.* **1978**, *49*, 2183-2185.

- (132) Stręk, W.; Dereń, P.; Jezowska-Trzebiatowska, B. *J. Lumin.* **1988**, *40-41*, 421-422.
- (133) Krzystek, J.; Ozarowski, A.; Telsler, J. *Coord. Chem. Rev.* **2006**, *250*, 2308-2324.
- (134) Thorp, J. S.; Skinner, A. R.; Al-Hawery, A. S. *J. Magn. Magn. Mater.* **1989**, *81*, 47-55.
- (135) Carlin, R. L. *Magnetochemistry* Springer-Verlag: Berlin Heidelberg New York Tokyo, 1985.
- (136) Arrott, A. *Phys. Rev.* **1957**, *108*, 1394-1396.
- (137) Yeung, I.; Roshko, R. M.; Williams, G. *Phys. Rev. B* **1986**, *34*, 3456-3457.
- (138) Baltzer, P. K.; Wojtowicz, P. J.; Robbins, M.; Lopatin, E. *Phys. Rev.* **1966**, *151*, 367-377.

BIOGRAPHICAL SKETCH

Education

- Florida State University, Tallahassee, Florida, Ph.D in Inorganic Chemistry, October 2011. Thesis: The interplay of size- and site-dependence of magnetic properties of diluted magnetic semiconductor quantum dots
- University of Science & Technology of China, Hefei, China, M. S. in Inorganic Chemistry, August, 2005. Thesis: Hydrothermal growth and characterization of wide-band gap semiconductor crystal
- Anhui Normal University, Wuhu, China, B. S. in Chemistry in Applied Chemistry.

Working & Teaching Experience

- Graduate Teaching Assistant – Florida State University, 2005-2011
- Graduate Researcher – Florida State University, 2005-2011
- Assistant professor –Fuyang Normal Collegy, 1999-2002

Honors & Scholarship

- In 2008, nominee for the Outstanding Teaching Assistant Award by FSU
- In 2004, received Donggang Graduate Student Scholarship from University of Science and Technology of China
- In 2000, recognized as an Outstanding Instructor by Fuyang Normal College
- In 1999, recognized as an Outstanding Graduate Student of Anhui Province by the Educational Committee of Anhui Province, presented to the top 1% of students
- From 1996-1999, received Outstanding Student Scholarship & Outstanding Student Leader four times by Anhui Normal University, presented to the top 3% of students

Publications

1. **Zheng, Weiwei**; Strouse, G. F.; Involvement of Carriers in the Size-dependent Magnetic Exchange for Mn:CdSe Quantum Dots. *J. Am. Chem. Soc.* **2011**, *133*, 7482–7489.
2. **Zheng, Weiwei**; Wang, Z.; Wright, J.; Dalal, N. S.; Meulenberg, R. W.; Strouse, G. F. Probing the Local Site Environments of Mn(II) in Mn:CdSe Quantum Dots. *J. Phys. Chem. C* **2011**, Accepted.
3. **Zheng, Weiwei**; Singh, K.; Wang, Z.; Wright, J.; van Tol, J.; Dalal, N. S.; Meulenberg, R. W.; Strouse, G. F. Evidence of Spinel Phase in Cr Doped ZnSe Quantum Dots. (Submitted to *J. Am. Chem. Soc.*)
4. Zhenxing Wang, **Weiwei Zheng**, Johan van Tol, Naresh S. Dalal, Geoffrey F. Strouse. High-Field Electron Paramagnetic Resonance as a Microscopic Probe of Lattice Strain in CdSe:Mn²⁺ Nanoparticles. (Submitted to *Chem. Phys. Lett.*)
5. **Zheng, Weiwei**; Guo, F.; Qian, Y. The Growth of Bulk ZnO Single Crystals via a Novel Hydrothermal Oxidative Pressure-relief Route. *Adv. Funct. Mater.* **2005**, *2*, 331–335.
6. **Zheng, Weiwei**; Guo, F.; Wan, S.; Liu, X.; Yin, Y. Synthesis and Characterization of GaN Nanocrystal. *Journal of Synthetic Crystals.* **2003**, *32*, 210–213.
7. Fan, H.; Wang, Z.; Liu, X.; **Zheng, Weiwei**; Guo, F.; Qian, Y. Controlled synthesis of trigonal selenium crystals with different morphologies. *Solid State Commun.* **2005**, *135*, 319–322.
8. Zhang, Y.; Guo, F.; Wan, S.; **Zheng, Weiwei**; Peng, Y.; In situ deposition of Co₉S₈ nanocrystallite on its single-crystal flakes at low temperature. *Bull. Chem. Soc. Jpn.* **2005**, *78*, 277–280.

9. Wan, S.; Guo, F.; Zhang, Y.; **Zheng, Weiwei**; Zhang, Y.; Qian, Y. CuBr Crystal Growth in Ethylene Glycol Solvent by the Temperature-Difference Method. *Cryst. Growth Des.* **2004**, *4*, 413–414.

Presentations

Definitive Spectroscopic Characterization of Doping Sites in Mn:CdSe Quantum Dots, 239th ACS National Meeting, San Francisco, CA. March 2010

Synthesis and Characterization of Mn doped CdSe Quantum Dots, Poster Presentation 4th Annual Florida Inorganic Mini-Symposium, Gainesville, FL. Oct. 2006